Characterization and Size Optimization of Additively Manufactured Flexible Piezoresistive Sensors for Vibration Strain Sensing

by

Jeffrey Andrew Sixt

A thesis

presented to the University of Waterloo

in fulfillment of the

thesis requirement for the degree of

Master of Applied Science

in

Mechanical and Mechatronics Engineering

Waterloo, Ontario, Canada, 2021

Author's Declaration

This thesis consists of material all of which I authored or co-authored; see Statement of Contributions included in the thesis. This is a true copy of my thesis, including any required final revisions, as accepted by my examiners.

I understand that my thesis may be made electronically available to the public.

Statement of Contributions

This research was completed at the University of Waterloo by Jeffrey Sixt under the joint supervision of Dr. Armaghan Salehian and Dr. Ehsan Toyserkani. Jeffrey Sixt was the sole author for Chapter 1, Chapter 2, and Chapter 5, which were written under the supervision of Dr. Armaghan Salehian and Dr. Ehsan Toyserkani.

Exceptions to sole authorship of material are as follows:

- Dr. Elham Davoodi: Developed the general fabrication process used, suggested the initial/benchmark sensor design to use in Section 3.1, provided scanning electron microscopy images Figure 3.2c and d and Appendix Figure A-1c, and provided general feedback on the presentation of results in Sections 3.1, 3.2.1, and 4.1.

Abstract

Flexible piezoresistive strain sensors have promising applications in areas such as wearables and soft robotics. For sensing dynamic strains, such as a runner's gait or a slipping object held by a robotic gripper, these sensors must capably measure strain over a range of amplitudes and frequencies. This thesis presents the characterization and optimization of a flexible piezoresistive sensor with triply periodic minimal surface (TPMS) structures for vibration strain sensing. Sensors are fabricated using an additive manufacturing (AM) process to subsurface coat a silicone rubber (SR) matrix with graphene nanoplatelets (GNP). These sensors are then characterized under uniaxial compressive strain amplitudes from 0-10% and frequencies of 10-110 Hz. Frequency and time domain analyses are used to demonstrate sensor performance and explain unique deformation mechanisms of the TPMS structure. Low sensor delays of less than 6.3 ms, and 0.420 ms on average, demonstrate its capability for high-frequency sensing. Frequency independence of the sensor is also demonstrated, as the mean error due to its sensitivity changing with frequency is only $\pm$3.89%. A second-degree polynomial calibration of the sensor is shown to predict the relationship between strain amplitude and sensor resistance change well, with a mean error of 3.56% for 2-10% strain amplitudes. Sensor durability is proven by testing ten sensors over 15×10^6 cycles and 80 hours without breaking. In addition, a multi-objective size optimization is performed for the TPMS sensor design, with the goal of improving its frequency independence and strain sensitivity. The optimization is solved using a multi-objective firefly algorithm (FA) and accounts for several fabrication constraints when finding a feasible sensor design. The first objective is to maximize the sensor's first natural frequency, which results in a reduced mean frequency dependence error of $\pm$2.18% during testing. To also attempt improving the sensor's strain sensitivity, given a negative (compressive) applied strain, the average principal strain at the sensor surface (where the GNP coating is located) is minimized. The implemented algorithm converged within 1618 unique function evaluations, a reduction of 85.5% compared to the entire set of feasible solutions. This design optimization is the first for a flexible piezoresistive sensor in literature.

Acknowledgements

The completion of my thesis would not be possible without the constant support, encouragement, and advice of many people. I would like to thank both my supervisors for maintaining a strong working relationship during my degree. Dr. Toyserkani gave great direction for my research thesis and focus, redirecting my attention on important details and giving constructive feedback on my progress. Dr. Salehian also played a key role in both my research and professional development. Her detailed insights and creative thinking helped guide my focus, and often improved the quality and value of results. Both supervisors were also very gracious in supporting many opportunities to explore different avenues of my research.

I would also like to thank Pranav Agrawal for helping me get settled quickly in our labs, helping troubleshoot problems, and offering his insights to support my academic development. Elham Davoodi also played a similar role in helping me get started working quickly in the lab. She was very generous with her time and gave me a great foundation of knowledge to start my research. I would also like to acknowledge Jerry Ratthapakdee, Grace Kurosad, Henry Ma, and Mark and Neil Griffett for their assistance in enabling my research. Last, I would like to thank my friends and family for their unconditional support and encouragement during my degree.

This research was made possible with funding from the Natural Sciences and Engineering Research Council of Canada (NSERC).

Table of Contents

List of Figures

List of Tables

List of Abbreviations

TPMS	Triply periodic minimal surfaces
AM	Additive manufacturing
SR	Silicone rubber
GNP	Graphene nanoplatelets
GF	Gauge factor
CAD	Computer-aided design
FDM	Fused deposition modelling
ABS	Acryl butadiene styrene
HMI	Human-machine interface
CPC	Conductive polymer composite
CNT	Carbon nanotubes
PDMS	Polydimethylsiloxane
DIW	Direct ink writing
SLS	Selective laser sintering
TPU	Thermoplastic polyurethane
MWCNT	Multi-walled carbon nanotubes
LPBF	Laser powder bed fusion
G-type	Gyroid type
D-type	Diamond type
P-type	Primitive type
FEA	Finite element analysis
FA	Firefly algorithm
PSO	Particle swarm optimization
GA	Genetic algorithm
NFE	Number of function evaluations
MOFA	Multi-objective firefly algorithm
IPA	Isopropanol alcohol
SEG	Surface-embedded graphene
SEM	Scanning electron microscopy
ML-G	Multi-layer graphene
PCB	Printed circuit board
DAS	Data acquisition system
FRF	Frequency response function
BC	Boundary condition
FE	Finite element

AC	Alternating current
FFT	Fast Fourier transform
CT	Computed tomography

Chapter 1
Introduction

1.1 Piezoresistive Sensors

For the measurement of mechanical strain in a range of engineering applications, piezoresistive strain sensors serve an important purpose. Piezoresistive behaviour is described by a material's changing electrical resistance while being strained, due to changes in the material resistivity and dimensions [1]. For piezoresistive sensors, this effect can be modeled and/or experimentally determined to correlate a change in sensor resistance to a mechanical strain, thus providing a reliable way to measure strain. A large strain sensitivity, commonly referred to as gauge factor (GF), is preferred, as this amplifies the sensor signal. Traditionally, piezoresistive strain sensing has been accomplished using metal alloys to monitor strains in stiff structural members [1]. However, these materials are limited to applications with small strains due to their high elastic moduli and low yield strains. For example, metallic high-performance strain gauges have operating strain limits of 1-2% [1].

With the recent interest in wearable technologies, biomedical research, and soft robotics, it has become increasingly important to develop flexible piezoresistive sensors. Compared to other strain sensors, the current literature lists advantages of flexible piezoresistive sensors to include simple electronic read-out, easy fabrication, and wide strain detection ranges [2], [3]. The performance of these sensors depends in general on their fabrication processes and design.

1.2 Additive Manufacturing and Design Optimization

Additive manufacturing (AM), also referred to as three-dimensional (3D) printing, is a fabrication process defined by the depositing/joining material in sequential layers to progressively build a 3D object. AM processes are flexible and can fabricate parts for many different applications, including flexible piezoresistive sensors. AM processes offer advantages including reduced fabrication lead times [4], enhanced design freedom at reduced resource costs [5], and personalization for users and use-cases [6]. Many geometries that could not be fabricated using traditional subtractive manufacturing methods can be easily created with AM. This freedom also allows fast, easy customization of objects for different users and applications, as custom tooling is not required for AM. This greatly reduces lead times between the computer-aided design (CAD) process and manufacturing. Another advantage of some AM processes is increased accessibility. For less

expensive AM processes, including those which use polymer materials, 3D printers are easily available to small businesses and consumers. Fused deposition modelling (FDM), a class of material extrusion AM, is an inexpensive process that deposits polymer filament through a heated extruder nozzle (see Figure 1.1). Common print materials for FDM include acryl butadiene styrene (ABS), nylon, polycarbonate, and polylactic acid. While FDM has limitations, such as requiring support material for shallow overhangs, it overall enables enhanced freedom in the engineering design process. This freedom also translates to improved design optimization by reducing fabrication constraints on design possibilities.

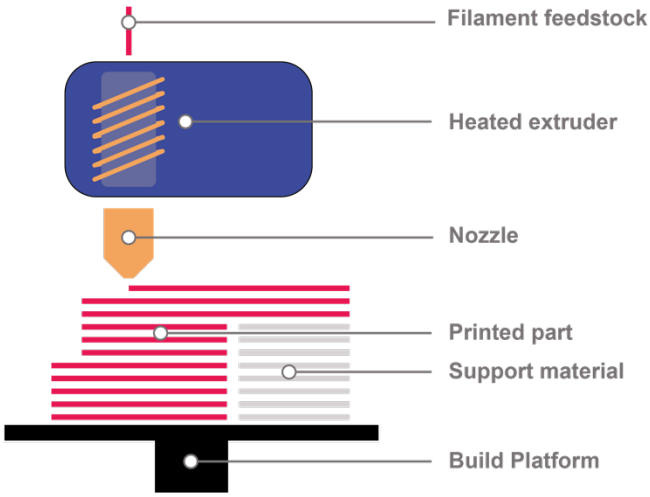

Figure 1.1. FDM printing process diagram.

Optimization is a necessary step in the design process for improving product performance. Design optimization with AM can be split into three main categories: shape, topology, and size optimization. Shape optimizations create an optimal design by moving the surface nodes of an initial geometry, while topology optimizations work to define optimal material placement and connectivity. In contrast, size optimizations modify design parameters such as object dimensions to find their optimal values. Many tunable geometries are well-suited for size optimization, including strut- and sheet-based lattice structures. When optimizing a design, the manufacturing process limitations must also be accounted for either during the optimization definition or as a post-processing step.

1.3 Motivation

Recent research on flexible piezoresistive strain sensors has focused on developing novel fabrication processes, geometries, and materials to improve performance. In addition, while characterization under quasistatic loading of these sensors is common, vibration strain sensing is often not characterized. Flexible vibration strain sensors can be used in a variety of applications such as wearables and soft robotics. For example, flexible wearable sensors that measure strain vibration can be required in space suits to help prevent bone mass density loss. During prolonged astronaut missions, reductions in bone mass density may occur due to the lower gravity in outer space. To combat this, studies have shown that bone mass density loss can be prevented by exposing the body to extended periods of vibration (20-90 Hz at 0.5-4.0 mm [7], [8]). As a result, space suits have been suggested to be equipped with sensors and actuators to monitor and subject the wearer to sufficient vibration [9]. Flexible wearable sensors capable of tracking daily exposure to a range of vibration frequencies and amplitudes are thus required for this application. Also, robots being used in human-machine interfaces (HMI) can require tactile sensing. Some HMIs involve a robot being operated remotely by a human, often in cases where the robot provides some additional capability or the location is too inconvenient or dangerous to be visited. Since the human operator is not directly in the robot's environment sensory feedback including tactile feedback is lost.

For this reason, robotic grippers require tactile sensing capabilities to provide vibration stimulation as feedback to the machine operator. The design of these robot grippers must be flexible enough to interact gently with the environment and deform to grab non-uniform surfaces. To meet these criteria while providing information for tactile feedback to the operator, robotic grippers should be equipped with flexible sensors capable of vibration strain sensing over a range of strains [10]. For example, Meissner corpuscle mechanoreceptors in human hands detect strain vibrations up to 20-50 Hz at thresholds of ~100 μm for contact and slip detection [11], [12], so a tactile sensor may require similar detection ranges. In addition, cutaneous nerves in human hands can convey tactile information in times of less than 12 ms [11]. Thus, flexible piezoresistive strain sensors should have similar fast response times. Flexible actuators have been developed for operating over a range of frequencies, such as 0-100 Hz for ionic polymer metal composites and bucky gel actuators [13]. However, flexible sensors for HMI still require further development for good sensing characterization over a range of strain amplitudes and frequencies [14].

To maintain a consistent relationship between strain and resistance change, a flexible vibration strain sensor should be frequency independent within a generally wide frequency range. As well, the sensor should have small signal delay between the input strain and output signal, good strain sensitivity, and should be calibratable. To validate a flexible vibration strain sensor design, these performance parameters should be characterized over a range of frequencies and strains. Beyond this, flexible piezoresistive sensor designs can also be optimized for applications in vibration strain sensing. Thus, design optimization strategies can be employed to further improve performance, and optimal designs can be experimentally validated. AM-based processes can enable fast, flexible fabrication of different optimized sensor designs.

1.4 Objectives

This work focuses on characterizing a flexible piezoresistive vibration strain sensor's performance for factors including frequency independence, signal delays, good strain sensitivity, and the potential to be calibrated for compressive vibration strain measurements. In addition, the sensor design should be further improved by optimizing its performance for vibration strain sensing. This can be done by pairing the AM sensor fabrication with a suitable optimization strategy. The thesis scope of work is outlined through the following objectives:

1) Characterize a flexible piezoresistive sensor, fabricated using AM, for vibration strain sensing.
2) Perform a size optimization of a flexible piezoresistive sensor for vibration strain sensing.
    a) Fabricate and experimentally validate the optimized sensor design.

To focus within this scope of work, a sensor fabrication process using tunable geometries is adopted from Davoodi et al. [15] to use as a foundation. This process utilizes the advantage of AM with a tunable geometry, making design optimization much more feasible, and is further discussed in Chapter 2.

1.5 Thesis Outline

Here a brief overview of the manuscript contents is for each of the 5 main chapters. The contents of each chapter are organized according to the two main objectives outlined. As such, each chapter begins by addressing characterization of flexible piezoresistive sensors, followed by any contents regarding size optimization of these sensors.

Chapter 1 and Chapter 2 cover the background information, motivations, literature review, and contributions in this work. As outlined, Chapter 1 gives a more brief, general overview of flexible piezoresistive strain sensors and their characterization and optimization. This allows objectives for this thesis to be established before elaborating with a more thorough literature review. Chapter 2 completes this review, discussing relevant literature. First, several flexible sensing technologies including piezoresistivity are discussed and compared. The resistance change mechanisms of popular flexible piezoresistive sensors are then introduced, followed by their AM fabrication methods. Flexible piezoresistive sensor geometries are discussed, particularly for tunable cellular structures. For vibration strain sensing, characterizations of flexible piezoresistive sensors are introduced and their results and methods are discussed. An overview of the sensor adopted in this work is given, and then design optimization strategies and relevant algorithms are introduced.

Chapter 3 continues by presenting the materials and methods used in this work. It begins with an overview of the manufacturing processes adopted from [15], and an initial characterization of the sensor materials used. Experimental methods are then discussed for any modelling and vibration testing. The optimization strategy is then discussed, including details of the optimization definition, the algorithm definition, and process flow. Manufacturing limitations are also accounted for in the optimization process.

Results are then presented in Chapter 4 for the vibration strain sensing characterization and subsequent optimization. Vibration strain sensing characterization results examine trends across a sample of 10 sensors, discussing strain sensitivity, signal delays, frequency independence, and sensor linearity and calibration. Then, the optimization results of the algorithm are presented, and an optimal design is fabricated. Testing is then repeated for this design to validate its performance and compare it to the previous sensor geometry used.

Last, Chapter 5 summarizes the results and insights from previous sections. Potential future work on these subjects is also discussed, as there are many interesting avenues for further sensor development.

Chapter 2
Literature Review and Contributions

Flexible strain sensors can vary widely in literature, according to their materials, shape, and fabrication processes. Despite their differences, these sensors can be grouped according to three main sensing mechanisms: capacitive, piezoelectric, and piezoresistive sensing. Each technology offers different advantages and disadvantages, which are discussed here. When making comparisons, sensor properties such as high flexibility (a wide operating strain range), low hysteresis, fast response times, and durability during cyclic loading are desirable [16]. Flexible capacitive strain sensors are comprised of a dielectric layer sandwiched between two electrodes. When compressed or stretched, the sensor will change in capacitance due to factors such as the distance between electrodes, which can be correlated to the applied strain. Dielectric and electrode layers are often flexible polymers such as polydimethylsiloxane (PDMS), where the electrode layers are filled with electrically conductive nanofillers such as carbon nanotubes (CNTs) [17]. Flexible capacitive sensors offer good sensitivities, fast response times, and simple structures [18]-[20]. Microstructures are also commonly applied to the dielectric layer to improve sensor performance. For example, micropores can be used to create high-capacitance voids in the sensor, such that voids closing during sensor compression create an amplified signal, thus improving sensitivity [21]. The sensor porosity also enables reversible, elastic deformation of the dielectric layer when strained, reducing sensor hysteresis and lowering stiffness [22]-[24]. Another alternative flexible sensing mechanism is piezoelectricity, where an electric charge is produced in the sensor material when subjected to mechanical strain. Piezoelectric behaviour is unique to certain materials, such that there is a limited range of materials capable of piezoelectric flexible strain sensing, including polyvinylidene fluoride and poly(vinylidenefluoride-co-trifluoroethylene) [25], [26]. While these materials are inexpensive and easy to prepare, they compromise between flexibility and high piezoelectric constants, delivering poorer strain sensing ranges and sensitivities than many capacitive and piezoresistive alternatives [22], [23]. Last, flexible piezoresistive sensors work by changing their electrical resistance when strained, such that changes in electrical resistance can be correlated to an applied strain. These are popular in literature for their wide strain detection ranges, low working voltages, and simple fabrication and signal measurement [18], [19], [22], [27]. Their construction normally consists of a flexible polymer material matrix combined with a conductive nanomaterial filler. This creates a flexible structure, while a sufficient

fraction of nanomaterial will form long-range connectivity pathways such that the sensor conducts electricity. This fraction is referred to as the percolation threshold. While the polymer matrix provides sensor flexibility, a disadvantage is that the internal friction in polymer chains can cause mechanical hysteresis, leading to longer sensor response and recovery times [22]. Piezoresistive sensor resistance change is described by $\Delta R/R_o$, where R_o is the nominal sensor resistance, and ΔR is the magnitude of its resistance change for a given strain. It is desirable for these sensors to have a large strain sensitivity, or GF, as defined by Equation (2.1).

$$GF = \frac{(\Delta R/R_o)}{\varepsilon} \tag{2.1}$$

where strain applied to the sensor is described by $\varepsilon = \Delta l/l_o$, with Δl as the change in sensor length and l_o as its original length. Compared to traditional metallic strain sensors, flexible piezoresistive sensors can have much higher GFs, which range widely from 4.7 - 10,000 depending on the sensor and strain applied [28]-[31]. While capacitive sensors are often very flat with high aspect ratios, piezoresistive flexible strain sensor geometries are more widely varied in literature. This makes them more advantageous as multifunctional materials, since 3D sensors can offer structure and sensing capability within one device. Flexible piezoresistive sensors have also been shown to maintain durability beyond tens of thousands of cycles [16], [32], [33]. Overall, flexible piezoresistive sensors are very advantageous for strain sensing, having been applied to HMIs, soft robotics, and wearable technologies/e-skin [23], [34]-[37].

2.1 Flexible Piezoresistive Strain Sensors

As discussed, flexible piezoresistive strain sensors combine flexible matrix materials and nanomaterials, which are often referred to as conductive polymer composites (CPCs). Carbon-based CPCs have been studied widely for flexible strain sensing [38], [39], and are fabricated through a range of methods combining a flexible matrix with nanomaterial carbon allotropes. Common sensor matrix materials include SR [40], [41], thermoplastic polyurethane (TPU) [35], PDMS [33], [42], [43], and polyimide [44], [45]. Matrix materials with high flexibility and failure strain are chosen to enhance the sensor's operating strain range [46], and also provide the compliance required for their application. For example, a sensor designed to be implanted in the sole of the shoe should have a similar compliance to the sole. Examples of carbon allotropes used for CPCs in literature include

graphene [33], [47], [48], graphene oxide [48], reduced graphene oxide [44], [45], and CNTs [36], [40], [42], [49], [50]. These carbon nanomaterials are popular for flexible piezoresistive strain sensors due to their high electrical conductivity [51], [52], adaptability to different sensor geometries [53], and their ability to form macroscopic conductive nanoparticle networks [38]. Nanoparticles are used as a filler in the matrix material [54], or as a surface coating [31], [47], [55], [56], to form a conductive nanoparticle network such that the sensor has a measurable electrical resistance.

2.1.1 Piezoresistive Mechanisms of Conductive Nanoparticle Networks

Here the piezoresistive mechanisms of conductive nanoparticle networks are discussed, specifically for carbon allotropes. Figure 2.1 depicts the main potential mechanisms by which flexible piezoresistive sensors with a conductive nanoparticle network can change their resistance when strained. These mechanisms are: nanoparticle strain, contact/overlap, and/or electron tunneling [38].

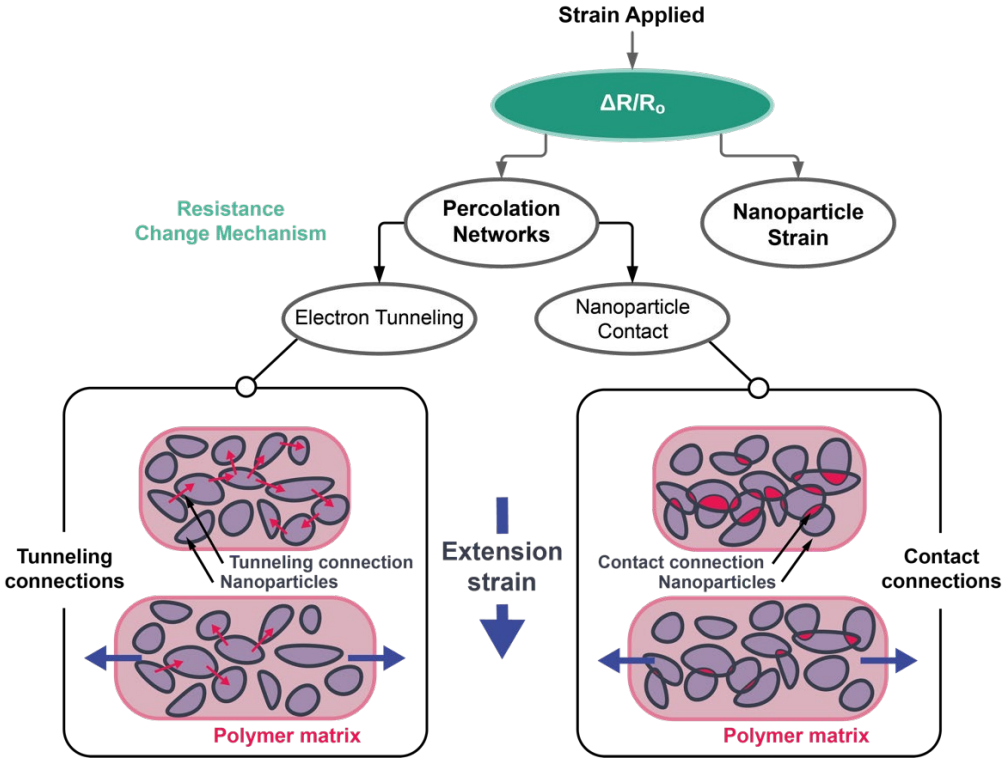

Figure 2.1. Mechanisms for resistance change in graphene-based conductive particle networks. Illustrations of percolation networks and their changing interparticle connections with strain are shown.

First, resistance changes due to nanoparticle strain are considered. This can occur due to strain transfer from the matrix material to individual nanoparticles, causing the nanoparticles to change resistance. However, this effect is typically ignored when modelling resistance changes of carbon conductive nanoparticle networks [57], [58]. This is due to the high conductivity of carbon nanomaterials, which makes their resistance change negligible in comparison to other mechanisms.

Second, nanoparticles can rearrange themselves relative to each other in an overlapping/contacting percolation network [38]. Thus, resistance changes are due to nanoparticles forming, altering, or breaking conductive pathways where they overlap and touch. For example, Hempel et al. [53] studied the spray-coating of graphene flakes on a flat polymer substrate to form a percolation network. They observed that weak out-of-plane bonding for graphene flakes permitted relative sliding between layered sheets, allowing contact areas to change more freely with strain [53]. Factors such as nanoparticle aspect ratios [59] and the nanoparticle type [60] influence the percolation threshold. As well, Mei et al. [61] created a composite sensor with a graphene 3D percolation network in TPU. During testing they observed that some conductive network connections are permanently broken, requiring the sensor to go through a conditioning period before performance stabilizes [61]. Similar observations have been made within other publications on conductive nanoparticle networks in polymer matrices [62], [63]. Models of CPC's resistance changes when strained have also been developed in the literature. For example, Yang et al. [63] developed a model for graphene filler in SR by dividing resistance changes during cyclic strain into stages of loading, unloading, and bending caused by residual deformation. The authors used the Kraus model and Smoluchowski equation to derive Equation (2.2), which describes resistance change due to rearranging of the nanoparticle network and formation/destruction of conductive paths during loading [63].

$$\frac{\Delta R}{R_o} = (\varepsilon + 1)^2 \left[\left(1 + \left(\frac{\varepsilon}{\varepsilon_c} \right)^{2m} \right)^{-1} \right]^{-n_\varepsilon} - 1 \tag{2.2}$$

where ε_c is the yield strain of the composite material, m is a constant related to the conductive network structure, and n_ε is a scaling constant. While strain terms here are raised to exponents, their contribution to exponential resistance change does not become significant until larger strains are applied. Overall, the dominant resistance change is described by the material yield strain, strain rate, and strain applied. Their model matched well with some experimental measurements of resistance

change for a simple rectangular CPC. The authors in [63] also hypothesize that residual deformation in the CPC can cause secondary bending effects during unloading, which cause competing resistance changing opposing the dominant resistance change. While this behaviour has been observed across different CPCs, its main cause is still not fully agreed upon in literature.

Last, non-contacting, neighbouring nanoparticles in CPCs can conduct electricity by forming an electron tunneling percolation network. Thus, relative motion between these particles will change the tunneling resistances. In many models the stiff nanoparticles are assumed not to touch if they're dispersed within a soft polymer matrix, which is referred to as the "hard core soft shell" assumption [58]. However, if nanoparticles are very close (within approximately < 2.0 nm for electron tunneling between graphene sheets [58]), electron tunneling connections will be present. These connections can be broken or formed, or their conductivity strength may also change depending on the tunneling distance. This is described well by the Simmons tunneling resistance model (see Equation (2.3)) for two neighbouring nanoparticles [64], [65].

$$R_{tunnel} = \frac{h^2 d}{Ae^2\sqrt{2m\lambda}} exp\left(\frac{4\pi d}{h}\sqrt{2m\lambda}\right) \tag{2.3}$$

where h is Plank's constant, d is the distance between nanoparticles, A is the tunneling connection cross-sectional area, m is the mass of an electron, e is the charge of an electron, and λ is the barrier height. Since d is part of the exponential term in Equation (2.3), R_{tunnel} describes a non-linear relationship between strain and tunneling resistance [66]. Other factors affecting tunneling can include nanoparticle size, aspect ratio/shape, and polymer properties [67] . Wang and Ye [57] also investigated the modelling of CNT resistances in CPCs, in addition to the tunneling junction resistances, and showed that CNT resistances can be ignored in the model.

Overall, accurately modelling nanoparticle networks in CPCs requires precise control of manufacturing processes and good assumptions to produce repeatable results. In addition, modelling detailed nanoparticle interactions (such as the orientation of CNTs) at the nanoscale can be computationally expensive and challenging. Whether the resistance change mechanism is dominated by overlapping nanoparticle networks or tunneling connections, strain experienced by the conductive network is always positively correlated with resistance change. Thus, the average strain experienced by the nanoparticle network determines the CPC's electrical resistance [68].

Regardless of the dominant piezoresistive mechanism for a flexible strain sensor, they often exhibit a non-linear relationship between resistance change and applied strain [56], [69]. This is particularly observed at higher strains. As discussed above, the percolation networks can exhibit a non-linear relationship with strain for both tunneling and contacting nanoparticle connections. Also, it is noted that any piezoresistive sensor will have a maximum limit for how much their resistance can change. When the sensor structure is in tension, its resistance will increase with applied strain until it reaches an upper limit (its percolation threshold). Conversely, the sensor resistance will decrease when under compressive strain until it reaches a lower limit (approaching zero ohms). In either case, the sensor resistance change will taper off in magnitude as it approaches its limit, which causes a non-linear relationship to the applied strain near the limit. While a higher GF is desirable, this will cause the sensor to approach its maximum/minimum resistance faster. This reduces the strain operating range of the sensor and can increase its region of non-linear behaviour. As a result, combining wide strain operating ranges and high GFs is a significant challenge in literature [63], [69].

2.1.2 AM Sensor Fabrication

To fabricate flexible piezoresistive sensors, AM is often used in literature to create carbon-based CPCs. Several methods of AM have been used for this purpose, including direct ink writing (DIW), FDM, and laser powder bed fusion (LPBF) which are presented and compared here.

DIW is often used for the fabrication of CPCs by depositing inks onto a substrate through a nozzle/syringe printer head. This is practical as it allows custom inks to be created by combining fillers and polymers before printing [70], [71]. For example, Huang et al. [6] developed a graphene-based flexible strain sensor that was 3D printed using DIW technology. Under quasi-static loading, the sensor displayed durability, high sensitivity at 30% mechanical strain, and had tunable properties due to the manufacturing method [6]. Wei et al. [29] created a TPU and carbon black CPC foam using DIW for sensing compressive strains. The sensor displayed good resistance recovery and a wide strain range up to 80% tested, with a GF up to 4.7. Nesaei et al. [72] studied the effects of DIW process parameters on the resistivity of CPCs, showing a positive correlation between resistivity and printing speed for multiple conductive inks. In addition, DIW fabricated parts can be susceptible to poor mechanical properties due to poor interlayer adhesion and material voids [73]. Zhang et al. [74] also stated that significant signal delays in CPCs made with DIW can exist due to poor strain transfer between the substrate and sensor.

FDM printing is also adapted to make many different CPC geometries using different materials in literature. For example, Christ et al. [75] fabricated uniaxial and biaxial flexible piezoresistive sensors using dual extrusion of TPU and multi-walled carbon nanotube (MWCNT)/TPU materials. They were able to cyclically test samples up to 50% strain and detect finger motions by incorporating the sensors in a wearable glove. FDM also allows creation of custom material filaments for printing. For example, Chen et al. [28] combined MWCNT, graphene nanoplatelet (GNP), and TPU in a screw extruder to create a filament for making CPCs. The structures printed exhibited high strain ranges up to 300% strain with a GF >10000, and good linearity up to 50% strain. Georgopoulou et al. [76] tested different conductive filaments, containing carbon black combined with either TPU or a styrenic block copolymer for FDM, measuring their mechanical properties and GF. They concluded that smaller diameter filaments produced better sensitivity, and GF increased for higher strain rates. A multi-material FDM approach was used by Hohimer et al. [77] to create soft pneumatic actuators out of TPU and TPU/MWCNTs. They found that process parameters such as layer height and print orientation influenced sensor performance. Conductivity generally increased with layer height for the same geometry due to the reduced number of layers, and thus interlayer seams. These seams can be prone to poor interlayer adhesion and voids, which decrease electrical conductivity. Similarly for print orientation, they show that conductivity is lower between toolpaths, compared to measuring conductivity along a toolpath, due to print voids. For printing of graphite-filled ethylene vinyl acetate CPCs, Kumar et al. [78] developed their own FDM printer to fabricate parts. They found a relatively high graphite content of 50 wt.% was required to produce good percolation, with conductivity of 2.3×10^{-4} S/cm.

Overall, FDM is preferred for CPCs due to its economic viability, low maintenance, flexibility for many applications, and low energy consumption [78]-[81]. Due to the simplicity of many FDM printers the process is very reliable, resulting in low material waste and more affordable printers [79]. As addressed earlier, FDM also provides great flexibility for creating different geometries, enabling mass customization and product personalization [80]. However, overhangs shallower than ~45 degrees typically require support structures [80]. Its other limitations include low resolution, higher surface roughness, slow print speeds [79], [82], and material anisotropy due to the print orientation and toolpath directions [82].

Another use of AM fabrication for CPCs involves printing of moulds. In addition to the AM methods mentioned, Kamat et al. [83] used LPBF of stainless steel to create a sacrificial mould. After

casting PDMS in the mould, it is dissolved using an etchant to leave behind the cured PDMS geometry. This technique was used to create microchannels infused with a GNP dispersion within a PDMS structure, such that it could be used as a force sensor. Here LPBF of stainless steel is desired to create strong moulds at good resolutions (near 140 microns wall thicknesses used) [83]. Some LPBF disadvantages include low print speeds and large power consumption [84]. Conversely, FDM has been used successfully for CPC mould printing in literature. For example, Nag et al. [85] made a reusable ABS mould for creating graphite and PDMS flexible capacitive strain sensors. The sensor developed exhibited good linearity for detecting tensile strains, up to a few mm.

2.1.3 Sensor Geometries

While sensor performance can be enhanced depending on material choice, sensor geometry also has a strong influence and varies widely across flexible piezoresistive sensors in literature [38], [39]. Some examples for flexible strain sensing include spider-web structures [28], mogul patterns [86], and microdome arrays [87]. One unique category of geometries is cellular structures, which are defined by open or closed cell lattices connected by struts or sheets. These are advantageous for flexible strain sensors due to their low apparent density [32], high deformability [88], and increased surface area for nanomaterial coating. As discussed in the previous section, while AM provides great design flexibility, it can be challenging to print some cellular structures with shallow overhangs. For this reason, self-supporting cellular structures such as TPMS are preferred sensor geometries for AM fabrication.

TPMS structures are defined by continuous minimal surfaces that repeat periodically along three orthogonal coordinates and do not self-intersect. Many TPMS variants exist, such as gyroid (G-), diamond (D-), and primitive (P-) types (see Figure 2.2a), where their surfaces can be described by an implicit equation. For example, Equation (2.4) is used to define the P-type TPMS implicit surface.

$$A = \cos\left(\frac{2\pi x}{a}\right) + cos\left(\frac{2\pi y}{a}\right) + cos\left(\frac{2\pi z}{a}\right) \tag{2.4}$$

where A is an isovalue that controls the sensor volume fraction V_f, a is the unit cell size, and x, y, and z are three-dimensional cartesian coordinates (see Figure 2.2a). TPMS implicit surface definitions can be used to either create sheet or strut-based structures. Sheet-based structures are formed by increasing the thickness of the implicit surface from a non-zero value (Figure 2.2b), while strut-based

structures fill the entire volume contained by the surface boundary (Figure 2.2a). As shown in Figure 2.2, the structures can be described by discrete unit cells patterned into a grid. Besides their suitability for AM fabrication, TPMS is touted in the literature for their distinct advantages such as multifunctionality, tunability, high surface area to volume ratios, enhanced mechanical properties, and structural light-weighting [89], [90]. Tunability of TPMS is also particularly advantageous, as its parameters (such as volume fraction, unit cell size, etc.) can be altered using optimization strategies to design an application-specific optimal geometry. A significant advantage of TPMS geometry for sensors is its compromise between compliance and stiffness. TPMS structures have a high specific stiffness [89], while pores in the structure facilitate the flexibility required to achieve high strains.

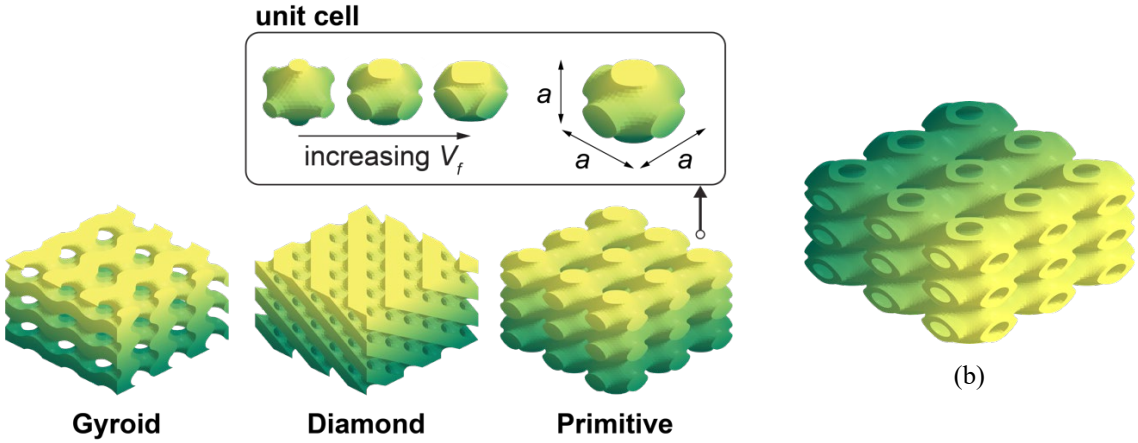

(a)

(b)

Figure 2.2. (a) Example TPMS structures including gyroid, diamond, and primitive types comprised of 3x3x3 unit cells. A P-type unit cell with dimensions and changing volume fraction is shown in the upper right. (b) Sheet-based P-type structure for comparison.

Due to the complex range of TPMS geometries, both strut and sheet-based, studying their deformation mechanisms during quasistatic loading is a topic of interest. Maskery et al. [91] modeled and tested nylon strut-based TPMS samples under uniaxial compression. They concluded that the deformation mechanism for G-type and D-type structures is bending-dominated, while P-type structures are stretching-dominated. They also found that using the compressive material modulus for modelling (as opposed to a combination of compressive and tensile moduli) yielded better agreement between finite element analysis (FEA) and experimental results. Keshavarzan et al. [92] similarly concluded that the P-type structure deformation mechanism is stretching-dominated during testing of vat photopolymerization samples. TPMS structures have also been studied for their damping

properties in applications such as impact loading [93] and high-frequency acoustic damping [94], [95]. For strain sensing, structural damping implies undesirable energy losses, as these losses will reduce the signal intensity/strain sensitivity of the structure. However, attenuation and energy dissipation for TPMS are studied at very high acoustic bandwidths (>2000 Hz [94], [95]) and strain rates (2057 s-1 [93]). For this reason it is not well-known how significant their damping effects are at lower frequencies and strain rates. As well, damping is dependent on the specific TPMS geometries used. For example, AlMahri et al. [93] determined specific energy absorption of five sheet-based TPMS structures during impact testing at 33 m/s. S-diamond and G-type geometries were found to absorb more energy, while P-type absorbed the least. This is likely due to the P-type stretching-dominated deformation mechanism, as bending-dominated deformation is preferred for energy dissipation [96], [97]. Also, strut-based TPMS structures have also been shown to absorb less energy per unit volume than sheet-based structures [98].

Presently, mechanical testing of TPMS in literature has focused on quasi-static loading and some applications in vibration isolation and damping. However, flexible piezoresistive sensors with TPMS geometries have not been studied yet for vibration strain sensing. Thus, there is a need to study and understand TPMS geometries within the context of vibration strain sensing to determine their capabilities and any limitations.

2.1.4 Vibration Strain Sensing

Though less common in literature, some flexible piezoresistive strain sensors have been characterized for vibration strain sensing. Coskun et al. [99] developed a graphene elastomer-based sensor for vibration pressure sensing up to 300 Hz, and acoustic sensing at up to 20 kHz. The cellular structure fabricated using freeze-casting consists of small (~50 μm diameter) corrugated pores, likened to cork or honeycomb structures [100]. However, due to a sensor natural frequency at 33 Hz, the sensor's GF exhibited frequency dependence up to ~180 Hz during mechanical vibration tests [99]. It is desirable to have a frequency independent sensor for a defined frequency range, as this ensures the relationship between strain input to sensor signal output will be unaltered by the excitation frequency. Also, the methods presented by Coskun et al. [99] perform vibration testing via base excitation of the sensor with a small mass attached to its opposite free end. Thus, the base excitation indirectly applies a force to the sensor via the attached mass. However, this method cannot directly control strain amplitude easily. As well, this experimental setup assumes that the mass only

travels in-line with the vibration direction, such that the sensor is uniaxially strained. Thus, parallelism of the sensor surfaces and centering of the mass on the sensor must be well controlled to ensure no force imbalances introduce non-axial strains. Also, Qiu et al. [32] presented pressure vibration testing of a similar sensor which showed fast response times and good stability when statically loaded. For example, the signal delay of the sensor at 20 Hz was < 2.0 ms. The authors tested a wide vibration bandwidth of 20-2000 Hz for pressure sensing, and presented results for discrete test frequencies in the time domain. Sensitivities were not presented in the frequency domain, which makes it hard to verify frequency independence. In addition, the authors used an electrodynamic shaker that was not able to control vibration amplitude independent of frequency. Thus, the authors could not gain any insights about strain amplitudes and strain sensing ranges during vibration testing. The practical limitations in [32], [99] can be addressed by considering alternative experimental methods. It is also noted that the sensors in [32], [99] are graphene hydrogels, not CPCs, but still exhibit flexible piezoresistive strain sensing capabilities. Flexible piezoresistive sensors have also been developed and tested only for acoustic measurements, though they do not present any characterization for frequency dependence for testing at high strain vibrations (e.g. >1% strain) [101], [102].

Low frequency cyclic loading of CPCs (typically < 1 Hz) has also been shown to require a conditioning period where stress softening occurs [69], [75], [103]. Here conditioning refers to cyclic straining of the sensor until its performance stabilizes. This is attributed to the Mullins effect, which is hypothesized to be due to effects such as bond rupture, molecule slipping, and polymer chain disentanglement [104], [105]. However, the main mechanism(s) have not been conclusively agreed upon in literature [105], [106]. The stress softening stabilizes after multiple cycles, and is also dependent on the maximum strain the material has been subjected to [105], [106]. A similar deterioration of CPC performance has been quantified due to Payne effects [107], [108]. Payne effect describes the behaviour of decreasing storage modulus with increasing strain for CPCs, due to polymer chain damage by filler interaction [109]. Thus, CPCs should be cyclically pre-conditioned at their expected maximum strain until their behaviour stabilize.

Overall, there is a great opportunity to expand on the limited research for flexible vibration strain sensors. While independently controlling frequency is done for flexible piezoresistive sensor characterizations in literature, to the author's knowledge vibration amplitude is not independently controlled. While strain amplitude is controlled in quasistatic strain measurements, these results

cannot necessarily be extrapolated to vibration strain sensing. This is because material properties such as loss factor and dynamic moduli have been shown to be both frequency and amplitude dependent [108], [110]. Thus, there is an opportunity to study the effects of frequency *and* strain amplitude, and their coupling, during vibration for flexible piezoresistive sensors. Additionally, frequency dependence has only been qualitatively discussed for flexible piezoresistive sensors in literature, without quantification of its effect on sensor accuracy. Similarly, sensor practicality can be determined better by calibrating the sensor according to its relationship between sensitivity and strain.

2.1.5 Adopted Flexible Piezoresistive Sensor

Previously, a flexible piezoresistive sensor employing TPMS was developed and fabricated using an FDM process by Davoodi et al. [15]. This sensor is defined by TPMS structures (D- and P-types), made using FDM printing of a sacrificial mould. The mould is used to embed GNPs in the surface of an SR matrix, creating a robust CPC capable of flexible piezoresistive strain sensing. In general, GNPs are a combination of monolayer, multilayer, and nanostructured graphene. Since the number of graphene layers in GNPs is not strictly controlled, their production is much more scalable and affordable [111]. This makes them advantageous for CPCs, combining greater affordability with good electrical conductivity and mechanical toughness [111]. The sensor in [15] was tested under cyclic (< 10 Hz) and quasi-static strains, displaying high durability, a GF up to 10, and good humidity stability. This use of FDM to create the sensor mould is advantageous over direct FDM/DIW printing, as the cast SR matrix material does not have issues such as interlayer-adhesion, material anisotropy, or high porosity.

In addition, there are other motivations to characterize this sensor for vibration strain sensing. First, the sensor is well-suited to measure dynamic strains compared to static strains. This is because of polymer matrix stress relaxation that occurs during static loading, causing changing electrical resistance during static strains [36], [69], [87]. Second, the sensor's surface coating is well-suited for dynamic strain measurements. Due to the Payne and Mullins effects, limiting the nanomaterial particles to near the surface will reduce this damage to the matrix, making it well-suited for high frequency cyclic strain sensing. As well, embedding graphene within the matrix enhances its robust behaviour [15], [47], [101]. For these reasons, the sensor fabrication process and design used in [15] is adopted for this work. While this sensor shows good performance under low strain-rate cyclic

loads, its competency for vibration strain sensing has yet to be explored. In addition, its use of TPMS and AM-based fabrication provides great flexibility for the sensor design to be later optimized.

2.2 Design Optimization

To improve product performance, optimization is an important step of any design workflow [112], [113]. AM particularly enables designers to optimize performance through design shape and size, hierarchical complexity, and functional complexity [114]. Hierarchical complexity refers to designing the AM part at multiple length scales, including the mesoscale and macroscale, and functional complexity refers to designing multifunctional parts. Thus, it is desirable to optimize the sensor's structure for improved performance in vibration strain sensing. However, formal design optimization of flexible piezoresistive sensors has not yet been addressed in literature. While great attention has been dedicated to improving performance through altering sensor materials, processes, and geometries, this has been done so far based on designer intuition [30]. Thus, while designs may be improved this way, they have not been optimized. This presents an opportunity to optimize the TPMS structures used for this sensor, accounting for advantages and constraints of AM by using design for additive manufacturing (DfAM) principles. Here the optimization of cellular TPMS structures is discussed, addressing suitable methods and algorithms.

2.2.1 TPMS Design Optimization Methods

For many cellular structures, including TPMS, it is possible to optimize them via functional grading. This is done using a field-definition for the structure, such that the structure is varied in 3D space to achieve locally tailored properties. For example, parameters such as volume fraction or strut diameter of cellular structures have been altered using a density-field definition in literature [115]-[118]. An example of this is shown in the right-most image of Figure 2.3, where a cellular structure is functionally graded for a simple bracket design. This example uses a topology optimization strategy for compliance minimization of the bracket, constrained to a 30% volume fraction. Different types of cellular lattices may also be blended gradually using a sigmoid function [97], [119]. To find an optimal functional grading for cellular structures, topology and size optimizations can be employed. These can be applied in isolation for a design or used together [120].

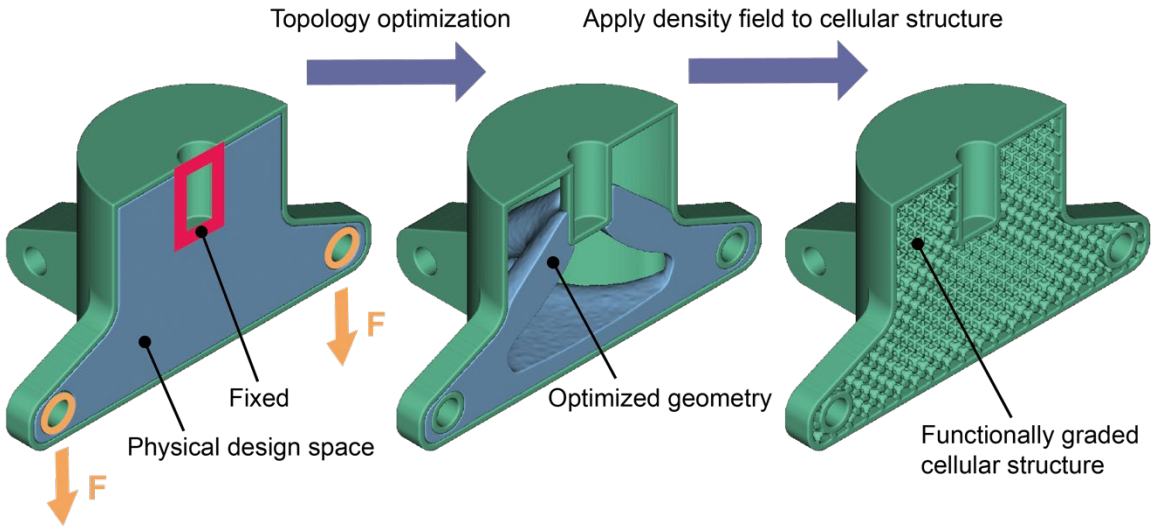

Figure 2.3. Topology optimization process for defining a functionally graded cellular structure. Cross-sections of a bracket are shown for a compliance minimization objective under a 30% volume fraction constraint.

Topology optimization strategies are used to determine the placement and connectivity of material within a predetermined physical design space. This method is popular in literature because of its general flexibility which provides greater opportunity for optimality improvements [121], [122]. However, care must be taken to implement any manufacturing constraints required for the optimization beforehand, such as minimum feature size, overhang restrictions, and avoiding closed volumes [121]. Also, topology optimization can produce esoteric geometries with bumpy surfaces, which often require post-processing to smooth surfaces and modify the body for its application. In addition, the size of the physical design space and any boundary conditions (BCs) must be defined beforehand in topology optimization. Pre-determining the size and location of BCs can be an undesirable constraint on the design, as these definitions may be flexible for the design. For the example bracket topology optimization in Figure 2.3, the locations of forces and fixed BCs must be pre-determined and are fixed during the optimization. After completing the optimization, the optimized geometry can be used to define a density field. This field can be combined with a cellular structure to spatially vary their dimensions, such as strut diameter or volume fraction [115], [123], [124]. In the example given in Figure 2.3, the density field used mandates larger strut diameters in areas where the optimal geometry was located. Another disadvantage of this method is that the cellular geometry definition is applied as a post-processing step in the optimization and is not considered during the topology optimization.

Conversely, a size optimization methodology is used to determine design dimensions. Again, changing the strut diameter in cellular structures is a common example. Similar to how size optimizations have been used for optimizing truss structure member sizes [125], [126], cellular structures' parameters can be optimized with this method. Here, altering design parameters such as TPMS volume fraction and unit cell size is also considered to be size optimization. An advantage of size optimization is the ability to combine cellular structure parameters (such as volume fraction) and part dimensions within a single optimization. It also does not mandate the designer to define a physical design space and BC locations beforehand, compared to topology optimization. However, size optimizations can be more computationally expensive than topology optimizations [127], so they should only be used when providing additional value. This thesis uses size optimization for defining an optimal TPMS sensor structure.

2.2.2 Metaheuristic Algorithms

To implement a size optimization, an effective optimization algorithm should be chosen. Due to the shape complexity of TPMS structures, FEA must be used to determine their structural properties. In this case, metaheuristic algorithms are particularly advantageous because they do not require any gradient information to be used. This enables them to be used with "black box" objective function evaluations, such as FEA. In general, "heuristic algorithms" is a general descriptor for algorithms that use problem-specific information to inform an optimization process towards a near-optimal solution. In contrast, metaheuristic algorithms apply heuristic methods within a more general strategy, such that they can be applied to many different problems. They are often created based on an analogy to a naturally occurring process, such as evolutionary or swarm behaviour, for the purpose of solving optimization problems.

Metaheuristic methods are generalized, efficient methods for finding near-optimal solutions in a design space [128], often used to reduce optimization times. Here, the design space is defined as the set of feasible solutions to an optimization problem. Almost any optimization will have practical constraints (e.g. fabrication or financial constraints) which act as boundaries on the design space size. In general, metaheuristic algorithms work by employing concepts of "exploration" and "exploitation" to balance between design space exploration and fast convergence. Exploration refers to the need for the design space (an n-dimensional space containing all valid solutions for n variables) to be searched thoroughly. This helps ensure the algorithm does not stagnate in an optimal local region. Exploitation

refers to the need to converge quickly on the optimal solution(s) and prevent wasted computation time. Algorithms do this by using the information of current and past generations to inform future generation locations in the design space. The execution of these concepts varies widely between metaheuristic algorithms, which largely accounts for their differences in performance [129]. For example, genetic algorithms (GAs) use the concept of natural selection as an analogy to describe their design . Here, a population of candidate solutions is generated in the design space and ranked according to how well they satisfy the optimization objective. To implement exploitation, GAs sequentially create new generations of solutions by combining the characteristics of the previous best-performing solutions. This new generation of solutions, or "offspring", inherit the best characteristics of their ancestors and should gradually converge to the optimal solution(s) with increasing generations. Exploration is maintained in GAs by using a concept of mutation, where characteristics of the new offspring are altered at a random probability to maintain population diversity.

Many interesting and practical applications of metaheuristic algorithms require a multi-objective optimization method. Multi-objective optimizations require a way to compare and/or quantify the tradeoff between the objectives. A simple way to find one optimal solution for a multi-objective problem is the weighted sum method, where objectives are assigned weighting coefficients that symbolize their importance (a larger magnitude coefficient indicates larger importance). For n objectives, a minimization problem using the weighted sum method can be described by Equation (2.5):

$$\min f(x) = \sum_{i=1}^{m} w_i f_i(x) + \cdots + w_m f_m(x) \tag{2.5}$$

where $f_i(x)$ is an objective function with weighting w_i, and $f(x)$ is the objective function value used to define optimality. However, this method assumes the objective space, a m-dimensional hyperspace described by the objective functions, is convex. If this assumption cannot be guaranteed in advance, Pareto dominance conditions are commonly used. These conditions divide a set of potential solutions into categories of "dominated" and "non-dominated". A non-dominated solution is defined as a solution where no improvement to a single objective function can be made, without worsening any other objective function value(s) [130]. This group of non-dominated solutions is referred to as a Pareto front in the objective space, and a Pareto set in the design space. An example Pareto front for a

minimization problem and 2D objective space is shown in Figure 2.4. Once the algorithm converges, the designer is left to choose a preferred solution from the Pareto front.

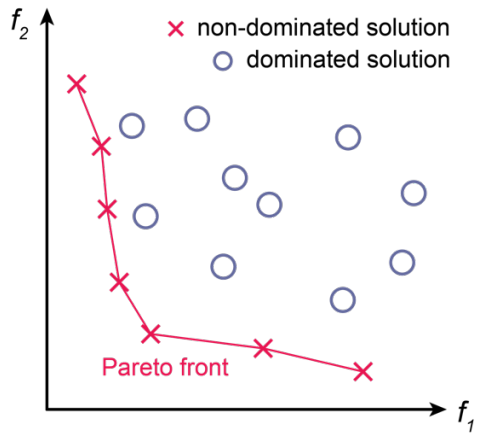

Figure 2.4. An example 2D objective space for a minimization optimization problem, showing the Pareto front of non-dominated solutions.

2.2.2.1 Firefly Algorithm

A promising metaheuristic algorithm is the FA developed in 2008 by Yang [131]. This algorithm is based on the communication swarm behaviour of fireflies in nature, where fireflies attract each other based on their light signals, and has been shown to outperform particle swarm optimization (PSO) and GAs [131]. FA has been popular in applications of engineering design problems. For instance, Gandomi et al. [132] solved several mixed continuous/discrete structural size optimization problems, including for a pressure vessel and welded beam. The authors demonstrated that it outperformed simulated annealing, harmony search, GA, and PSO algorithms. Discrete value optimization problems can often occur in practical size optimizations, where only certain dimensions of stock materials are available. The treatment of discrete value optimization problems can be handled using different methods, including penalization and rounding off number [133]. For engineering optimization problems using computationally expensive function evaluations, continuous design spaces are often discretized to reduce the design space size [134], [135]. This helps to limit the number of function evaluations (NFE) required when solving an optimization problem and is referred to as a metamodelling approach.

Many FA variants have been explored in the literature to provide performance improvements or target specific optimization types. For example, Baykasoglu and Ozsoydan [136] developed an

adaptive FA that introduces additional conditions that reduced firefly motions by ~26%. They also present an incumbent local search near the top-ranked fireflies to slightly improve the optimality of solutions [137]. A disadvantage of the methods used in [137] is that together they require a lengthy setup and definition of many algorithm parameters. Compared to other non-metaheuristic optimization algorithms, the basic FA is already considered to have high number of parameters [138]. Among important parameters, swarm-based algorithms such as FA require a number of fireflies to be defined for exploring the design space. It is important to choose an appropriate population number, as oversizing will result in excessive function evaluations and under-sizing will cause the algorithm to fail to explore the design space. For lower-dimensional design spaces, populations of 30-60 are generally suggested for swarm-based metaheuristic algorithms [139]-[141]. FA has also been successfully combined with other metaheuristic algorithms to improve on their individual benefits [142], [143]. Multi-objective firefly algorithms (MOFA) have also been developed by implementing Pareto optimality conditions [144], [145]. A detailed discussion of the MOFA algorithm parameters and implementation is given in Section 3.2.2.

2.3 Contribution Summary

As noted from the literature, it seems there are no studies on the characterization of a flexible piezoresistive sensor with TPMS geometry under vibration strains. To fill the gap, the first part of this manuscript presents the characterization of a flexible piezoresistive sensor with TPMS geometry for vibration strain sensing. This is the first characterization of a TPMS geometry for vibration strain sensing. Results are presented in both frequency and time domains, observing sensor behaviour as a function of frequency and strain. As well, current research for vibration strain sensing is expanded on by quantifying the sensor accuracy due to frequency dependence. Additional topics such as sensor signal delays and deformation mechanisms are also discussed.

The second half of this manuscript presents a size optimization of a TPMS geometry sensor for vibration strain sensing. A MOFA is implemented to maximize the sensor's frequency independence and strain sensitivity. This is the first formal design optimization of a flexible piezoresistive sensor in literature. The AM mould-based fabrication process and surface coating create additional unique challenges for this optimization process. In general, many flexible piezoresistive sensor variants have been shown to exist in literature. Thus, an approach is defined such that it can be adapted to different conductive nanoparticle networks and sensor geometries.

Chapter 3
Materials and Methods

This section outlines the experimental methods and materials used for the sensor fabrication, characterization, and optimization. Here the reference sensor design that is initially characterized is referred to as the "benchmark" sensor, in order to distinguish it from any optimized design(s) introduced later. If the sensor type is not specified, then the statement is true for either sensor type (e.g. fabrication processes are the same for all sensors).

3.1 Sensor Fabrication and Material Characterization

For the sensors fabricated and studied, the strut-based P-type surface defined by implicit Equation (2.4) is used. This TPMS type was chosen as it performed well in [15], has lower energy damping as discussed in Section 2.1.3, and has also been shown to have higher endurance for cyclic compressive loading [92]. The sensor is also trimmed radially to make a cylindrical, axisymmetric shape, resulting in the fabricated benchmark sensor shown in Figure 3.1a. The cylindrical porous sensor has unit cells 3.3 mm in size patterned in a 6×6×3 grid.

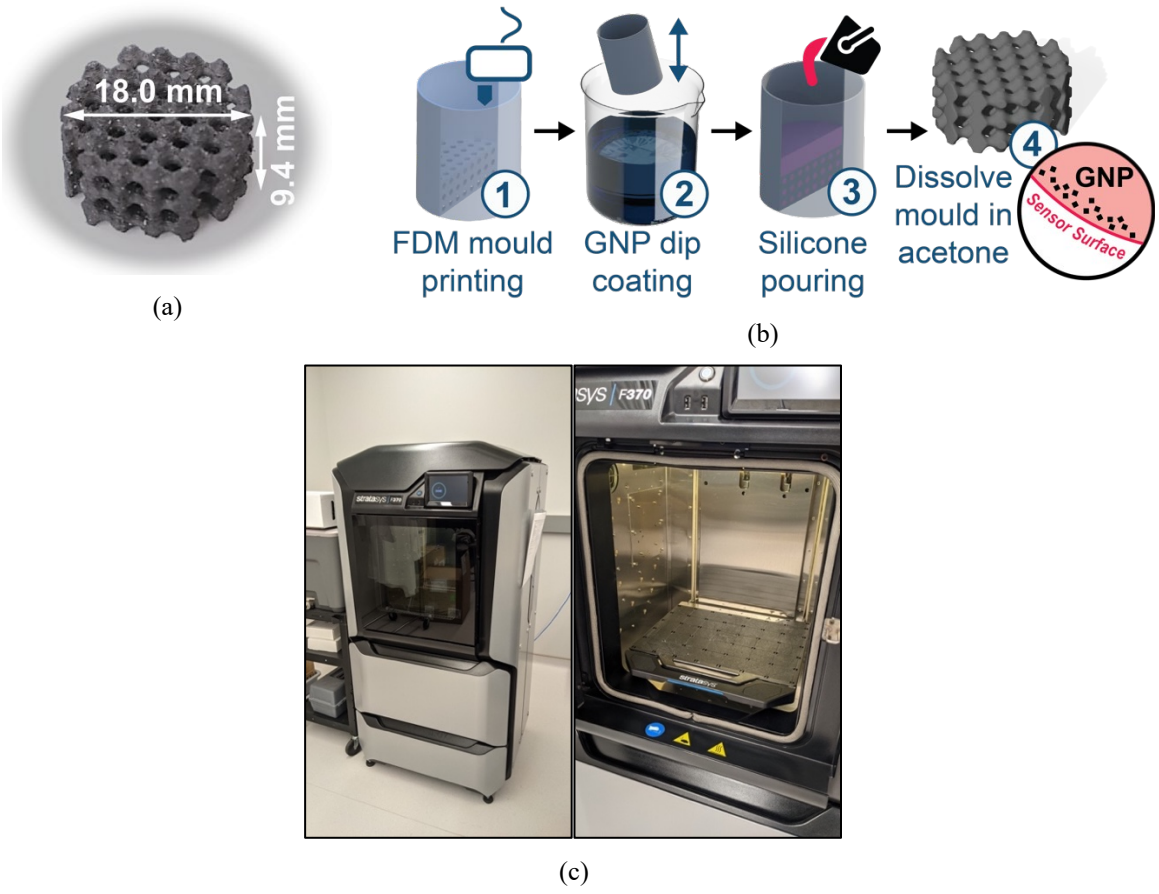

Figure 3.1. (a) Fabricated benchmark sensor with approximate height and diameter. (b) Main process steps for sensor fabrication. (c) F370 FDM printer and interior print bed.

The sensor fabrication repeats the AM-based sacrificial mould casting process and materials as defined in [15]. For continuity, the process is described here with a visual summary as shown in Figure 3.1b. First, FDM is used to create an ABS plastic mould. The FDM printer used for the benchmark sensor mould is the F370 (Stratasys, USA/Israel, see Figure 3.1c), and the FDM printer used for the optimized sensor mould is the M200 (Zortrax, Poland). The M200 is used for the optimized mould due to its higher layer resolution ($\geq$ 90 µm [146]), which enhances design flexibility. The mould is then dip-coated 20 times in a 99%-wt. isopropanol alcohol (IPA), 1%-wt. GNP solution. Between dips IPA is evaporated from the mould using convective heating, leaving deposited GNP on the surface. This dip coating process is comparable to drop-casting, which has been studied previously for fabricating polyimide and GNP CPCs [147]. After the dip-coating process, the GNP-impregnated mould is filled with a mixture of SR with 5% silicone thinner and

allowed to cure overnight at room temperature. While curing, the GNPs transfer and embed within the SR surface. Post-curing, the ABS mould is dissolved in acetone, leaving a highly flexible surface-embedded graphene (SEG) sensor. This sensor has a measurable electrical resistance, which changes when strained due to rearrangement of its nanoparticle network as outlined in Section 2.1.1

Scanning electron microscopy (SEM) images (VEGA3, TESCAN, Czech Republic) are presented in Figure 3.2 at different process steps during fabrication (4 kV SEM voltage). Figure 3.2a shows a cross-sectional image of the ABS mould after 3D printing, where printed layers are outlined by distinct ridges. This is the characteristic stair-step effect of many AM processes, which is a result of slicing 3D models into individual layers to be printed. Stringing is also visible in Figure 3.2a, and occurs when small strands of residual plastic can be left from the FDM extruder as it travels between deposition locations. These strands are generally removed before GNP coating by poking through the mould holes. Figure 3.2b shows the mould after being dip-coated in GNP. The additional layer thickness of the GNP coating that covers the mould smoothens its features when compared to Figure 3.2a. The visible presence of GNP across the surfaces confirms there is a comprehensive coating. Coating uniformity has been previously studied in [15]. Figure 3.2c shows a sensor unit cell after it has been removed from the mould. The sensor unit cell features are clearly formed, indicating a successful casting process completion, and it is noted that ridges from the mould are also transferred to the sensor. Figure 3.2d is a higher magnification image showing greater detail of the sensor surface. Here GNP is visible on the surface, confirming its transfer from the mould to the sensor surface. Additional photos of the sensor are also included in Appendix A, with detailed views of the sensor surface. Computed tomography (CT) scans (Versa 520, Zeiss, Germany) are also performed of the sensor using an 80 kV voltage and 20 μm voxel size. These results are presented in Section 4.1.2.1.

Raman spectroscopy was also used to validate the presence of GNP on the sensor. As supplied, the GNP flake thickness is 12 nm comprised of 30-50 graphene sheets (equivalent to graphite). A micro-Raman spectrometer (Ramascope, Renishaw, United Kingdom) equipped with a 633 nm, He-Ne laser measuring at a 0.5 cm^{-1} wavenumber resolution was used. The Raman spectra with major peaks labeled are presented in Figure 3.2e, and can be used to help confirm the presence of graphite. For monolayer graphene the 2D-band (~2700 cm^{-1}) tends to dominate due to a combination of phonon resonance modes [148], while G-band (~1580 cm^{-1}) dominance is characteristic of graphite and multi-layer graphene (ML-G) [149]. Here the first-order Raman scattering G-Band dominates the 2D-Band

by a factor of ~5, indicating graphite's presence. As well the 2D-band is typically shifted closer towards 2700 cm^{-1} for higher graphene layers when using a 633 nm laser [150]. This is another characteristic of the 2D-band measured here, which is at ~2673 cm^{-1}. Thus, there are multiple pieces of evidence that further confirm the presence of many graphene layers in the GNP surface coating. The D-band (found near 1350 cm^{-1}) occurs in graphene/graphite due to a double-resonance Raman scattering process [151]. One of these resonances is an elastic phonon emission caused by crystal defects, which increases the D-band intensity [152]. The D-band intensity in Figure 3.2e is smaller than the G-Band by a factor of ~6, indicating a low presence of defects [153], [154].

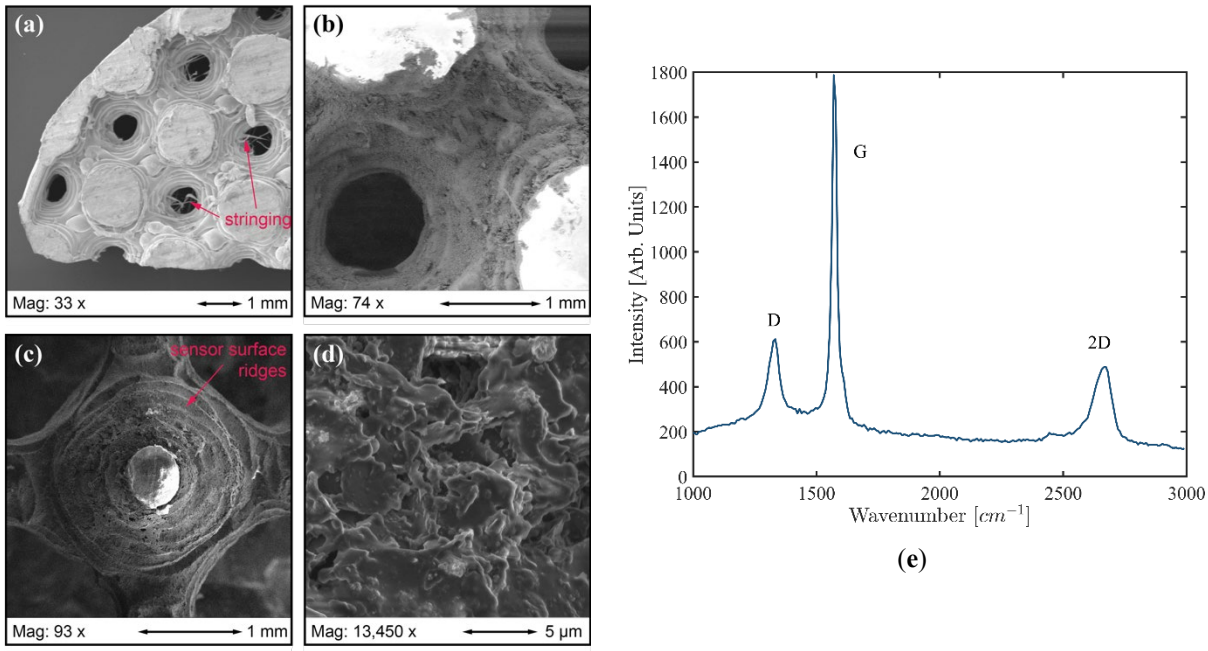

Figure 3.2. SEM images taken during fabrication process steps, and Raman spectroscopy of sensor. (a) SEM image of a cross-section of the 3D printed ABS mould. (b) SEM image of the mould surface after dip coating in GNP. Washed-out areas are due to the contrast of the light ABS plastic with the dark GNP coating. (c) SEM image of a sensor unit cell. (d) Sensor surface SEM image at higher magnification, showing GNP on the surface. (e) Raman spectra measured at the sensor surface with major graphene-associated bands labeled.

To determine the SR elastic modulus (E), four cylindrical samples of SR were fabricated and tested under compression according to ASTM-D575. Each sample was compressed at a rate of 12 mm/min up to 30% strain (see Figure 3.3a) using a tensile tester (Model 40, MTS Systems Corporation, USA).

The data in the linear region of material behaviour (< 10% strain) was used to determine the elastic modulus, E = 366 kPa (see Figure 3.3b).

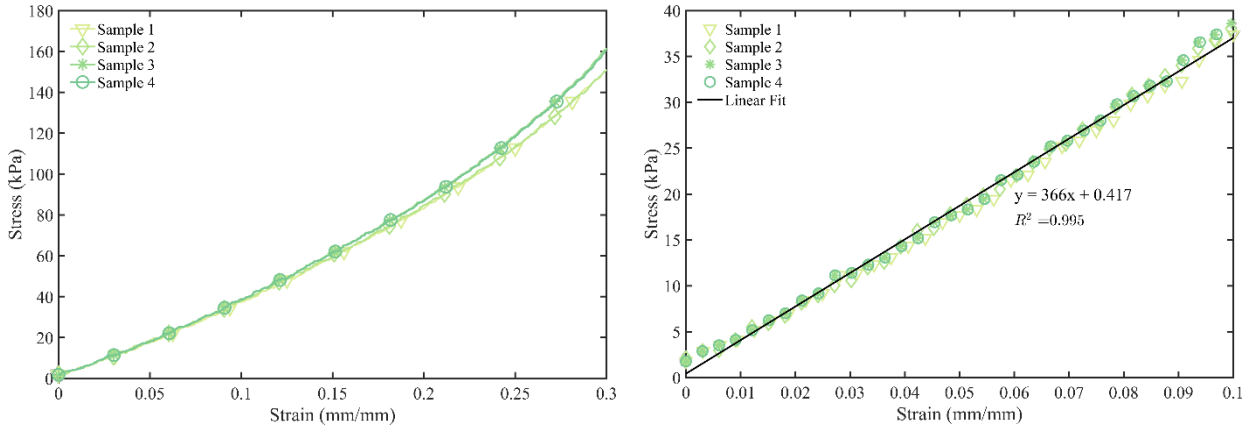

(a) (b)

Figure 3.3. Stress strain curves obtained from testing four SR cylindrical prism samples (a) Stress-strain curve for 0-30% strain. (b) Stress-strain curve for 0-10% strain. The linear fit used to determine the SR elastic modulus is also shown.

3.2 Experimental Methods

This section defines the experimental methods for testing the sensors under a range of strains and frequencies, followed by a detailed description of the optimization strategy, algorithm, and software used.

3.2.1 Dynamic Strain Testing

Figure 3.4a depicts the vibration strain test that a sensor is subjected to. With the sensor fixed on one end, a sliding condition is imposed on the opposite end, such that its motion is restricted to its axial direction (Z-axis). Before excitation, the sensor is pre-compressed by an initial strain (ε_o = 5% for all measurements presented here) to ensure the net strain of the sensor remains in a compressive state. During testing the vibrations oscillate around ε_o, enabling the sensor to be tested under net compression, up to 10% peak-to-peak compressive strain amplitudes (ε_{pk}). For any given test, the ε_{pk} is always kept constant. Both sine frequency sweep and dwell tests were performed to observe different sensor behaviours.

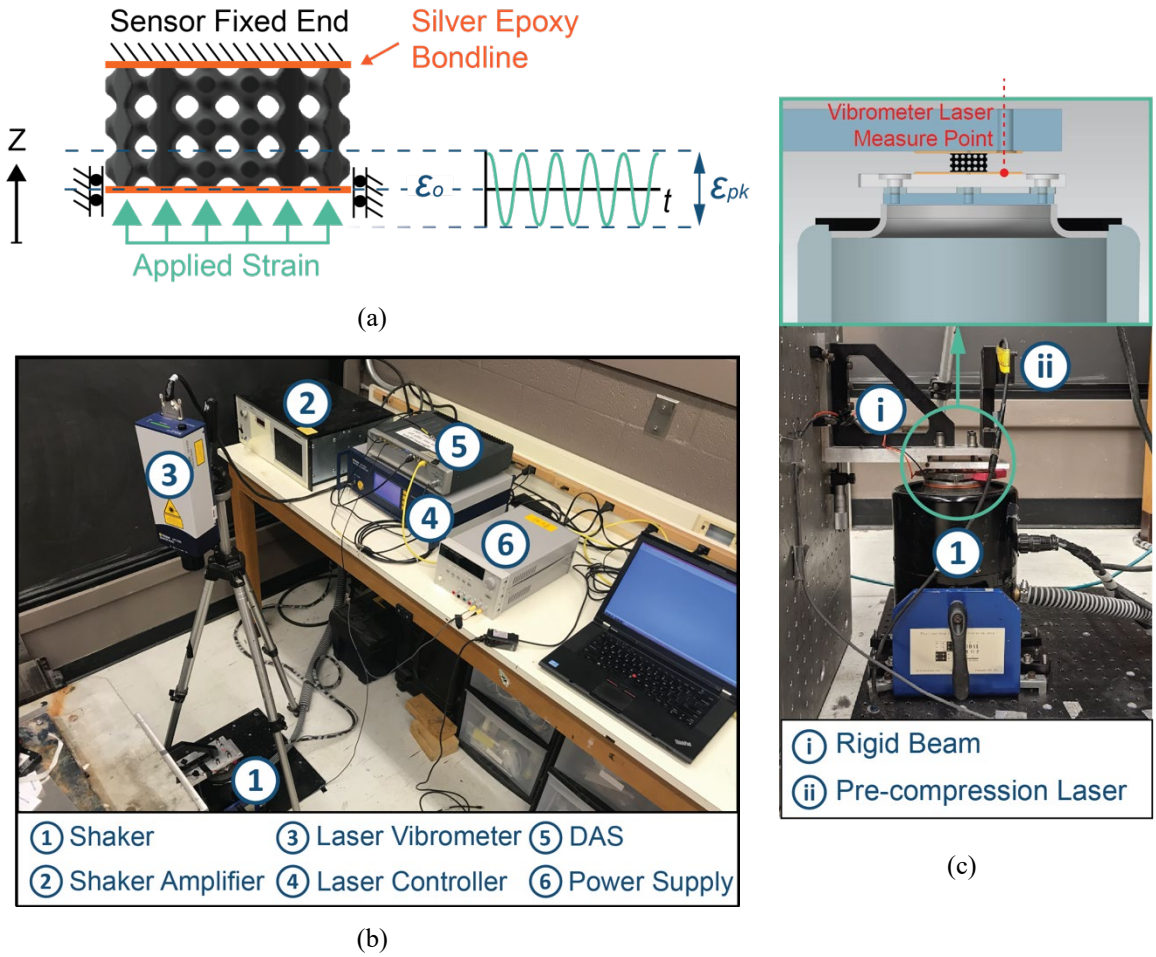

Figure 3.4. (a) Diagram of sensor BCs and test parameters applied during the vibration test. (b) Lab equipment used for vibration control and sensor signal measurement. (c) The shaker and fixture used to mount and pre-compress the sensor are shown. A cross-section view of the fixture also shows how the sensor is mounted and where the laser vibrometer measures its displacement.

To practically implement the desired test conditions, printed circuit board (PCB) plates were used as electrodes by attaching them to each sensor end using silver epoxy (see Figure 3.5 for photos of the sensor assembly). Afterwards, they were securely bolted to the test fixture. The experimental implementation is presented in Figure 3.4(b-c). The sensor is fixed to a rigid beam from above, while the bottom end is attached to an electrodynamic shaker (Model 2075E, The Modal Shop, USA). This implementation is shown for a cross-section view of the fixture (see the top of Figure 3.4c). The shaker is controlled in a closed feedback loop using a data acquisition system (DAS, SCM V8, Siemens, Germany). The DAS receives displacement data from the laser vibrometer and controller

(OFV-505 and OFV-5000, Polytec, Germany), and corresponds with the shaker amplifier (2050E09, The Modal Shop, USA) to control vibrations. This setup implements the test conditions in Figure 3.4a, however it is noted the shaker armature is flexure-based, which allows small lateral motion during testing. A power supply (E3631A, Agilent, USA) provides a fixed voltage (V_{in} = 8V), and the sensor voltage (V_{out}) is measured by the DAS such that the sensor resistance can be calculated. During setup the sensor pre-compression strain is measured and controlled using a secondary laser device (IL-100, Keyence, Japan) and micrometer, respectively. Once the desired ε_o is achieved by moving the fixture's rigid beam, the beam is then bolted in place. The main test parameters include ε_o, ε_{pk}, and excitation frequency (ω). Frequency sweeps were performed at 0.1 Hz/s and a resolution of 0.05 Hz. Unless otherwise specified, data was collected at a sampling rate of 6400 samples/s.

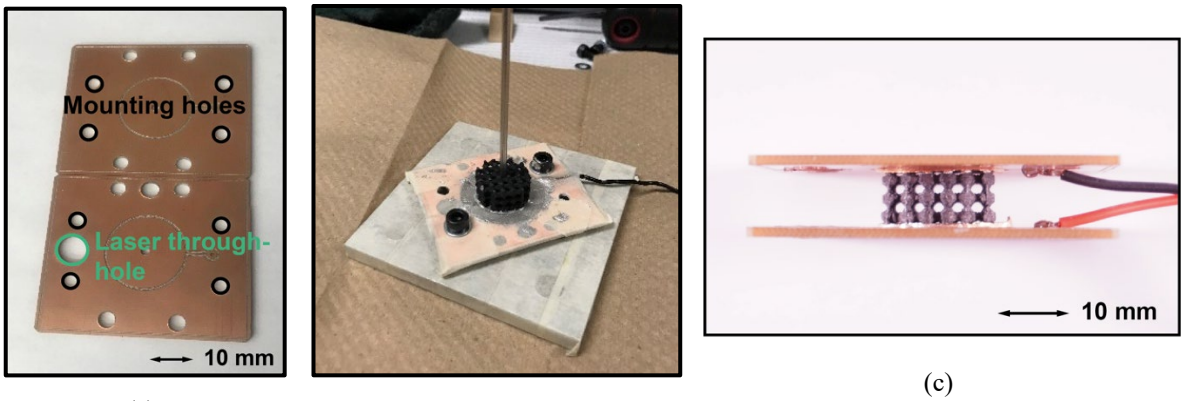

(a) (b) (c)

Figure 3.5. Additional fabrication images and steps during sensor electrode mounting. (a) Copper PCB Plates used to mount the sensor, which include mounting holes around the perimeter and a through-hole for the vibrometer laser path. (b) PCB after being coated with silver epoxy and attaching the sensor. The vertical shaft is used to orient the sensor squarely to the PCB. (c) Sensor mounted to both PCBs.

3.2.1.1 Sensor Resistance and Delay Measurements

A voltage divider is used to measure the sensor voltage and calculate its resistance (see Figure 3.6). Two leads are connected across the sensor to a high-impedance DAS to avoid significant voltage drop in the measurement. The DAS resolution is 24 bits, making it capable for sensing even very small voltage signals. The frequency response function (FRF) spectral data is collected for the sensor voltage change (ΔV_{out}) and applied displacement in mm. R_o is calculated as a function of frequency by averaging the nominal sensor resistance measured across the frequency range tested. Then the voltage divider Equation (3.1) is manipulated into Equation (3.2) which can be used to solve for ΔR.

$$R = \frac{V_{out} R_{ref}}{(V_{in} - V_{out})} \tag{3.1}$$

$$\Delta R = \frac{\Delta V_{out} \left(R_{ref} + R_o\right)^2}{R_{ref}(V_{in} - \Delta V_{out}) - \Delta V_{out} R_o} \tag{3.2}$$

Where R_{ref} is the electrical resistance of the constant reference resistor in the voltage divider, and R is the sensor resistance for a given V_{out} measured.

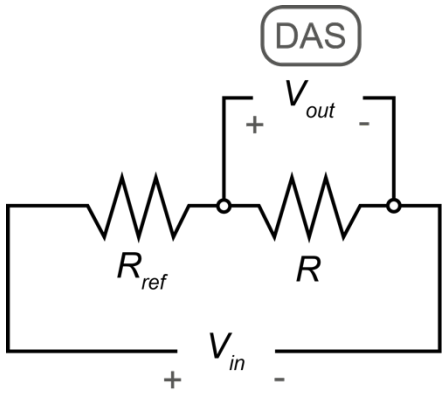

Figure 3.6. Voltage divider used to measure sensor electrical resistance.

Sensor signal delays are originally measured as a phase angle shift in radians, φ, between the input and output signals. Values are then converted to both temporal delays (δ_{time}) and delay as a fraction of the vibration period (δ_{period}), defined by Equation (3.3) and Equation (3.4), respectively. Here mod is defined as the modulo operator.

$$\delta_{time} = [\pi - mod(\varphi, 2\pi)]/2\pi\omega \tag{3.3}$$

$$\delta_{period} = [\pi - mod(\varphi, 2\pi)]/2\pi \tag{3.4}$$

3.2.1.2 Benchmark Sensor FEA

To help validate experimental data from dynamic strain testing, the benchmark sensor was modeled using the FEA software COMSOL. Material properties used for SR are given in Table 3.1, which were used assuming that the GNP surface coating does not significantly alter the mechanical properties. The SR elastic modulus (E) measured in Section 3.1 is used, and the same BCs were applied in the FEA as described in Section 3.2.1.

Table 3.1. Sensor material properties used in FEA.

Material Property	Value
E (kPa)	366
Poisson ratio, υ	0.47
Density, ρ $\left(\frac{kg}{m^3}\right)$	1280

3.2.2 Optimization Definition and Strategy

After characterizing the benchmark sensor, a size optimization is performed to find optimal design parameters that maximize its performance for compressive vibration strain sensing. The optimization problem is first defined, followed by describing the strategy used to solve it. For this optimization, two objective functions are considered:

1. Maximizing the first sensor natural frequency (Maximize $f_1 = \omega_{n,1}$)
2. Minimizing the normalized average principal strain on the sensor surface (Maximize $f_2 = -\bar{\varepsilon}'/\varepsilon_{pk}$)

where $\bar{\varepsilon}'$ is the average principal strain evaluated on the sensor surface. The first objective is chosen to improve the sensor frequency independence, which is a priority to improve dynamic strain sensing performance. The second objective is chosen as an additional goal of improving the strain sensitivity of the sensor. When the sensor is compressed, the GNP network is ideally compressed as much as possible to maximize its resistance change. So for this sensor's GNP surface coating, only compressive strains near the surface are required to be maximized, and strain within the sensor body can be ignored. Considering compressive strains to be negative here, the average principal strain evaluated on the sensor surface is multiplied by -1 to get -$\bar{\varepsilon}'$. This allows the compressive strains to be maximized and not tensile strains. This value is normalized by the compressive strain amplitude applied to the sensor (ε_{pk}) such that the objective function is represented as a fraction of the applied strain. As discussed in Section 2.1.1, regardless of the resistance change mechanisms for the sensor, strain experienced by the nanoparticle network will have a significant impact. This objective is easily implemented in the current commercial FEA software, and is chosen to accomplish the objective of improving strain sensitivity at a higher level of understanding. As a result, a benefit of this approach is that it is easily adaptable to different nanoparticle networks and does not require detailed knowledge of the network materials and connectivity. Both objective functions are black-box functions, since FEA is required to determine their values for a particular sensor design. Solving an

FEA problem is computationally expensive, so function evaluations will be the main contributor to this optimization algorithm's runtime. Thus, decisions made when framing the optimization problem primarily consider how to reduce the NFE, while still finding the global optimal solution.

3.2.2.1 Design Space Definition

The optimization design space is defined by 5 sensor design parameters:

1. Unit cell size, a
2. The number of repetitions of the unit cell along the horizontal (XY) plane, p_{xy}
3. The number of repetitions of the unit cell along the vertical (Z) axis, p_z
4. The sensor's volume fraction at its bottom (minimum Z), V_f^{bot}
5. The sensor's volume fraction at its top (maximum Z), V_f^{top}

The visual representation of these parameters is shown in Figure 3.7a. The sensor volume fraction is varied between V_f^{bot} and V_f^{top}, creating a functional grading for the TPMS lattice. Together these parameters create a 5-dimensional design space with associated constraints listed in Table 3.2. Each parameter has a lower and upper inequality constraint. Values of a are constrained between 3.3 to 4.5 mm, as very small values will not be printable, and large values will create oversized designs. V_f^{bot} and V_f^{top} are given the same general constraints between 0.40 and 0.66 to avoid creating extreme designs. When defining acceptable values of p_{xy} and p_z, limitations are indirectly imposed on them using sensor width ($15 \leq w \leq 27.5$ mm) and height ($6.5 \leq h \leq 11$ mm) constraints (see Figure 3.7a). Thus, given a unit cell size a, the acceptable integer values of p_{xy} and p_z can be determined using their respective equations in Table 3.2.

A size optimization is more suitable for this problem than topology optimization for two reasons. First, the sensor's major dimensions, and thus the location of its BCs may change. For example, if the sensor's height is changed, the location of the compressive strain BC will change. Topology optimizations cannot readily accommodate this change, as discussed in Section 2.2.1. Second, the strain on the sensor surface must be found in the optimization algorithm. Since this is unique to the TPMS geometry, the TPMS surface must be modeled. Topology optimization with lattices works by solving for the material allocation in the physical design space, and as a post-processing step, a

density field can be applied to a lattice to decide its volume fraction. This strategy cannot account for strain on the lattice surface during the optimization, since the lattice definition is not applied until afterwards. Thus, a size optimization is chosen to solve this problem.

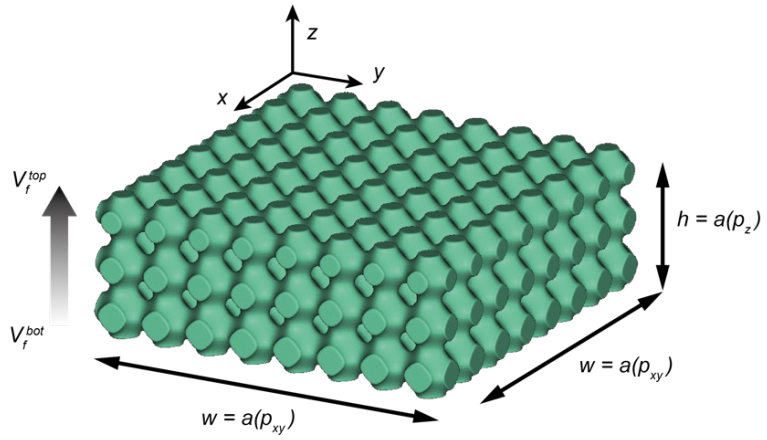

(a)

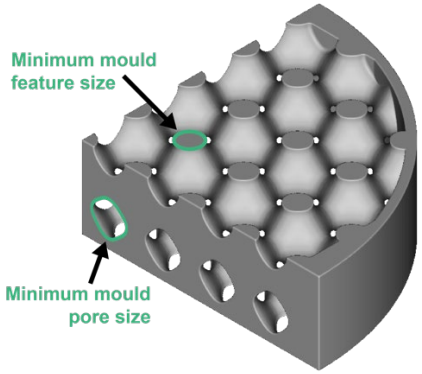

(b)

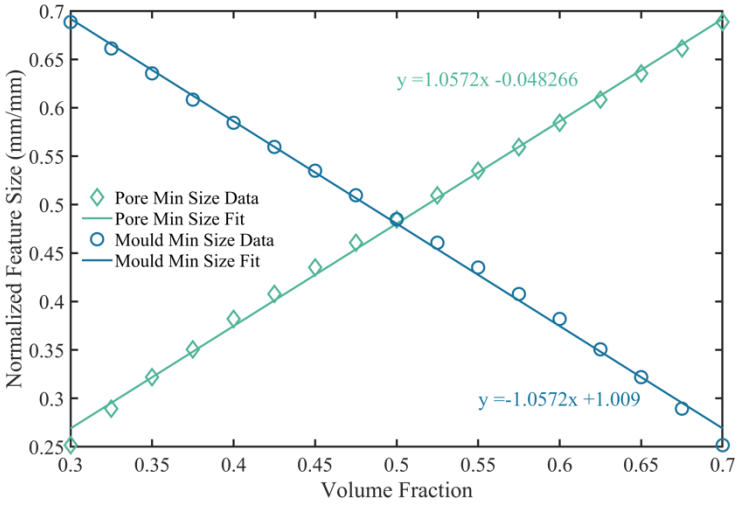

(c)

Figure 3.7. (a) Diagram of sensor parameters for an example geometry (before radial trimming). (b) Section of the sensor mould showing its minimum pore and feature size. (c) Sensor mould minimum pore and feature size plotted with respect to volume fraction. Data points are given a linear fit, with the equation of the line shown next to it.

Table 3.2. Design space parameters with associated constraints and intervals listed.

Parameter	Lower Inequality	Upper Inequality	Discrete Interval
a (mm)	3.3	4.5	0.1
p_{xy} [1]	$ceil(15/a)$	$floor(27.5/a)$	1
p_z [1]	$ceil(6.5/a)$	$floor(11/a)$	1
V_f^{bot} [2]	0.40 (V_f^{min})	0.66 (V_f^{max})	0.02
V_f^{top} [2]	0.40 (V_f^{min})	0.66 (V_f^{max})	0.02

[1] $ceil$ and $floor$ are operations for rounding up and down to the nearest integer number, respectively.
[2] Additional V_f constraints applied for some values of a (see Section 3.2.2.1.1).

3.2.2.1.1 Fabrication Constraints

Additional fabrication constraints can be imposed on the design, considering the sensor mould and sensor body fabrication process. In the FDM-printed TPMS mould, its open-cell lattice structure facilitates the travel of the GNP-IPA solution through the mould to apply a comprehensive coating. The pores of this structure have a minimum size (diameter) they must be above, or GNP may begin to clog the mould. Conversely, given the resolution of the printer being used, excessively small features will be unprintable or have very poor quality. Thus, both the mould pore and feature sizes have minimum dimensional constraints which require defining (see Figure 3.7b). These minimum dimensions were plotted as a function of the *sensor's* V_f in Figure 3.7c, where the pore/feature size is normalized by a. A linear fit is applied to each set of data points, showing that the two relationships are linear functions of V_f with the same slope magnitude. However, the pore size has a positive slope, and the feature size has a negative slope. For this reason, both very high and very low volume fractions are undesirable. From experience fabricating, the lower limit of mould pore size is chosen as 0.50 mm, and the lower limit of mould feature size is used as 0.85 mm (the Zortrax M200 printer has a minimum feature size of ~0.40 mm [146]). The equations for minimum and maximum volume fractions (V_f^{min} and V_f^{max}) given a are derived from their linear fits as Equations (3.5) and (3.6), respectively.

$$V_f^{min} = \frac{0.473}{a} + 0.045 \tag{3.5}$$

$$V_f^{max} = \frac{-0.804}{a} + 0.955 \tag{3.6}$$

Another consideration during sensor fabrication is that sensors will shrink during ABS dissolving in acetone [155], which can vary depending on the sensor geometry and soak time. Based on experience fabricating these sensors, ~10% volumetric shrinking is assumed to occur for any design, so the mould requires +10% volumetric scaling. To account for this, Equations (3.5) and (3.6) are modified by multiplying a by 1.10. Thus, given a, Equations (3.7) and (3.8) are used to find pore and feature size constraints on both V_f^{bot} and V_f^{top}, where pore size creates a lower inequality and feature size creates an upper inequality. If either of these constraints is within the general inequality range of $0.40 \leq V_f \leq 0.66$ previously defined, the pore/feature constraint becomes dominant and further restricts the design space. While these fabrication constraints were accounted for, for the given range of a values they never dominated the general V_f inequality constraints.

$$V_f^{min} = \frac{0.430}{a} + 0.045 \tag{3.7}$$

$$V_f^{max} = \frac{-0.731}{a} + 0.955 \tag{3.8}$$

As well, parameters are only allowed to take discrete values between their inequalities at a specified interval/resolution (see Table 3.2). Discrete values are used, as opposed to continuous values, to reduce the NFE required. Since small differences in parameter values will not significantly change design performance, it is not worthwhile to evaluate these small differences. As well, FDM printers have a limited resolution (0.09-0.39 mm [146] for the printer used here), so small changes in design parameters such as the unit cell size or volume fraction would be lost in the fabrication resolution. Further, the parameters p_{xy} and p_z are already required to be integers. Thus, there are a limited number of discrete values each parameter can assume, creating a finite number of candidate solutions in the design space (11,172 for this case).

3.2.2.2 Optimization Problem Definition

Given the objective functions and design space definitions, the formal optimization definition for this problem is written below. It is framed as a minimization problem by multiplying each objective by -1, as this the common convention for optimization problem definitions.

$$
\begin{aligned}
&minimize && f_1(X) = -\omega_{n,1},\ f_2(X) = \bar{\varepsilon}'/\varepsilon_{pk} \\
& && X = \begin{bmatrix} a & p_{xy} & p_z & V_f^{bot} & V_f^{top} \end{bmatrix}^T \\
&subject\ to && g_1(X) = a \leq 4.5 \text{ mm} \\
& && g_2(X) = a \geq 3.3 \text{ mm} \\
& && g_3(X) = aw \leq 27.5 \text{ mm} \\
& && g_4(X) = aw \geq 15\text{mm} \\
& && g_5(X) = ah \leq 11 \text{ mm} \\
& && g_6(X) = ah \geq 6.5 \text{ mm} \\
& && g_7(X) = V_f^{bot} = V_f^{top} \leq 0.66 \\
& && g_8(X) = V_f^{bot} = V_f^{top} \geq 0.40 \\
& && g_9(X) = V_f^{bot} = V_f^{top} \leq \frac{-0.731}{a} + 0.955 \\
& && g_{10}(X) = V_f^{bot} = V_f^{top} \geq \frac{0.430}{a} + 0.045
\end{aligned}
$$

3.2.2.3 Multi-Objective Firefly Algorithm Strategy

To solve the optimization problem defined, a MOFA is implemented as introduced in Section 2.2.2.1. The algorithm works by generating an initial population of candidate designs, where each candidate is referred to as a "firefly". In a n-dimensional design space, the location of firefly i is described by X_i, which is a vector of n sensor design parameter values. Within a finite number of k_{max} generations, defined at the algorithm start, these fireflies move each generation to explore the design space and eventually converge on any optimal solution(s). The firefly motions are described by several components, which are discussed here.

To implement exploitation in the MOFA, each firefly compares itself to the rest and will only move towards fireflies that have better objective function values ("brighter" fireflies). When comparing fireflies, the relative improvement in either objective function is considered to justify motion. This exploitation term is defined for motion t of firefly X_i^t moving towards X_j^t by (3.9) and (3.10):

$$\beta = \left[\beta_o^a + \beta_o^b e^{\left(\frac{-4.605k^2}{k_{max}^2}\right)}\right] e^{-\gamma r^2} \tag{3.9}$$

$$r = \left\| X_i^t - X_j^t \right\| \tag{3.10}$$

where β describes the exploitation motion magnitude, comprised of constant and decaying terms β_o^a and β_o^b, k is the current generation, and r is the Euclidean distance between X_i^t and X_j^t. Firefly motion described by β partially decays with the increasing generation, as defined for the β_o^b term, in order to promote convergence at higher generations. As well, a unique part of FA is the exponential decay of firefly "brightness" in the design space, which is described by the constant γ in the term $e^{-\gamma r^2}$. This decay is analogous to exponential decay of light intensity in 3D space. Thus, fireflies are more likely to be influenced by those nearby them in the design space than those far away. To avoid premature convergence on a local optimum, exploitation must be balanced in the algorithm by good exploration of the design space. To do this, firefly motion magnitude also has a random component α described by Equation (3.11). This is an adaptation of the sigmoid technique used in [156], which allows greater initial exploration of the design space before quickly decreasing towards zero. The magnitude of random motion decays with increasing generation, such that the exploitation terms become more dominant and causes the solution to converge. The random motion for move t is described by Equation (3.12).

$$\alpha = \frac{\alpha_o}{1 + e^{0.05(k-150)}} \tag{3.11}$$

$$\alpha_i^t = \alpha \epsilon_i^t \tag{3.12}$$

where α_o is a constant describing the random motion nominal magnitude, α_i^t is the random motion of firefly i described by an n-dimensional vector, and ϵ_i^t is another n-dimensional vector, where each value is randomly sampled from an even distribution within [-1, 1]. Combining exploitation and exploration terms, the firefly motion to its new location X_i^{t+1} is thus described by Equation (3.13).

$$X_i^{t+1} = X_i^t + \beta\left(X_j^t - X_i^t\right) + \alpha_i^t \tag{3.13}$$

To accommodate firefly motion in the design space, a few changes are noted here. First, since the length scales of each parameter vary significantly (e.g. V_f is always less than 1 but p_{xy} can take values of up to 8), the design space is scaled in each dimension to only take values between 0 and 1. This ensures that firefly motions are unbiased in direction and magnitude, and do not require custom scaling for each dimension. This also ensures the exponential brightness decay is equal in all design space dimensions. As well, it was noted earlier that design space parameters are only allowed to

assume discrete values. Thus, the design space of acceptable points can be described as a discrete grid (X^{grid}) where fireflies may only exist on a grid point. For this case, the resolution of this grid is not very fine; for example, p_z only takes values of 2 and 3. As a result, firefly motions of smaller magnitudes can be lost within the grid resolution. This can result in an undesirable reduction of firefly motion and promote fireflies to get stuck at local optima. To prevent this, a dual representation of the firefly's location in the design space is used:

- For firefly motions: The *continuous* design space X^{real} is used, where fireflies can move to any location, including locations not on X^{grid}.
- For function evaluations: The *discrete* design space X^{grid} is used, where fireflies' function values are determined by using their nearest point in X^{grid} (compared to their location in X^{real}).

Thus, firefly locations are simultaneously described in the continuous and discrete design spaces, X^{real} and X^{grid}. This allows free motion of the fireflies within the design space while maintaining a reduced NFE. To accommodate this rule, fireflies are not allowed to move to near a grid point that is already occupied. As an example, consider the motion of firefly "A" in a 2D design space as shown in Figure 3.8. It has two design point representations, X_A^{grid} and X_A^{real}, and is allowed to move anywhere within the design space, not bound to the grid. However, if it tries to move nearby a grid point that is already occupied, this motion is considered invalid and is rejected. In this example, firefly "B" is already occupying a point X_B^{grid}, so a motion near this point is invalid. This prevents fireflies from occupying the same discrete candidate design point. Last, it is noted that fireflies are allowed to travel outside of the design space boundaries, but their objective functions are heavily penalized to encourage their return to the design space.

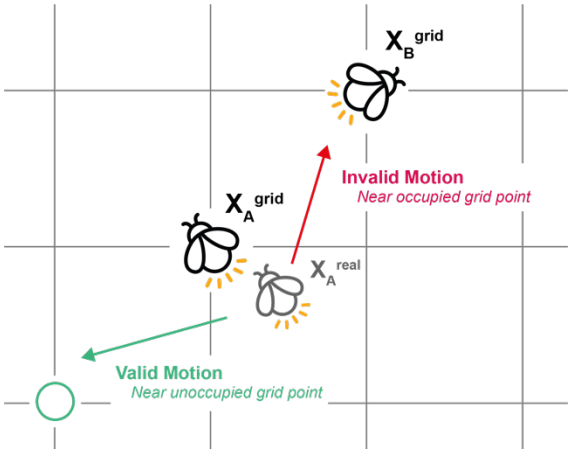

Figure 3.8. Firefly motion example with fireflies A and B in a 2D design space with a discrete grid X^{grid}. Examples are shown for valid and invalid motion of firefly "A".

For the multi-objective optimization, its objective space convexity cannot be guaranteed, so a weighted sum method combining the objective functions cannot be used. Instead, Pareto dominance conditions are used to find the Pareto front and then select any desirable solutions from it. Thus, each generation the fireflies are ranked according to their Pareto dominance. To help preserve the best (non-dominated) fireflies between generations, an elitism strategy defined by Baykasoğlu and Ozsoydan [137] is also imposed, defined by Equations (3.14) and (3.15):

$$\varsigma = \frac{mod(k-1, k_{max})}{k_{max}} \tag{3.14}$$

$$\xi = (rank_i)^{-\varsigma} \tag{3.15}$$

where ξ is a threshold value for firefly i, described by the generation parameter ς and firefly rank ($rank_i \in \mathbb{Z}^+$). A rank one firefly represents a non-dominated solution. Before firefly motion, parameter ξ is compared to a random number $\tau \in [0,1]$. If τ is less than ξ, firefly motion is permitted. Thus, a smaller value of ξ indicates that the firefly is less likely to move, such that non-dominated fireflies have a reduced likelihood of motion, which increases with the generation.

Algorithm parameter values are defined beforehand and listed in Table 3.3. As discussed in Section 2.2.2, a swarm population of 30-60 is suitable for lower dimension design spaces. In this case, a k_{max} of 250 and a population of $m = 40$ fireflies are used. The parameters used for β_o^a, β_o^b, and α_o were

found to work for the given design space by some trial and error. The firefly pseudocode used for this problem is shown in Figure 3.9, adapted from the pseudocode presented in [145].

Table 3.3. Firefly algorithm parameter values used.

Parameter	Value
k_{max}	250
m	40
γ	2.5
α_o	0.35
β_o^a	0.1
β_o^b	0.15

	Line
Define: $f_1(X),\ f_2(X),\quad X = [x_1 \dots x_n]^T$ for n sensor design parameters	
Initialize design space and scale parameter values such that $x_j \in [0,1]$ for $j = 1, 2, \dots, n$	2
Generate initial population of m fireflies X_i^{real}, X_i^{grid} for $i = 1, 2, \dots, m$	
Light intensity I_i at X_i is given by $f_1(X_i^{grid})$ and $f_2(X_i^{grid})$	4
Define $\gamma, \alpha_o, \beta_o^a, \beta_o^b$, and k_{max}	
Sort fireflies according to their Pareto dominance ranking	6
while ($k < k_{max}$)	
Calculate ς	
for ii = 1 : m	8
for jj = 1 : m	
Generate values for τ and ϵ_i^t	10
if ($I_{ii} < I_{jj}$) and $\tau \leq \xi$	
Calculate motion of firefly X_{ii}^{real} towards firefly X_{jj}^{real}	12
Vary motion magnitude with β and α	
if (X_{ii}^{grid} is unoccupied)	14
Move firefly X_{ii}^{real}	
end if	16
end if	
Evaluate new $f_1(X_{ii}^{grid}),\ f_2(X_{ii}^{grid})$	18
end for jj	
end for ii	20
Sort fireflies according to their Pareto dominance ranking and record the non-dominated solutions	
end while	22

Figure 3.9. MOFA pseudocode for firefly motion minimization problem, adapted from [145].

For the function evaluation, two main strategies are used to reduce FEA computation time:

1. Employing symmetry/anti-symmetry conditions
2. Using a field-driven mesh definition

Since the sensor is symmetric about both X and Y planes (see Figure 3.10a), it can be halved along each plane with symmetry/anti-symmetry BCs applied at these two interfaces, such that its mesh size is quartered. This reduction in mesh size is very effective in reducing computation times. For the static analysis, symmetry BCs are applied at both plane, and modal analyses apply all unique combinations of symmetry and anti-symmetry BCs (see Figure 3.10a-b). A field-driven mesh is used to also reduce computation times. This works by defining mesh element sizes to be fine near the TPMS surface and rougher within the center of the body (see Figure 3.10c). To validate the mesh accuracy, a mesh resolution study was performed for 100 randomly generated different geometries within the design space, which showed a maximum relative error of 3.15% when decreasing the fine mesh resolution from $0.04a$ to $0.03a$. Thus, a fine mesh resolution of $0.03a$ is used. Quadratic tetrahedral elements were used in the finite element (FE) mesh for all analyses.

For both analyses, the sensor bottom is given a fixed BC. In the modal analysis, the top is left free to allow a conservative estimate of the sensor natural frequencies (in some applications, including testing, the top may be restricted more than this). Thus, the sensor natural frequencies for the optimization will be lower than those calculated according to Section 3.2.1.2. In the static analysis, the sensor top is subjected to a compressive strain of magnitude ε_{pk}, as illustrated in Figure 3.10b. The software nTopology is used for the FEA, because of its ability to use field-driven design, integration with MATLAB, and easy to define workflows.

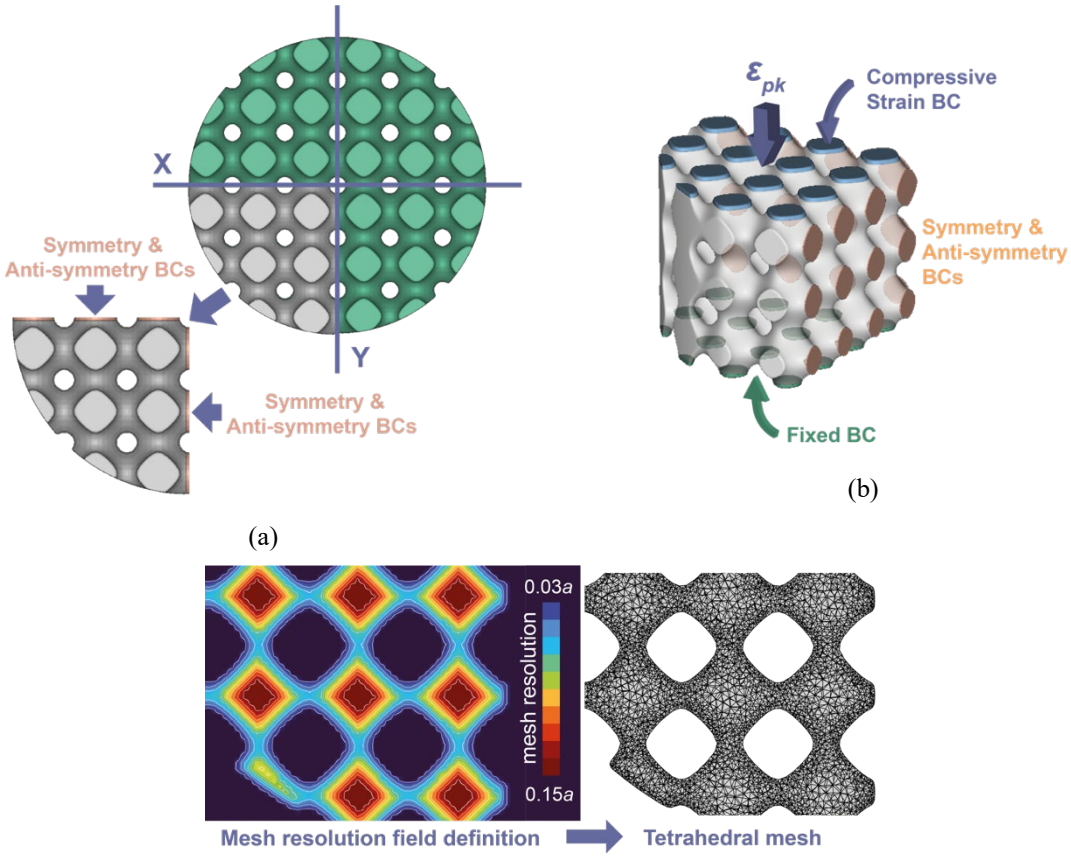

Figure 3.10. (a) Sensor quartering to apply symmetry and anti-symmetry BCs. (b) BCs imposed on sensor geometry during modelling (the strain BC is only applied for the static analysis). (c) A field-defined mesh resolution gradient in the sensor cross-section, showing finer mesh resolution near surfaces, and the tetrahedral mesh resolution created from the field definition.

The coupling of MATLAB and nTopology is illustrated in the algorithm process flow chart in Figure 3.11. The MATLAB code executes the firefly optimization algorithm, and also creates the initial functionally graded TPMS grid. The volume fractions V_f^{bot} and V_f^{top} are varied by blending two TPMS surfaces with each V_f using a sigmoid function, as described in [97], [119]. MATLAB then passes the geometry as an ".stl" file to nTopology for further processing and function evaluation. nTopology performs the radial trim, quarters the sensor to utilize symmetry and anti-symmetry conditions, solves the static and modal analyses, and returns both objective function values to MATLAB. Once the final firefly generation is reached, the MATLAB script ends and saves the results. The algorithm was run on a workstation with 64 GB of physical memory and an Intel i7-

6800K 3.40 GHz processor. Fabrication and characterization of the optimal sensor design is then completed as described in Sections 3.1 and 3.2. We note that to evaluate $\bar{\varepsilon}'$, the principal strains are sampled using a set of 5000 points distributed across the sensor surface (see the bottom-right image in Figure 3.11). These values are then averaged and divided by the input strain (ε_{pk}) to find the value of f_2. The material is assumed to be linear elastic within the main intended strain range ($\varepsilon_{pk} \leq 10\%$).

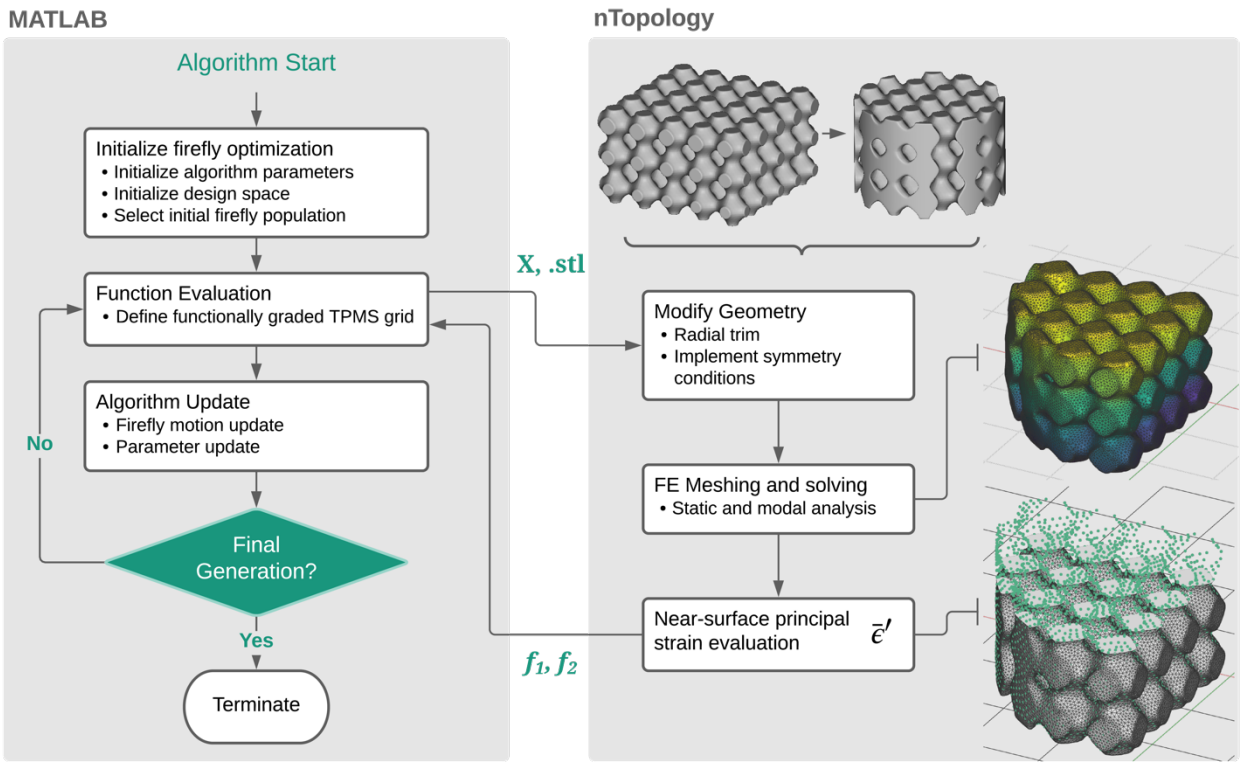

Figure 3.11. MOFA process flow and software coupling between MATLAB and nTopology.

3.2.3 Experimental Methods Summary

In summary, an experimental test method has been developed to test the sensor over a range of strain amplitudes and frequencies. Modeling of the sensor has also been developed to support experimental results. Also, a multi-objective size optimization has been formulated for the sensor design, with the goals of improving its frequency independence and strain sensitivity. The design space of the sensor is constrained by manufacturing and practical limitations, and is discretized to reduce expensive computations. A MOFA code was written and executed in MATLAB for this problem, with FEA evaluations performed in the nTopology software.

Chapter 4
Results and Discussion

4.1 Benchmark Sensor Characterization

To identify trends in sensor behaviour, in total ten benchmark sensors were fabricated and tested. Due to the fixture design and equipment used, vibration frequency and strain amplitude can be controlled independently. The general ranges for test parameters used are ε_{pk} = 1-10 % and ω =10-110 Hz. Initially the ε_{pk} limits were chosen to adequately explore the strain sensor's flexible sensing range. Given this strain range, the increasing frequency will exponentially increase the inertial loads experienced during vibration. To limit inertial loads for the desired strain range, the upper-frequency limit was chosen as 110 Hz. These limits also address some of the potential applications discussed in Section 1.3. Some tests presented in this section also explore outside these general limits.

4.1.1 Benchmark Sensor Modelling

The first four natural frequencies (ω_n) solved from FEA described in Section 3.2.1.2 are listed in Table 4.1. The ideal operating frequency range is below and away from the first natural frequency of 334 Hz, as operating near resonance will also alter the sensor strain state and contribute to a change in piezoresistive behaviour. Thus, it would be hard to correlate resistance changes to strain accurately near a sensor's natural frequency. Since increasing stiffness increases natural frequencies, the balance struck by TPMS geometries between stiffness and compliance is advantageous for flexible vibration strain sensing. This aids in preventing the sensor's natural frequencies from being too low, while still allowing flexibility. To widen the frequency range before resonance, it is beneficial to shift sensor natural frequencies higher by pre-compressing the sensor. To estimate the magnitude of this effect, sensor natural frequencies with and without the pre-compression were compared using FEA (see Table 4.1). A $\varepsilon_o = 5\%$ resulted in a 10% increase in the first natural frequency, and an increase for the first four modes in general. This is expected due to the stiffening of the structure when pre-compression is imposed as a BC.

Table 4.1. First four sensor natural frequencies found using FEA for nominal and pre-compressed strain states.

Mode Number	ω_n (Hz)	
	$\varepsilon_o = 0\%$	$\varepsilon_o = 5\%$
1	334	368
2	355	382
3	373	431
4	383	463

4.1.2 Benchmark Sensor Characterization under Vibration

In this section sensor performance is evaluated for several dynamic strain tests (frequency sweep and dwell tests) to evaluate sensor signal delays, piezoresistive sensitivity, frequency dependence, sensor calibration, minimum strain detection, and durability. All ten sensors' initial major dimensions and nominal electrical resistances are averaged and presented in Table 4.2. The manufacturing parameters for sensor geometry and materials are consistent between sensors. During fabrication silicone thinner can be used to reduce cross-linking, thereby increasing the SR flexibility. However, too high a thinner concentration results in significant shrinking of the sensor during acetone dissolving of the ABS mould [155]. It was found that this could increase the apparent density of the sensor and overall stiffen the sensor, so thinner concentration was kept at 5%. The fabrication procedure produces repeatable dimensions with standard deviations less than 2% of the average value. R_o values exhibit some more variation which did not affect sensor functionality, as discussed later.

Table 4.2. Sensor fabrication parameters, dimensions, and electrical resistance.

Category	Property Name	Value	Std. Deviation
Manufacturing Parameters	SR Thinner Concentration (%)	5	-
	Dip Coats	20	-
Sensor Properties	Height [1] (mm)	9.29	0.07
	Diameter [1] (mm)	16.91	0.31
	R_o [1] (kΩ)	1.62	0.84

[1] Values averaged across 10 sensors.

4.1.2.1 Signal Quality and Delays

To observe signal quality in the time domain, dwell tests were performed on a sensor. Figure 4.1a shows the controlled ε_{pk} and sensor alternating current (AC) voltage signal (ΔV_{out}) at two separate dwells, exciting at frequencies $\omega = 30$ Hz and 80 Hz. Data was collected at 640 samples/s after the sensor behaviour reached a steady-state situation (time = 155 s). For both frequencies the voltage signals display good cyclic repeatability, matching the ε_{pk} waveform in shape and frequency. The ΔV_{out} amplitude also remains consistent between frequencies. Note that the voltage signals are a half-period out-of-phase with the input displacement in Figure 4.1a. This is because a positive trending strain indicates compression of the sensor, which densifies the conductive GNP network and decreases its resistance. Thus, peaks in the ε_{pk} waveform correspond to valleys in the voltage signal. The dominant frequencies in each waveform are confirmed by taking their fast Fourier transform (FFT) and plotting in Figure 4.1b. Both voltage and strain signal sets have matching dominant frequencies, confirming the voltage signal oscillates in time with the input.

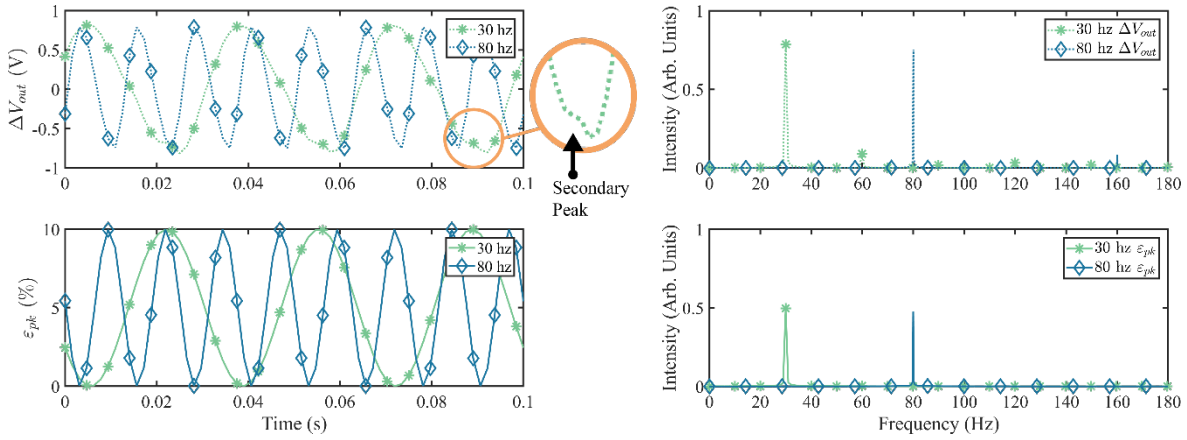

(a) (b)

Figure 4.1. (a) Measured ε_{pk} and sensor voltage signals for 30 and 80 Hz vibration across a time window of 0.1 seconds after reaching steady state (recording started at time = 155 s). A detail view of the secondary voltage peak is also shown in the upper subplot. (b) FFT of voltage and ε_{pk} signals for 30 and 80 Hz vibration.

Notably, the voltage signal has a small, visible secondary peak (shown in the detail view of Figure 4.1a for the 30 Hz dwell). The effect also presents itself in the upper FFT subplot of Figure 4.1b as a multiple of the excitation frequency. For example, the 80 Hz dwell has a signal of smaller intensity at 160 Hz. The cause of this behaviour is suspected to be due to local tensile strains in the sensor, as

discussed in Section 2.1.1. These tensile strains will locally increase resistance due to expansion of the GNP network, which competes with the dominant resistance decrease due to compressive strain. Previously, this secondary peak was also identified during low strain rate compressive loading [15]. To investigate further, CT imaging of the sensor was performed while applying static compressive strains of 0% and 10%. Figure 4.2a shows the sensor mid-section from the 0% strain CT scan using an 80 kV voltage and 20 μm voxel size. Since the sensor is mounted in silver epoxy and attached to PCBs, the sensor top and bottom are slightly obstructed. The 0% strain image can be compared to the 10% strain images shown in Figure 4.2b. Across different cross-sections in the body, voids in the sensor lattice visibly become oblong during compression. Also, thin columnar struts around the sensor perimeter experience local buckling, which is most intense at the sensor surface. This buckling outward results in tensile strains along the sensor surface at these columnar struts. Since the GNP network is a surface coating, the strut buckling effect is likely a significant contributor to localized tensile strains in the network. As a result, these resultant localized tensile strains will contribute to the secondary peak measured in the Figure 4.1a voltage signal.

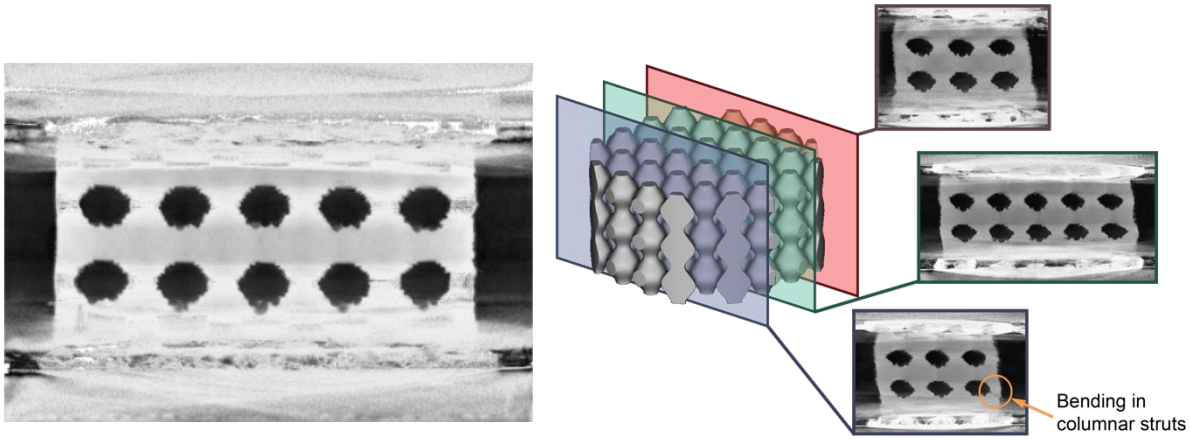

(a) (b)

Figure 4.2. CT scan cross-sections of the sensor under different compressive strains. White/grey pixels indicate the sensor body and black pixels indicate voids/empty space. (a) Cross-section view of the sensor mid-section with 0% strain for reference. (b) Cross-section views of sensor at 10% compressive strain. Each detail view shows the sensor structure at a different location.

Another important quantifier of sensor performance is signal delay. To be used over a range of frequencies, sensor response times must be fast. The time delay between input and output signals was determined for all ten sensors across $\varepsilon_{pk} = \{1, 2, 3, \dots, 10\}$ and $\omega =$ 10-110 Hz. As shown in Figure

4.3 delays were measured up to peak strain rates ($\dot{\varepsilon}_{pk}$) of 34.5 s^{-1}, which are calculated as $\dot{\varepsilon}_{pk} = \varepsilon_{pk}\omega/2$. Since both ε_{pk} and ω are varied in these tests, different combinations can result in the same $\dot{\varepsilon}_{pk}$. To consolidate data from different ε_{pk} and ω, delays for similar $\dot{\varepsilon}_{pk}$ values are first averaged in spans of 15 points to get a single curve per sensor. Then a moving average spanning 15 points is also applied to the curve. Figure 4.3a shows the delay measured in milliseconds (δ_{time}), where the median decreases from 3 ms to less than 1 ms. The delays can also be quantified as a percentage of the excitation period (δ_{period}). Presented in Figure 4.3b, the median δ_{period} stays below a few percent. Delays below the sampling rate resolution of 1.5625×10^{-4} s (line plotted in Figure 4.3a) are measured less-accurately, which is why sometimes delays appear negative. This is particularly apparent when plotting δ_{period} at higher frequencies in Figure 4.3b, since some delays are measured as negative values. For this reason, the resolution-corrected median curve in Figure 4.3a is plotted, and should be referred to for quantitative results. δ_{period} plotted in Figure 4.3b should only be used to infer relative changes in sensor delay with strain rate. These delays are very good, even when not reporting values below the sampling rate resolution. Overall, this data well-illustrates how the viscous effects of SR decrease with increasing strain rate. Due to decreased times for polymer matrix relaxation, there is a clear trend of decreasing delay with increasing strain rate. Overall, the delays measured were all below δ_{period} = 7%. This indicates the sensor can be used for a range of frequencies and strain amplitudes without significant delay. This is an important result that shows piezoresistive sensors can leverage SR flexibility without viscoelastic behaviour compromising performance. This is ideal since SR is a popular matrix material used for flexible piezoresistive sensors due to its common availability and ease of use. Results will also vary depending on the material properties of the SR used as well as the sensor geometry.

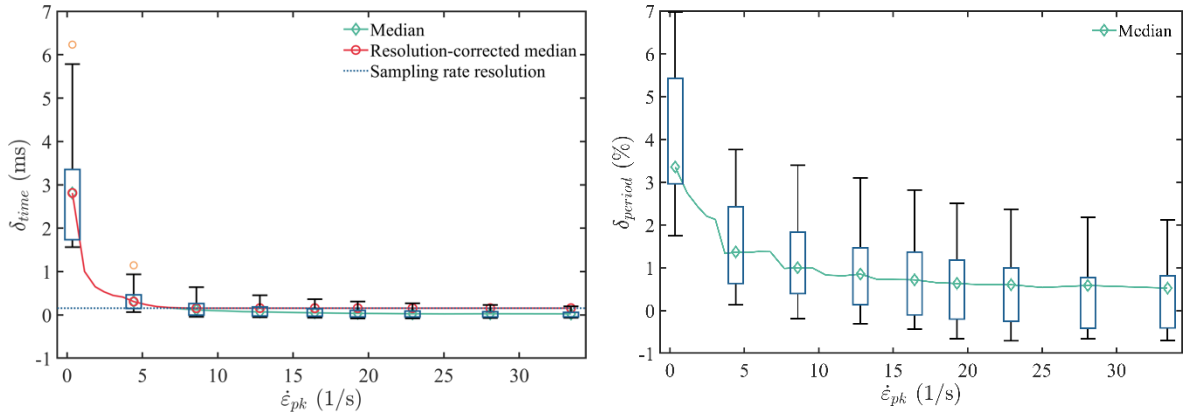

Figure 4.3. Phase delays of sensor signal during vibration using data from 10 sensors. Nine box plots are included at different strain rates to illustrate variation in delays between sensors. (a) Phase delay in the time domain plotted vs peak strain rate during vibration. (b) Phase delay as a percent of the excitation frequency's period, plotted vs peak strain rate during vibration.

As discussed previously, peak strain rates are a product of ε_{pk} and ω. The effect of these two variables on response delay can also be observed independently by plotting each on its own axis. The delay data for all sensors were averaged for unique combinations of ω and ε_{pk} and plotted in Figure 4.4 for δ_{time}. All values of δ_{time} below the sampling rate were round up to 1.5625×10^{-4} s. Frequency effects on delay appear to be much more significant and decay towards zero near 40 Hz for all strain amplitudes. Changes in ε_{pk} generally have a smaller impact compared to frequency. At lower frequencies, it is apparent that δ_{time} reaches a lower asymptote with increasing ε_{pk}. Due to the sampling rate resolution, the effects of both variables at higher frequencies and strain amplitudes cannot be observed. However, both $\varepsilon_{pk}$and ω clearly have unique contributions to signal delay. This is expected, as it is well-documented that viscoelastic materials have properties that are both frequency and amplitude-dependent, including loss and dynamic moduli [107], [108]. For estimating delays given an application, the minimum operating frequency and strain amplitude should be determined and used with Figure 4.4 to predict an average sensor signal delay.

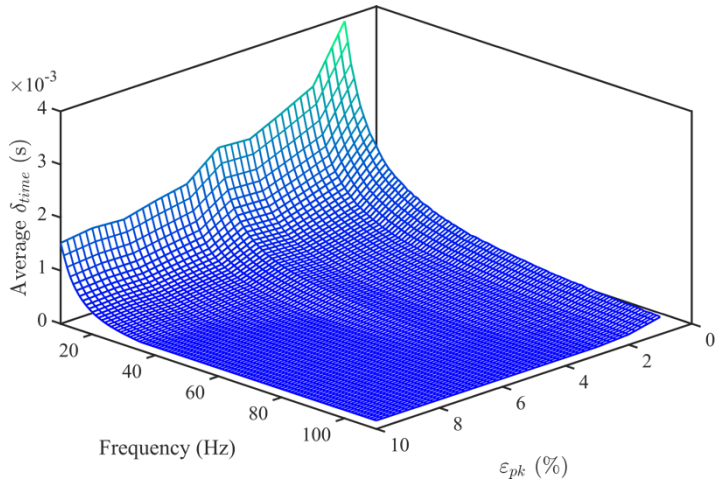

Figure 4.4. Surface plot of average sensor time delay versus frequency and peak-to-peak strain amplitude. The data is remapped here to have a similar resolution on each axis, but was originally collected at resolutions of 0.05 Hz and 1% for ω and ε_{pk}, respectively.

4.1.2.2 Performance and Calibration

Same as the data used for delays, $\Delta R/R_o$ of each sensor was measured using frequency sweeps done at a constant $\varepsilon_{pk} = \{1,2,3, \ldots,10\}$ for the range $\omega =$ 10-110 Hz. After applying a moving average with a window of 15 data points, $\Delta R/R_o$ is plotted in Figure 4.5a for a single sensor. Each curve corresponds to a fixed ε_{pk}. The curves are mostly flat, indicating strong frequency independence for the sensor. Across all sensors and test parameters, the mean error due to $\Delta R/R_o$ changing with frequency is only $\pm$3.89%. This low error is expected, as the FEA in Section 4.1.1 predicted the sensor's first natural frequency to be well beyond this test range ($\omega_{n,1} = 334$ Hz). The increased natural frequencies due to sensor pre-compression also aids frequency independence here. This plot also confirms that any shifts in strain sensitivity due to strain-rate dependence are not significant for this test range. While the previous testing performed under lower loading rates ($\leq$60 mm/min in [15]) showed sensitivity dependency on loading rate, this effect clearly diminishes with increased rates. In comparison, the minimum peak loading rate used here is ~175 mm/min (for $\varepsilon_{pk} =$ 1% and $\omega = 10$ Hz). This reinforces the evidence that the sensor's viscous effects decrease with increasing frequency.

The sweeps performed for all ten sensors resulted in peak forces up to ~180 N for $\varepsilon_{pk} = 10\%$ at $\omega = 110$ Hz, which is close to the shaker force limitations. Figure 4.5a shows these results for an

example sensor. To further investigate frequency independence, one sensor was tested at $\varepsilon_{pk} = 3\%$ up to 200 Hz (see Figure 4.5b). In this range the sensor still exhibited a similar, low-frequency dependence error of only $\pm 2.73\%$. Some small shifts in $\Delta R/R_o$ can even be attributed to small lateral motion of the shaker armature flexure. The lateral motion of the armature was confirmed by impact hammer testing of the shaker, which showed natural frequencies near 95 Hz and 165 Hz (see Appendix Figure B-1). In some cases, these frequencies corresponded to small shifts in $\Delta R/R_o$, such as the visible shift near 165-170 Hz in Figure 4.5b. Shaker resonance can then contribute to sensor errors, suggesting they are even being slightly underreported here. Overall, even beyond the primary test range of 110 Hz, the sensor continues to show good frequency independence.

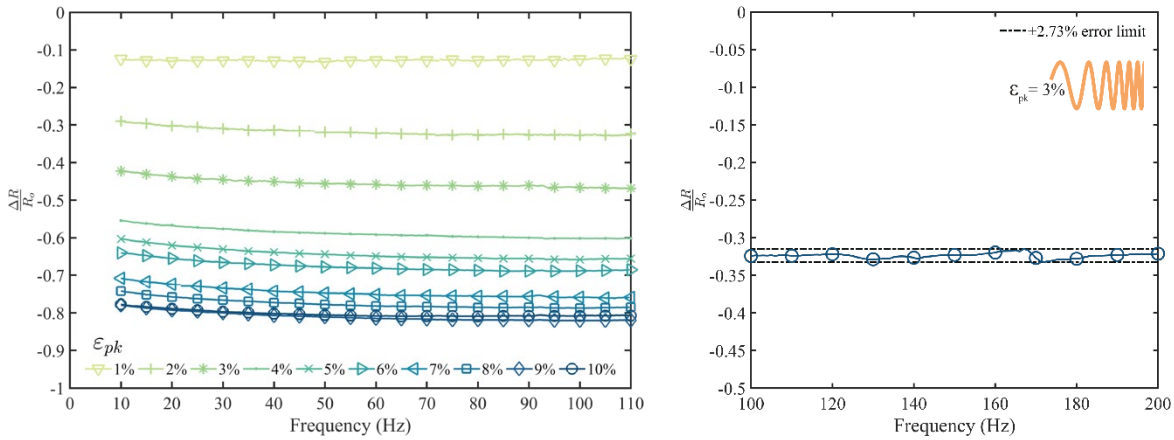

(a) (b)

Figure 4.5. (a) Sensor $\Delta R/R_o$ across a 10-110 Hz frequency range for ε_{pk}= 1-10% (b) $\Delta R/R_o$ plotted vs frequency for a single sensor test at $\varepsilon_{pk} = 3\%$ from 100-200 Hz.

To determine trends in sensor piezoresistive behaviour with ε_{pk}, $\Delta R/R_o$ values were averaged for each sensor across the 10-110 Hz frequency range, and then plotted together against ε_{pk} in Figure 4.6a. There is a visibly consistent non-linear trend between ε_{pk} and $\Delta R/R_o$ for all sensors. Here the absolute resistance change (ΔR) decreases with increasing ε_{pk}, approaching an asymptote at higher amplitudes. This occurs for two reasons: First, non-linear piezoresistivity has frequently been shown experimentally for conductive nanoparticle networks in CPCs, especially at higher strains [33], [54]. This agrees well with some nanoparticle network models, especially those that are based on tunneling resistances. Second, as the sensor's electrical resistance decreases with increasing compressive strain, it hits a lower limit before reaching zero. As a result, this sensor has a maximum theoretical value of

$\Delta R/R_o = -1$ when testing in compression, which acts as an asymptote. The top right of Figure 4.6a also shows the nominal resistance distribution of the sensors, which can vary from 0.6-3.4 kΩ. Within this range, no trend was observed between nominal resistance and sensor performance. This indicates that R_o does not require strict tolerances to guarantee good performance, and dip coating the mould 20 times consistently provides an adequate GNP coating for sensing.

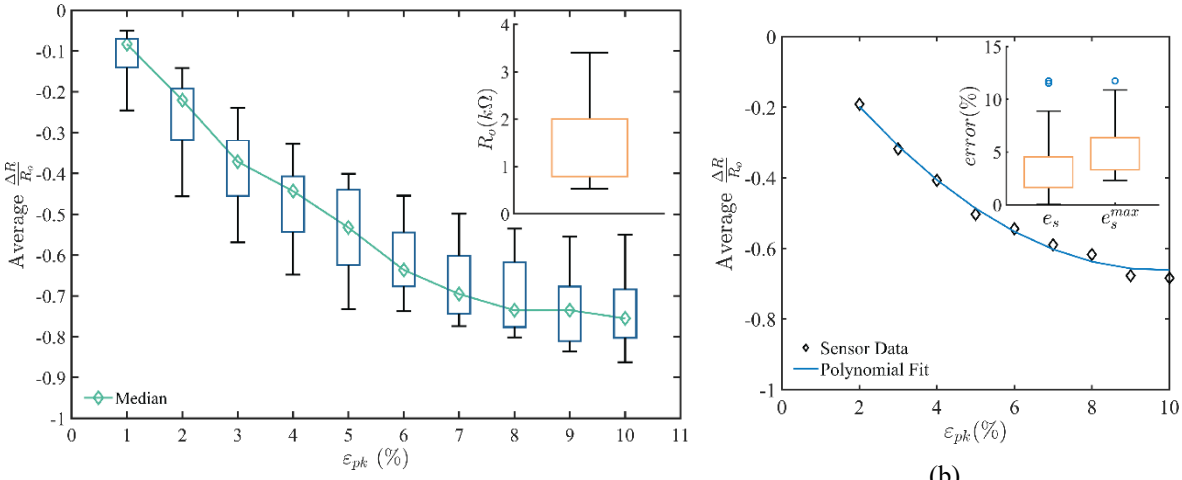

(a) (b)

Figure 4.6. (a) Average ΔR/Ro across ε_{pk} = 1-10% for ten sensors. The distribution of sensor nominal resistance is shown in box plot in the top right corner. (b) Polynomial fit to a single sensor's $\Delta R/R_o$ data. Boxplots in the top right are made using the errors for all sensors and strains (e_s), and the max error for each sensor (e_s^{max}).

Since the overall relationship between ε_{pk} and $\Delta R/R_o$ is consistent across sensors, it is possible to individually calibrate them for practical use. Due to the non-linear relationship observed, an error-conscious calibration should be non-linear (higher-order polynomial) as well. Table 4.3 compares fit quality to sensor data in terms of error for several different options. For comparison, linear and second-degree polynomial fits were applied to each set of sensor data. Also, different strain operating ranges (1-10%, 2-10%, and 3-10%) were explored to observe the effect on fit quality. Table 4.3 summarizes the resulting median values of sensor errors for different strain ranges and fits, where e_s is a general sensor error for any given strain amplitude and sensor. When selecting polynomial coefficients to fit a curve to data, they are optimized in MATLAB by minimizing the maximum sensor error (e_s^{max}). Polynomial fits clearly model the sensor behaviour more-accurately, reducing e_s^{max} by 12-52% compared to linear fits. While linear calibrations are common for metallic

piezoresistive sensors, a non-linear calibration is justified given the fit quality improvements observed. When comparing differing ε_{pk} ranges, errors are amplified at low strain amplitudes, which is why several options excluding lower strains are considered. While an "acceptable" error may depend on the application, in general the reduction in error by excluding ε_{pk} = 1% is considered to be worthwhile (e_s^{max} = 3.56%). Thus, from the ε_{pk} range tested an operating range of 2-10% is recommended for general applications. An example of the calibration fit is shown for one sensor in Figure 4.6b. Box plots in the upper right corner also show the distribution of errors for all sensors, which has only a few outliers. Since no physical damage was discovered on these sensors, it is assumed any error variation is primarily due to differences introduced in fabrication.

Table 4.3. Fit errors for different combinations of fit methods and strain operating ranges.

ε_{pk} Range (%)	Fit Method	Mean e_s (%)	Mean e_s^{max} (%)
1-10	Polynomial	4.00	12.11
	Linear	13.55	25.04
2-10	Polynomial	3.56	11.73
	Linear	9.05	16.61
3-10	Polynomial	3.29	11.37
	Linear	5.85	13.03

4.1.2.3 Minimum Strain Sensitivity

Minimum sensor sensitivity for compressive vibrations was also determined by lowering the strain amplitude until noise became dominant in the signal. This study is done to determine the lower limit of the strain sensitivity, ignoring error contributions discussed in the previous subsection. Figure 4.7 shows two plots where a sensor was tested at $\varepsilon_{pk} = 0.50\%$ and 0.25% (Figure 4.7a and b, respectively) during a 40 Hz dwell. The transition from Figure 4.7a to b clearly shows that with decreasing strain the secondary peak amplitude begins to dominate the signal. At the lower $\varepsilon_{pk} = 0.25\%$, the secondary peak becomes so significant that the voltage waveform appears to oscillate at twice the input displacement frequency. Thus, care should be taken to avoid testing use the sensor in an operating range $\varepsilon_{pk} < 0.25\%$. Contribution from the secondary peak will increase with decreasing strain amplitude such that the sensor is best used for $\varepsilon_{pk} \geq 1\%$. This range is fine for a flexible sensor and does not limit the 2-10% operating range previously recommended for sensor calibration. 0.50%

and 0.25% strain amplitudes amount to very small travel amplitudes of ~23 µm and ~12 µm, respectively.

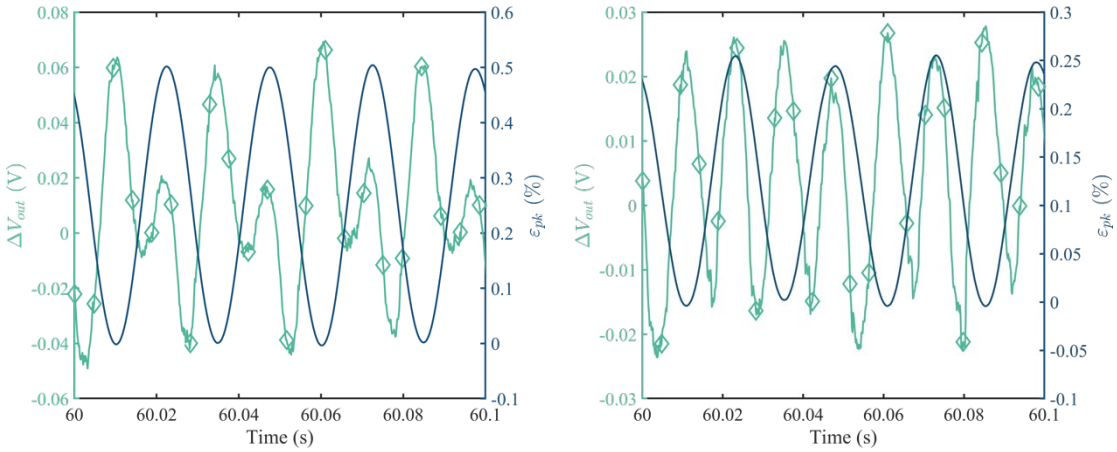

(a) (b)

Figure 4.7. (a) AC voltage and ε_{pk} signals for $\varepsilon_{pk} = 0.50\%$ at a 40 Hz sine dwell. (b) AC voltage and ε_{pk} signal for $\varepsilon_{pk} = 0.25\%$ at a 40 Hz sine dwell.

4.1.3 Benchmark Sensor Durability and Performance Summary

During characterization, each sensor was put through rigorous cyclic testing over a range of frequencies and strains. For each sensor, on average over 15 million cycles and 80 hours of testing were performed. Sustained testing periods of 20 hours were repeated several times for each sensor to observe if damage occurred after long periods of testing. Throughout and after these tests, no sensor exhibited any visible structural damage. Moreover, the sensor sensitivity was observed to stabilize with continued testing after a conditioning period, which is common for nanoparticle-based flexible sensors. To illustrate this, a sensor was tested each day for 30 minutes at $\varepsilon_{pk} = 5\%$ and its sensitivity was recorded. Figure 4.8 shows the sensitivity change each day measured relative to day 1, which stabilizes after day 8. This further proves the robust behaviour of these sensors, attributed to their SEG construction. The reason the sensor requires conditioning is due to initial damage of the polymer matrix when undergoing strain [62], which stabilizes as the number of cycles increases. As discussed in Section 2.1.4, this observed behaviour is due to Mullins and Payne effects, and should become negligible after ~100 cycles or less. The dominant cause for long sensitivity stabilization times is suspected to be due to polymer chain relaxation after pre-compression is applied. The time to

stabilize/condition the sensor can be accelerated with more frequent cyclic testing, where a minimum 3-4 days was typically required before the sensitivity stabilized.

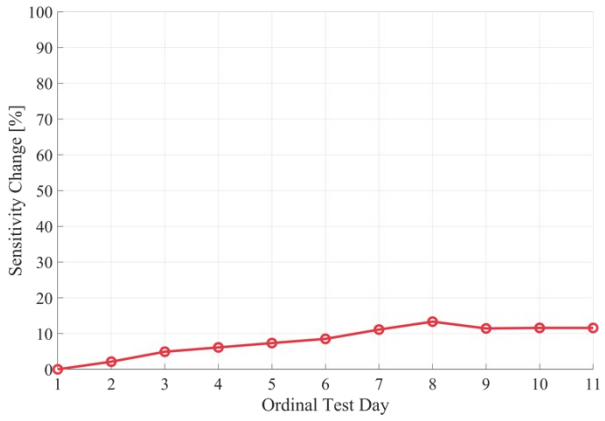

Figure 4.8. Sensor sensitivity change across multiple days of testing.

Table 4.4 shows a summary of important sensor performance indicators. As discussed, maximum sensor error is best minimized when using a polynomial calibration. The mean GF between all sensors is -10.2, which is a strain sensitivity approximately five times greater than a metallic-based strain gauge. This is consistent with the GF found during quasistatic tests previously performed on the sensor [15], and indicates sensitivity does not dramatically change with the higher strain rates used here.

Table 4.4. Sensor performance summary for the 10-110 Hz and ε_{pk} = 1-10% sensing range.

Sensor Property	**Mean**	**Std. Deviation**
Gauge Factor	-10.2	3.30
Strain error, e_s(±%)	3.56 [1]	2.75 [1]
Frequency error, e_f (±%)	3.89	3.46
Time Delay, δ_{time} (ms)	0.420 [2]	0.676 [2]

[1] Values given for recommended ε_{pk} = 2-10% range

[2] Values given for the resolution-corrected data set (see Figure 4.3a).

4.2 Sensor Size Optimization

The converged firefly locations at their final generation are shown in Figure 4.9a for the objective space, including the dominated solutions and Pareto front. Each point represents a unique sensor design. The dominated solutions can be seen to gather near a few local optima in the objective space, as they are very close to the Pareto front. The benchmark sensor's objective function values are also

shown for reference, where clearly there is an improvement in both objective function values for many of the optimal solutions found. An optimal solution is chosen from the Pareto front that compromises between the two objective functions, corresponding to the sensor design parameters in Table 4.5. This optimal sensor's small cell size (a = 3.3 mm) is similar to the benchmark sensor. However, the unit cells patterned along the height and base of the sensor are reduced to 2 and 4, respectively. The highest allowed volume fraction of 0.66 is used for both the bottom and top of the sensor, so there is no functional grading along the sensor height. The fabricated optimal sensor and its mould are also shown in Figure 4.9a.

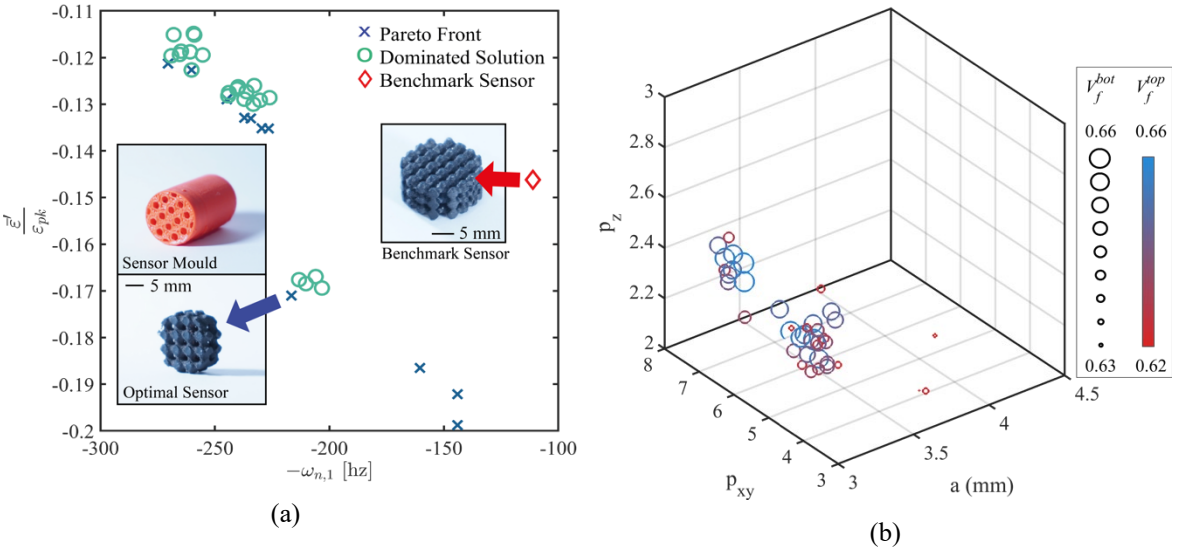

(a) (b)

Figure 4.9. (a) Final 40 firefly locations in the objective space after convergence at 250 generations. (b) Final 40 firefly locations in the design space. Since the design space is a hyperspace of 5 dimensions, colour and point size are additionally used to represent the volume fraction values (see the legend on the right).

Table 4.5. Benchmark and optimal sensor design parameter values.

Design Parameter or Objective Function	**Benchmark Sensor**	**Optimal Sensor**
a (mm)	3.33	3.3
p_{xy}	6	4
p_z	3	2
V_f^{bot}	0.42	0.66
V_f^{top}	0.42	0.66
f_1 (Hz)	111	217
f_2	-0.146	-0.171

The final firefly sensor design parameters are also shown in Figure 4.9b. By comparing the solutions, especially those on the Pareto front, some inferences can be made on what design parameter values are preferred. For example, the designs with high natural frequencies are either short, wide, or both. Since the sensor has fixed-free BCs, the first natural frequency is typically a bending mode shape, as shown in Figure 4.10a. Short and wide sensors reduce this bending effect, such that they are preferred to maximize the first sensor resonance.

In addition, volume fraction gradings along the sensor height were not found to be desirable for improving either objective, with high volume fractions consistently preferred. Considering f_1, a higher sensor density will stiffen the structure, so the sensor's natural frequencies will increase for higher volume fractions. Considering f_2, high volume fractions were also preferred, indicating that small volume fractions lead to greater tensile strain contribution in the TPMS structure. This reason can be partially explained by examining the distribution of tensile and compressive principal strains on the optimal and benchmark sensors, as shown in Figure 4.10b and c, respectively. Each figure shows an isometric view of the quartered sensor design at the top, where some of the sampled strains are visible for both tensile and compressive strains. The sensor side view at the bottom of the figures is transparent, such that all the sampled principal strains are visible. For either sensor design, compressive strains are dominant along the sensor perimeter (labeled in Figure 4.10b). For this reason, designs with larger surface areas at the perimeter are preferred to produce a larger compressive strain contribution. This area increases with volume fraction, which is why higher volume fractions are preferred for f_2. Also, the contribution from compressive perimeter strain will increase for smaller diameter sensors. This is because the sensor cross-section area decreases at an exponential rate with diameter, while sensor perimeter decreases linearly. So by decreasing the diameter, the perimeter strain will contribute to a larger fraction of the overall sensor strain. This partially explains why the optimal sensor has a smaller p_{xy}. Overall, it is not advantageous to functionally grade the sensor's volume fraction along its height, since both objective functions are found to prefer consistently higher volume fraction.

Larger unit cells were also not preferred, due to their poorer packing density. As explained earlier, increasing the sensor density will increase its natural frequencies, so for a given sensor height and diameter, smaller unit cells can generally achieve a higher packing density within the volume. Since altering the unit cell size will uniformly scale the sensor, it should not change the distribution of principal surface strains.

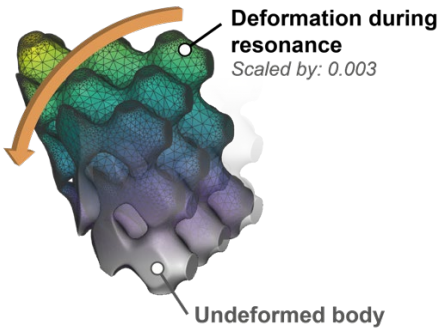

(a)

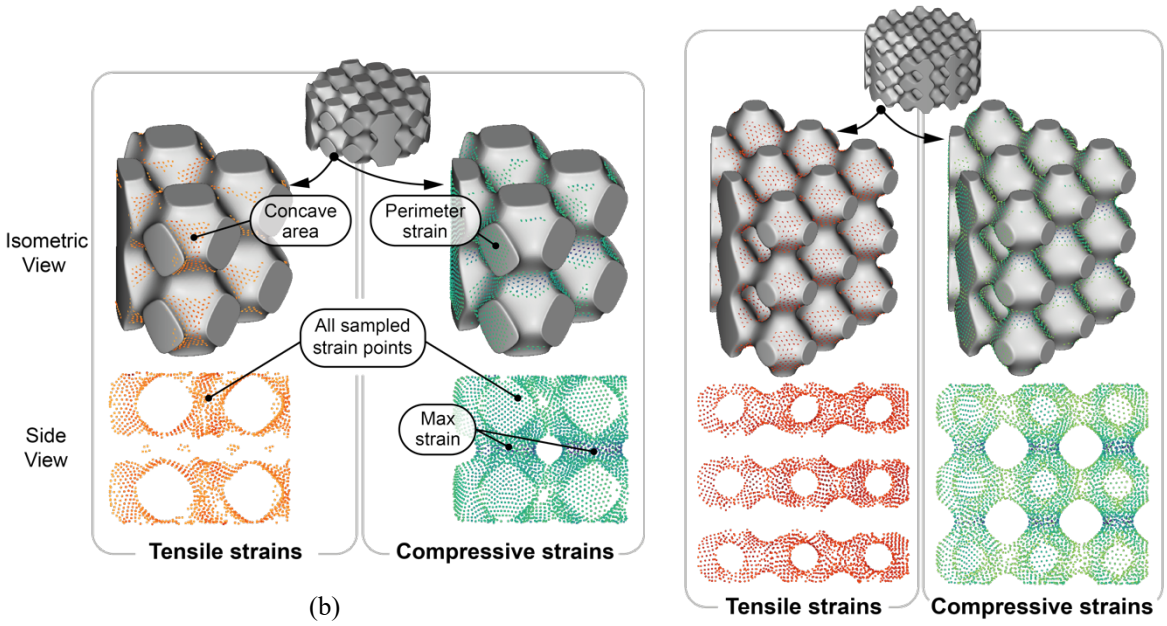

(b)

(c)

Figure 4.10. (a) Benchmark sensor bending deformation shown during its first natural frequency. Sensor average tensile and compressive principal surface strain point maps for a quarter of the: (a) optimal sensor, and (b) benchmark sensor.

Maximum compressive strain occurs at the small cross-sectional areas of the sensor (labeled in Figure 4.10b) since the small area causes a stress concentration. By comparison, the concave patches of the sensor surface (labeled in Figure 4.10b) are generally where tensile strains dominate. Due to the curvature of these patches, the strain magnitude and area may vary with volume fraction. For this reason, it is difficult to correlate any change in these tensile patches to a net positive or negative effect on f_2. To provide a more direct comparison, the principal surface strain distributions for the benchmark and optimal sensors are plotted in the histogram in Figure 4.11. Notably, the benchmark

sensor has a significant contribution from several bins at small magnitude tensile strains. The distribution of strain in the optimal sensor is more balanced, without any distinct peaks, and has a wider left tail of compressive strains. The combination of these effects improves f_2.

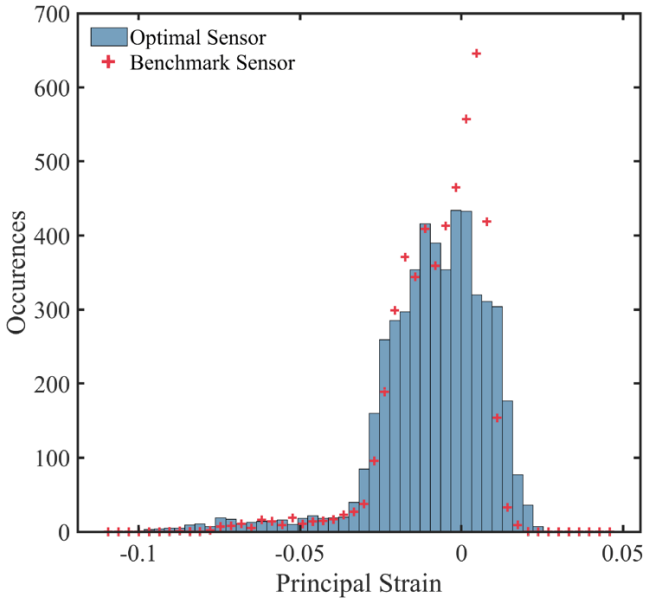

Figure 4.11. Surface principal strain distribution for optimal and benchmark sensors.

To confirm good exploration of the design space, the locations of all points explored during the algorithm were recorded. For each sensor design parameter, their entire range of acceptable values should be explored in good proportion to the design space. The number of occurrences that parameter values are visited is shown in Figure 4.12a, with a separate histogram for each parameter. This is also compared to the distribution of all values within the design space. These distributions are normalized to allow a more direct comparison between the two. In general, sensor parameter values are visited proportionately to their number of occurrences in the design space. The main exceptions to this are volume fraction, where larger values were visited more frequently, and unit cell size, where smaller values were visited more frequently. This is due to the exploitation component of the algorithm, which is more biased towards certain sensor parameter values if they benefit the objectives more. As explained in the previous paragraph, both high volume fractions and low unit cell sizes were favoured, causing them to be visited in greater proportion. Overall, the good exploration helps confirm that the algorithm converged on the most optimal solutions. The function evaluation times for a single algorithm run are also shown in Figure 4.12b, with an average time of 2.05 minutes. Larger

function evaluations are generally due to large values of p_{xy} and p_z, which occur less frequently in the design space as indicated in Figure 4.12a. The NFE required for the solution was 1618, only 14.5% of the total solutions in the design space, which indicates the good efficiency of the algorithm. The average motion magnitude during each generation is shown in Figure 4.12c, illustrating how the fireflies converge with each generation. The significant decreased from generations 100-200 is due to the point of inflection at generation k =150 in the random motion sigmoid from Equation (3.11). The random motion magnitude parameter (α) is overlayed to show this relationship. Thus, the influence of the firefly random motion is shown to encourage greater design space exploration and prevent premature convergence.

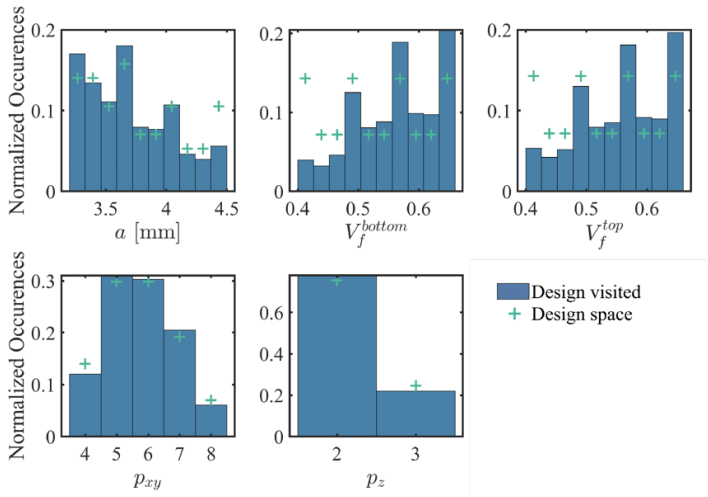

(a)

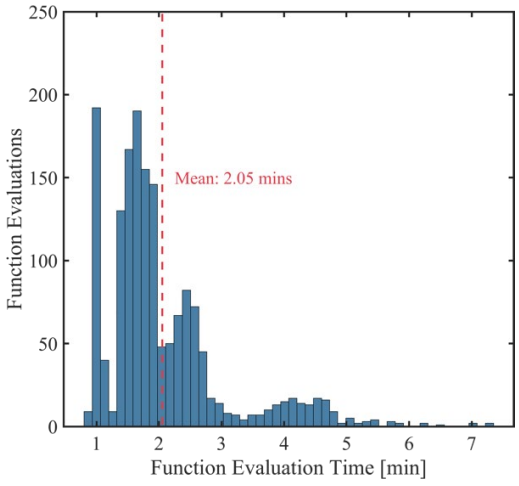

(b)

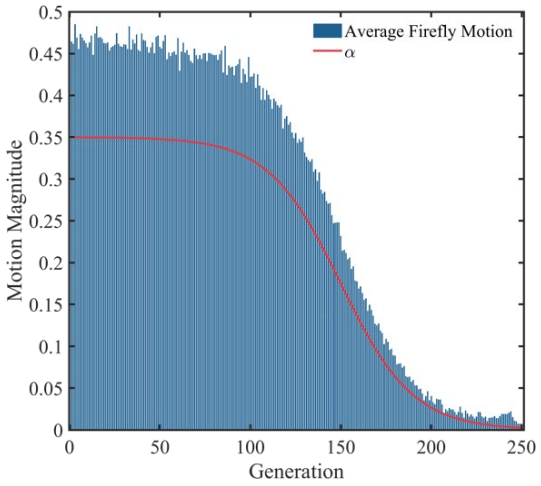

(c)

Figure 4.12. (a) Distribution of parameter values explored compared to design space size for a single MOFA run. (b) Distribution of FEA function evaluation times for a single MOFA run. (c) Average firefly motion magnitude each generation during the MOFA and magnitude of firefly random motion parameter α.

4.2.1 Optimal Sensor Characterization

When fabricating the new optimal sensor, the manufacturing process and parameters are repeated as shown in Table 4.6. The optimal sensor dimensions and nominal resistance are also shown in this table. Compared to the benchmark sensor, the nominal resistance is much lower. This can be due to the reduction in surface area from 2366 mm^2 to 905 mm^2 for the optimal design, as there will be fewer resistance junctions between nanoparticles. After oversizing the mould by 10%, the optimal

sensor was still slightly undersized by 3.7-6.0% in its major dimensions after shrinking during the acetone dissolving phase.

Table 4.6. Optimal sensor manufacturing parameters and general properties.

Category	Property Name	Value
Manufacturing Parameter	SR Thinner Concentration (%)	5
	Dip Coats	20
Sensor Properties	Height (mm)	6.20
	Diameter (mm)	12.71
	R_o (Ω)	130

To characterize the optimal sensor for vibration strain sensing, the general frequency sweep tests for $\varepsilon_{pk} = \{1,2,3, \dots ,10\}$ and $\omega =$ 10-110 Hz are repeated. Because the optimal sensor's nominal resistance is much lower compared to the benchmark sensor, small resistance changes on the order of a few ohms will occur for the smallest strains applied. To measure these changes more accurately, the sensor resistance is measured in a Wheatstone bridge configuration for $\varepsilon_{pk} =$ 1-2% (see Appendix Figure C-1). The frequency sweep results are shown in the FRFs plotted in Figure 4.13a. Overall the sensor exhibited very strong frequency independence, with a mean frequency error of only $\pm$2.18%. There is also no fluctuation in sensitivity due to shaker resonance near $\omega =$ 95 Hz. This is explained by the greater stiffness of this high volume fraction sensor design, which makes it less susceptible to any small lateral forces. It is also noted that there is a small amplitude-dependent behaviour for the optimal sensor. This becomes apparent at higher strain amplitudes, where the sensitivity slightly changes between 10-30 Hz; however, the effect on frequency dependence error is minimal. Overall, the mean frequency error for the optimal sensor of $\pm$2.18% is a significant improvement compared to the benchmark sensor ($\pm$3.89%).

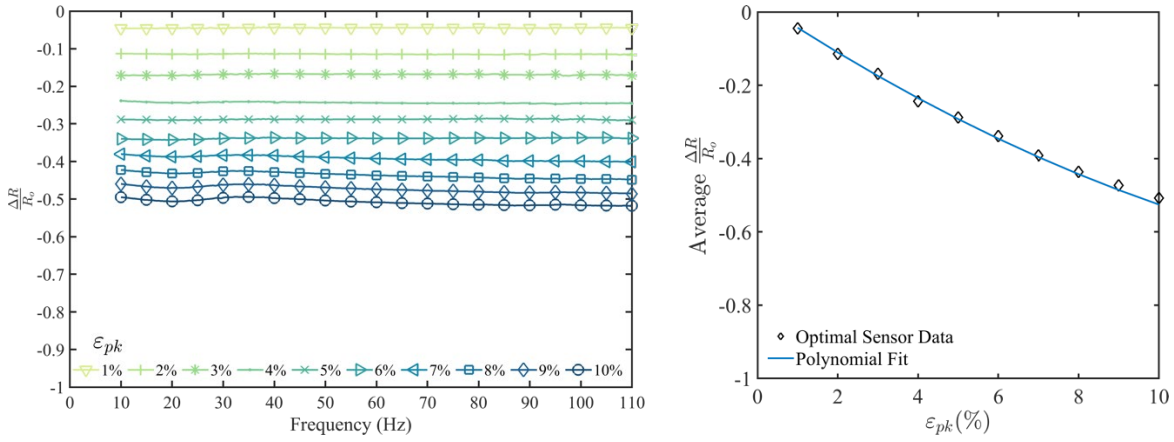

(a) (b)

Figure 4.13. (a) Optimal sensor $\Delta R/R_o$ across a 10-110 Hz frequency range for ε_{pk}= 1-10 %. (b) Average $\Delta R/R_o$ across ε_{pk} = 1-10% for the optimal sensor, with a polynomial fit applied to the data set.

The optimal sensor relationship between strain amplitude and resistance change is also shown in Figure 4.13b. The superscript of "O" is used to indicate error values between the optimal sensor data and curve fit (e_s^O and $e_s^{max,O}$). Again, calibration of the sensor is described by a range of polynomial and linear fits to the sensor data, shown in Table 4.7. The 2nd order polynomial fit still best describes the sensor, and in this case a mean error of 2.61% can be achieved for the full 1-10% strain amplitude range. The reduction in error for the 2-10% range is not considered worthwhile, so in this case the full strain amplitude range tested can be used. The relative change in error compared to the benchmark sensor, Δe_s, is also presented in Table 4.7. A good improvement is seen in error reduction for both the polynomial and linear fits, with reductions to the mean sensor error of 28.1-58.4%. This is explained by the increased stiffness of the high volume fraction sensor design, which provides more stable resistance changes. As well, it is noted that the sensor strain sensitivity has decreased for the optimal sensor, with an average GF of -5.50 compared to -10.2 for the benchmark design.

Table 4.7. Optimal sensor calibration errors for different combinations of fit methods and strain operating ranges. Relative error improvements compared to the benchmark sensor are also shown.

ε_{pk} Range (%)	Fit Method	Mean e_s^O (%)	$e_s^{max,O}$ (%)	Δe_s (%)
1-10	Polynomial	2.61	3.53	+34.8
	Linear	5.64	10.10	+58.4
2-10	Polynomial	2.56	3.51	+28.1
	Linear	3.78	6.79	+58.2
3-10	Polynomial	1.97	2.65	+40.1
	Linear	3.35	5.78	+42.7

The reason for the GF decrease is hypothesized to be due to the objective function f_2 requiring revision. Originally, it was assumed that by minimizing the average principal strain in the sensor (assuming compressive strain is negative), a geometry with a very dominant compressive strain will be found. Since the sensor resistance is dependent on the strain experienced by the nanoparticle network, an increased compressive strain should result in an increased resistance change. However, if there is a group of high tensile strain regions within these nanoparticle pathways, there will be a high localized resistance increase. If this resistance increase is significantly large, it will begin to dominate and limit the resistance change regardless of the resistance decrease elsewhere. Reviewing the optimal sensor strain distribution in Figure 4.11, compared to the old sensor it has a slightly wider right tail. Thus, these large tensile strains could be causing a negative effect on the sensor GF. The optimization should then be revised in the future to prevent this behaviour. For example, a third objective function could be included to minimize the maximum tensile strain on the sensor surface. As well, it could be valuable to change which strains are sampled on the sensor surface depending on their orientation. Assuming the conductive pathways are primarily parallel to the TPMS surface, local reductions in electrical resistance should be due to compressive strains parallel to the local surface. Instead of considering the principal surface strain, strains which are near-perpendicular to the local surface normal could only be considered. These revisions to f_2 may more-accurately predict changes in GF, though they will require experimental validation first.

The change to a lower GF does provides some advantage, because it will widen the sensor's operating strain range. As discussed previously, this piezoresistive sensor has a minimum resistance which it will approach with increasing strain. The GF directly controls the rate at which this limit is approached with respect to strain. Therefore, a smaller GF will widen the strain operating range before this limit is reached. Also, the smaller diameter of the optimal sensor provides some additional

benefit, as a smaller sensor design can provide better spatial resolution for applications where multiple sensors are used in an array. The main optimal sensor properties discussed are summarized in Table 4.8.

Table 4.8. Optimal sensor performance summary for the 10-110 Hz and ε_{pk} = 1-10% sensing range.

Optimal Sensor Property	Mean
GF	-5.50
e_s^O (±%)	2.61
e_f (±%)	2.18

4.3 Results Summary

In summary, the benchmark sensors were fabricated and characterized across ε_{pk} = 1-10% and ω = 10-110 Hz, demonstrating good frequency independence. Median sensor delays below 3 ms also indicate its suitability for vibration strain sensing at higher frequencies, due to low viscous damping. Sensors are shown to be best calibrated with a second degree polynomial fit, and the average sensor GF is -10.2.

Also, an optimal sensor design was found using the MOFA and subsequently fabricated. The algorithm produced a good Pareto front of diverse designs and reduced the maximum NFE by 85.5%. Testing of the sensor showed an improvement in sensor frequency independence and better agreement when modeling its piezoresistive resistance change.

Chapter 5
Conclusions

Overall, this manuscript presents the testing of a TPMS flexible piezoresistive sensor for vibration strain sensing. Sensors were fabricated using AM methods combining SR with an electrically conductive surface coating of GNP as defined in [15]. A benchmark sensor design was tested while independently controlling strain amplitude and frequency, for the ranges of ε_{pk} = 1-10% and ω = 10-110 Hz. The main conclusions about the benchmark sensor performance are:

- Median δ_{time} below 3 ms, showing that the SR matrix viscoelasticity does not inhibit high-frequency testing.
- Strong frequency independence was demonstrated with a mean e_f = $\pm$3.89%.
- 2nd degree polynomial fits were shown to represent the relationship between ε_{pk} and $\Delta R/R_o$ much better than linear fits. This resulted in mean error of e_s = $\pm$3.56% for the recommended operating range of ε_{pk} = 2-10%.
- The rigorous testing of each sensor, for over 15 million cycles and 80 hours each, highlights its durability and robust construction.

These results highlight the advantages and practicality of the TPMS flexible sensor used for vibration strain sensing. The second component of this manuscript presents a size optimization of the TPMS sensor design using a MOFA. The sensor's first natural frequency was maximized while minimizing the average principal strain near the sensor surface. Several manufacturing constraints of the fabrication process were considered in the optimization to ensure a feasible design. The optimal design was also fabricated and characterized for the same ranges of ε_{pk} = 1-10% and ω = 10-110 Hz. This is the first design optimization of a flexible piezoresistive sensor in literature. The optimization resulted in:

- Convergence within 1618 function evaluations, a reduction of 85.5% compared to the design space size.
- An improved sensor design with mean frequency error e_f = $\pm$2.18%.
- An improved e_s^O = $\pm$2.61% for the range of ε_{pk} = 1-10%.

5.1 Future Work

Vibration strain sensing for flexible piezoresistive sensors is still an underdeveloped category in literature, so there is significant incentive to continue pursuing this topic. Due to the overall complexity of the CPCs studied, there are many avenues for continued work on this sensor.

Revisions to the objective function for maximizing compressive strain in the sensor's nanoparticle network should be made, such that GF is maximized as a result. Also, the design space size was limited to only 5 sensor design parameters, but more parameters could be added to yield further improvements. For example, different TPMS types can be used and combined, functional gradings may be defined differently (e.g. a radial grading can be used), TPMS unit cells can be stretched/elongated in certain directions, etc. More complex models can also be implemented to improve the correlation between objective functions and experimental results. For instance, more complex conductive nanoparticle network models may be introduced to predict the sensor GF. However, this may sacrifice generality of objective function(s) and would require detailed knowledge and control of the fabrication process and materials. Related to the process, future optimizations can also focus on optimizing process parameters as well, including the number of dip coats, the sensor time spent in acetone, the mould's print layer height, and the silicone thinner percentage.

Some exploration of different process aspects may provide additional performance benefit. For example, different matrix materials may also be worthwhile investigating to look for further improvements for dynamic strain sensing. Also, the surface roughness of the sensor due to FDM could be reduced by changing the AM process used. Vat photopolymerization could be trialed as an alternative to FDM, as it can offer better surface finishes.

References

[1] G. F. Chalmers *et al*, *Strain Gauge Technology.* (2nd ed.) London: Elsevier Applied Science, 1992.

[2] T. Q. Trung and N. Lee, "Flexible and stretchable physical sensor integrated platforms for wearable human-activity monitoring and personal healthcare," *Adv Mater,* vol. 28, *(22),* pp. 4338-4372, 2016. DOI: 10.1002/adma.201504244.

[3] X. Li *et al*, "Highly sensitive, reliable and flexible piezoresistive pressure sensors featuring polyurethane sponge coated with MXene sheets," *J. Colloid Interface Sci.,* vol. 542, pp. 54-62, 2019. DOI: 10.1016/j.jcis.2019.01.123.

[4] S. He *et al*, "Recent progress in 3D printed mold-based sensors," *Sensors,* vol. 20, *(3),* pp. 703, 2020. DOI: 10.3390/s20030703.

[5] R. Hague, S. Mansour and N. Saleh, "Design opportunities with rapid manufacturing," *Assembly Automation*
, vol. 23, *(4),* pp. 346-356, 2003. DOI: 10.1108/01445150310698643.

[6] K. Huang *et al*, "Three-dimensional printing of a tunable graphene-based elastomer for strain sensors with ultrahigh sensitivity," *Carbon,* vol. 143, *(1),* pp. 63-72, 2019. DOI: 10.1016/j.carbon.2018.11.008.

[7] N. Baecker *et al*, "Effects of vibration training on bone metabolism: results from a short-term bed rest study," *Eur J Appl Physiol,* vol. 112, *(5),* pp. 1741-1750, 2012. DOI: 10.1007/s00421-011-2137-3.

[8] S. Sehmisch *et al*, "Effects of low-magnitude, high-frequency mechanical stimulation in the rat osteopenia model," *Osteoporos. Int.,* vol. 20, *(12),* pp. 1999-2008, 2009. DOI: 10.1007/s00198-009-0892-3.

[9] K. Krishen, "Space applications for ionic polymer-metal composite sensors, actuators, and artificial muscles," *Acta Astronaut.,* vol. 64, *(11),* pp. 1160-1166, 2009. DOI: 10.1016/j.actaastro.2009.01.008.

[10] N. Lu and D. Kim, "Flexible and Stretchable Electronics Paving the Way for Soft Robotics," *Soft Robotics,* vol. 1, *(1),* pp. 53-62, 2014. DOI: 10.1089/soro.2013.0005.

[11] E. P. Gardner and K. O. Johnson, "The somatosensory system: Receptors and central pathways," in *Principles of Neural Science*, 5th ed., E. Kandel *et al*, Ed. McGraw-Hill Education, 2014, pp. 475-497.

[12] Y. Yang *et al*, "An Enhanced FingerVision for Contact Spatial Surface Sensing," *IEEE Sensors Journal,* vol. 21, *(15),* pp. 16492-16502, 2021. DOI: 10.1109/JSEN.2021.3076815.

[13] W. Chen and Z. Zhu, "Flexible actuators," in *Handbook of Smart Textiles*, X. Tao, Ed. Singapore: Springer Singapore, 2015, pp. 381-410.

[14] F. Wang, "Soft tactile sensors for human-machine interaction," in *Handbook of Smart Textiles*, X. Tao, Ed. Singapore: Springer Singapore, 2015, pp. 317-355.

[15] E. Davoodi *et al*, "3D-printed ultra-robust surface-doped porous silicone sensors for wearable biomonitoring," *ACS Nano,* vol. 14, *(2),* pp. 1520-1532, 2020. DOI: 10.1021/acsnano.9b06283.

[16] F. Han *et al*, "Materials, Electrical Performance, Mechanisms, Applications, and Manufacturing Approaches for Flexible Strain Sensors," *Nanomaterials,* vol. 11, *(5),* 2021.

[17] D. J. Lipomi *et al*, "Skin-like pressure and strain sensors based on transparent elastic films of carbon nanotubes," *Nature Nanotechnology,* vol. 6, *(12),* pp. 788-792, 2011. DOI: 10.1038/nnano.2011.184.

[18] H. Liu *et al*, "3D Printed Flexible Strain Sensors: From Printing to Devices and Signals," *Adv Mater,* vol. 33, *(8),* pp. 2004782, 2021. DOI: 10.1002/adma.202004782.

[19] W. Chen and X. Yan, "Progress in achieving high-performance piezoresistive and capacitive flexible pressure sensors: A review," *Journal of Materials Science & Technology,* vol. 43, pp. 175-188, 2020. DOI: 10.1016/j.jmst.2019.11.010.

[20] F. Xu *et al*, "Recent Developments for Flexible Pressure Sensors: A Review," *Micromachines,* vol. 9, *(11),* pp. 580, 2018. DOI: 10.3390/mi9110580.

[21] D. Kwon *et al*, "Highly Sensitive, Flexible, and Wearable Pressure Sensor Based on a Giant Piezocapacitive Effect of Three-Dimensional Microporous Elastomeric Dielectric Layer," *ACS Appl. Mater. Interfaces,* vol. 8, *(26),* pp. 16922-16931, 2016. DOI: 10.1021/acsami.6b04225.

[22] X. Wang, Z. Liu and T. Zhang, "Flexible Sensing Electronics for Wearable/Attachable Health Monitoring," *Small,* vol. 13, *(25),* pp. 1602790, 2017. DOI: 10.1002/smll.201602790.

[23] C. Liu *et al*, "3D printing technologies for flexible tactile sensors toward wearable electronics and electronic skin," *Polymers,* vol. 10, *(6),* pp. 629, 2018. DOI: 10.3390/polym10060629.

[24] S. Lao *et al*, "A Novel Capacitance-Based In-Situ Pressure Sensor for Wearable Compression Garments," *Micromachines,* vol. 10, *(11),* pp. 743-758, 2019. DOI: 10.3390/mi10110743.

[25] L. Persano *et al*, "High performance piezoelectric devices based on aligned arrays of nanofibers of poly(vinylidenefluoride-co-trifluoroethylene)," *Nature Communications,* vol. 4, *(1),* pp. 1633, 2013. DOI: 10.1038/ncomms2639.

[26] J. S. Lee *et al*, "Highly Sensitive and Multifunctional Tactile Sensor Using Free-standing ZnO/PVDF Thin Film with Graphene Electrodes for Pressure and Temperature Monitoring," *Scientific Reports,* vol. 5, *(1),* pp. 7887, 2015. DOI: 10.1038/srep07887.

[27] J. Wang, C. Lu and K. Zhang, "Textile-Based Strain Sensor for Human Motion Detection," *Energy Environ. Mater.,* vol. 3, *(1),* pp. 80-100, 2020. DOI: 10.1002/eem2.12041.

[28] X. Chen *et al*, "3D printed high-performance spider web-like flexible strain sensors with directional strain recognition based on conductive polymer composites," *Mater Lett,* vol. 306, pp. 130935, 2022. DOI: 10.1016/j.matlet.2021.130935.

[29] P. Wei *et al*, "Reprocessable 3D-Printed Conductive Elastomeric Composite Foams for Strain and Gas Sensing," *ACS Appl. Polym. Mater.,* vol. 1, *(4),* pp. 885-892, 2019. DOI: 10.1021/acsapm.9b00118.

[30] L. Duan, D. R. D'hooge and L. Cardon, "Recent progress on flexible and stretchable piezoresistive strain sensors: From design to application," *Progress in Materials Science,* vol. 114, pp. 100617, 2020. DOI: 10.1016/j.pmatsci.2019.100617.

[31] L. Ma *et al*, "A 3D flexible piezoresistive sensor based on surface-filled graphene nanosheets conductive layer," *Sensors and Actuators A: Physical,* vol. 332, *(1),* pp. 113144, 2021. DOI: 10.1016/j.sna.2021.113144.

[32] L. Qiu *et al*, "Ultrafast dynamic piezoresistive response of graphene-based cellular elastomers," *Adv Mater,* vol. 28, *(1),* pp. 194-200, 2016. DOI: 10.1002/adma.201503957.

[33] Y. R. Jeong *et al*, "Highly stretchable and sensitive strain sensors using fragmentized graphene foam," *Advanced Functional Materials,* vol. 25, *(27),* pp. 4228-4236, 2015. DOI: 10.1002/adfm.201501000.

[34] J. Shi *et al*, "Multiscale hierarchical design of a flexible piezoresistive pressure sensor with high sensitivity and wide linearity range," *Small,* vol. 14, *(27),* pp. 1800819, 2018. DOI: 10.1002/smll.201800819.

[35] R. Senthilkumar *et al*, "Piezoresistive nanocomposite films for foot strike data monitoring," *Sensors and Actuators A: Physical,* vol. 284, pp. 76-84, 2018. DOI: 10.1016/j.sna.2018.10.022.

[36] Z. Tang *et al*, "Coaxial carbon nanotube/polymer fibers as wearable piezoresistive sensors," *Sensors and Actuators A: Physical,* vol. 284, pp. 85-95, 2018. DOI: 10.1016/j.sna.2018.10.012.

[37] S. Jung *et al*, "Reverse-micelle-induced porous pressure-sensitive rubber for wearable human–machine interfaces," *Adv Mater,* vol. 26, *(28),* pp. 4825-4830, 2014. DOI: 10.1002/adma.201401364.

[38] T. T. Tung *et al*, "Recent advances in sensing applications of graphene assemblies and their composites," *Advanced Functional Materials,* vol. 27, *(46),* pp. 1702891, 2017. DOI: 10.1002/adfm.201702891.

[39] Q. Zheng *et al*, "Graphene-based wearable piezoresistive physical sensors," *Materials Today,* vol. 36, pp. 158-179, 2020. DOI: 10.1016/j.mattod.2019.12.004.

[40] B. Herren *et al*, "Development of ultrastretchable and skin attachable nanocomposites for human motion monitoring via embedded 3D printing," *Composites Part B: Engineering,* vol. 200, pp. 108224, 2020. DOI: 10.1016/j.compositesb.2020.108224.

[41] Y. Shu *et al*, "Surface-modified piezoresistive nanocomposite flexible pressure sensors with high sensitivity and wide linearity," *Nanoscale,* vol. 7, *(18),* pp. 8636-8644, 2015. DOI: 10.1039/C5NR01259G.

[42] J. Park *et al*, "Giant tunneling piezoresistance of composite elastomers with interlocked microdome arrays for ultrasensitive and multimodal electronic skins," *ACS Nano,* vol. 8, *(5),* pp. 4689-4697, 2014. DOI: 10.1021/nn500441k.

[43] N. Lu *et al*, "Highly sensitive skin-mountable strain gauges based entirely on elastomers," *Advanced Functional Materials,* vol. 22, *(19),* pp. 4044-4050, 2012. DOI: 10.1002/adfm.201200498.

[44] Y. Qin *et al*, "Lightweight, superelastic, and mechanically flexible graphene/polyimide nanocomposite foam for strain sensor application," *ACS Nano,* vol. 9, *(9),* pp. 8933-8941, 2015. DOI: 10.1021/acsnano.5b02781.

[45] O. Park *et al*, "In situ synthesis of thermochemically reduced graphene oxide conducting nanocomposites," *Nano Letters,* vol. 12, *(4),* pp. 1789-1793, 2012. DOI: 10.1021/nl203803d.

[46] H. Liu *et al*, "Electrically conductive polymer composites for smart flexible strain sensors: a critical review," *J. Mater. Chem. C,* vol. 6, *(45),* pp. 12121-12141, 2018. DOI: 10.1039/C8TC04079F.

[47] R. Yu *et al*, "Highly sensitive flexible piezoresistive sensor with 3D conductive network," *ACS Applied Materials & Interfaces,* vol. 12, *(31),* pp. 35291-35299, 2020. DOI: 10.1021/acsami.0c09552.

[48] S. Liu *et al*, "Ultrafast dynamic pressure sensors based on graphene hybrid structure," *ACS Applied Materials & Interfaces,* vol. 9, *(28),* pp. 24148-24154, 2017. DOI: 10.1021/acsami.7b07311.

[49] M. Abshirini *et al*, "3D printing of highly stretchable strain sensors based on carbon nanotube nanocomposites," *Advanced Engineering Materials,* vol. 20, *(10),* pp. 1800425, 2018. DOI: 10.1002/adem.201800425.

[50] M. Charara *et al*, "Highly sensitive compression sensors using three-dimensional printed polydimethylsiloxane/carbon nanotube nanocomposites," *J Intell Mater Syst Struct,* vol. 30, *(8),* pp. 1216-1224, 2019. DOI: 10.1177/1045389X19835953.

[51] J. Chen *et al*, "Intrinsic and extrinsic performance limits of graphene devices on SiO2," *Nature Nanotechnology,* vol. 3, *(4),* pp. 206-209, 2008. DOI: 10.1038/nnano.2008.58.

[52] X. Xie, Y. Mai and X. Zhou, "Dispersion and alignment of carbon nanotubes in polymer matrix: A review," *Materials Science and Engineering: R: Reports,* vol. 49, *(4),* pp. 89-112, 2005. DOI: 10.1016/j.mser.2005.04.002.

[53] M. Hempel *et al*, "A Novel Class of Strain Gauges Based on Layered Percolative Films of 2D Materials," *Nano Lett.,* vol. 12, *(11),* pp. 5714-5718, 2012. DOI: 10.1021/nl302959a.

[54] B. Dong *et al*, "High performance natural rubber composites with well-organized interconnected graphene networks for strain-sensing application," *Ind Eng Chem Res,* vol. 55, *(17),* pp. 4919-4929, 2016. DOI: 10.1021/acs.iecr.6b00214.

[55] T. Zhao *et al*, "Highly Sensitive Flexible Piezoresistive Pressure Sensor Developed Using Biomimetically Textured Porous Materials," *ACS Appl. Mater. Interfaces,* vol. 11, *(32),* pp. 29466-29473, 2019. DOI: 10.1021/acsami.9b09265.

[56] L. Huang *et al*, "Three-dimensional light-weight piezoresistive sensors based on conductive polyurethane sponges coated with hybrid CNT/CB nanoparticles," *Applied Surface Science,* vol. 548, pp. 149268, 2021. DOI: 10.1016/j.apsusc.2021.149268.

[57] Z. Wang and X. Ye, "A numerical investigation on piezoresistive behaviour of carbon nanotube/polymer composites: mechanism and optimizing principle," *Nanotechnology,* vol. 24, *(26),* pp. 265704, 2013. DOI: 10.1088/0957-4484/24/26/265704.

[58] A. Manta, M. Gresil and C. Soutis, "Predictive model of graphene based polymer nanocomposites: electrical performance," *Applied Composite Materials,* vol. 24, *(2),* pp. 281-300, 2017. DOI: 10.1007/s10443-016-9557-5.

[59] V. Kumar *et al*, "Silicone Rubber Composites Reinforced by Carbon Nanofillers and Their Hybrids for Various Applications: A Review," *Polymers,* vol. 13, *(14),* 2021. DOI: 10.3390/polym13142322.

[60] Y. Huang *et al*, "Synergistic effects and piezoresistive characteristics of carbon nanofillers/silicone rubber composites," *Mater. Technol.,* vol. 31, *(4),* pp. 229-233, 2016. DOI: 10.1179/1753555715Y.0000000046.

[61] S. Mei *et al*, "3D-Printed thermoplastic polyurethane/graphene composite with porous segregated structure: Toward ultralow percolation threshold and great strain sensitivity," *Journal of Applied Polymer Science,* vol. 138, *(14),* pp. 50168, 2021. DOI: 10.1002/app.50168.

[62] F. R. Al-solamy, A. A. Al-Ghamdi and W. E. Mahmoud, "Piezoresistive behavior of graphite nanoplatelets based rubber nanocomposites," *Polym. Adv. Technol.,* vol. 23, *(3),* pp. 478-482, 2012. DOI: 10.1002/PAT.1902.

[63] H. Yang *et al*, "Highly sensitive and stretchable graphene-silicone rubber composites for strain sensing," *Composites Sci. Technol.,* vol. 167, pp. 371-378, 2018. DOI: 10.1016/j.compscitech.2018.08.022.

[64] H. Yang *et al*, "Piezoresistive response of graphene rubber composites considering the tunneling effect," *J. Mech. Phys. Solids,* vol. 139, pp. 103943, 2020. DOI: 10.1016/j.jmps.2020.103943.

[65] J. G. Simmons, "Generalized Formula for the Electric Tunnel Effect between Similar Electrodes Separated by a Thin Insulating Film," *Journal of Applied Physics,* vol. 34, *(6),* pp. 1793-1803, 1963. DOI: 10.1063/1.1702682.

[66] W. Obitayo and T. Liu, "A Review: Carbon Nanotube-Based Piezoresistive Strain Sensors," *Journal of Sensors,* vol. 2012, pp. 1-15, 2012. DOI: 10.1155/2012/652438.

[67] M. Amjadi *et al*, "Stretchable, Skin-Mountable, and Wearable Strain Sensors and Their Potential Applications: A Review," *Advanced Functional Materials,* vol. 26, *(11),* pp. 1678-1698, 2016. DOI: 10.1002/adfm.201504755.

[68] M. Liu *et al*, "Fundamental Insights into Graphene Strain Sensing," *Nano Lett.,* vol. 21, *(1),* pp. 833-839, 2021. DOI: 10.1021/acs.nanolett.0c04577.

[69] A. Georgopoulou and F. Clemens, "Piezoresistive Elastomer-Based Composite Strain Sensors and Their Applications," *ACS Appl. Electron. Mater.,* vol. 2, *(7),* pp. 1826-1842, 2020. DOI: 10.1021/acsaelm.0c00278.

[70] T. Giffney *et al*, "Highly stretchable printed strain sensors using multi-walled carbon nanotube/silicone rubber composites," *Sensors and Actuators A: Physical,* vol. 259, pp. 44-49, 2017. DOI: 10.1016/j.sna.2017.03.005.

[71] C. Liu and J. Choi, "Strain-Dependent Resistance of PDMS and Carbon Nanotubes Composite Microstructures," *IEEE Transactions on Nanotechnology,* vol. 9, *(5),* pp. 590-595, 2010. DOI: 10.1109/TNANO.2010.2060350.

[72] S. Nesaei *et al*, "Additive Manufacturing With Conductive, Viscoelastic Polymer Composites: Direct-Ink-Writing of Electrolytic and Anodic Poly(Ethylene Oxide) Composites," *Journal of Manufacturing Science and Engineering,* vol. 139, *(11),* 2017. DOI: 10.1115/1.4037238.

[73] S. B. Balani *et al*, "Processes and materials used for direct writing technologies: A review," *Results in Engineering,* vol. 11, pp. 100257, 2021. DOI: 10.1016/j.rineng.2021.100257.

[74] Y. Zhang *et al*, "Recent Progress of Direct Ink Writing of Electronic Components for Advanced Wearable Devices," *ACS Appl. Electron. Mater.,* vol. 1, *(9),* pp. 1718-1734, 2019. DOI: 10.1021/acsaelm.9b00428.

[75] J. F. Christ *et al*, "Bidirectional and Stretchable Piezoresistive Sensors Enabled by Multimaterial 3D Printing of Carbon Nanotube/Thermoplastic Polyurethane Nanocomposites," *Polymers,* vol. 11, *(1),* 2019. DOI: 10.3390/polym11010011.

[76] A. Georgopoulou, T. Sebastian and F. Clemens, "Thermoplastic elastomer composite filaments for strain sensing applications extruded with a fused deposition modelling 3D printer," *Flex. Print. Electron.,* vol. 5, *(3),* pp. 035002, 2020. DOI: 10.1088/2058-8585/ab9a22.

[77] C. J. Hohimer *et al*, "3D printed conductive thermoplastic polyurethane/carbon nanotube composites for capacitive and piezoresistive sensing in soft pneumatic actuators," *Additive Manufacturing,* vol. 34, pp. 101281, 2020. DOI: 10.1016/j.addma.2020.101281.

[78] N. Kumar *et al*, "Additive manufacturing of flexible electrically conductive polymer composites via CNC-assisted fused layer modeling process," *J Braz. Soc. Mech. Sci. Eng,* vol. 40, *(4),* pp. 1-13, 2018. DOI: 10.1007/s40430-018-1116-6.

[79] Rahim, Tuan Noraihan Azila Tuan, A. M. Abdullah and H. Md Akil, "Recent Developments in Fused Deposition Modeling-Based 3D Printing of Polymers and Their Composites," *Polymer Reviews,* vol. 59, *(4),* pp. 589-624, 2019. DOI: 10.1080/15583724.2019.1597883.

[80] Hugo I.Medellin-Castillo and Jorge Zaragoza-Siqueiros, "Design and Manufacturing Strategies for Fused Deposition Modelling in Additive Manufacturing: A Review," *Chin. J. Mech. Eng.,* vol. 32, *(3),* pp. 1-16, 2019. DOI: 10.1186/s10033-019-0368-0.

[81] D. Thaler, N. Aliheidari and A. Ameli, "Mechanical, electrical, and piezoresistivity behaviors of additively manufactured acrylonitrile butadiene styrene/carbon nanotube nanocomposites," *Sms,* vol. 28, *(8),* pp. 84004, 2019. DOI: 10.1088/1361-665X/ab256e.

[82] S. C. Daminabo *et al*, "Fused deposition modeling-based additive manufacturing (3D printing): techniques for polymer material systems," *Materials Today Chemistry,* vol. 16, pp. 100248, 2020. DOI: 10.1016/j.mtchem.2020.100248.

[83] A. M. Kamat *et al*, "Biomimetic Soft Polymer Microstructures and Piezoresistive Graphene MEMS Sensors Using Sacrificial Metal 3D Printing," *ACS Appl. Mater. Interfaces,* vol. 13, *(1),* pp. 1094-1104, 2021. DOI: 10.1021/acsami.0c21295.

[84] M. R. Khosravani and T. Reinicke, "3D-printed sensors: Current progress and future challenges," *Sensors and Actuators A: Physical,* vol. 305, pp. 111916, 2020. DOI: 10.1016/j.sna.2020.111916.

[85] A. Nag *et al*, "3D printed mould-based graphite/PDMS sensor for low-force applications," *Sensors and Actuators.A.Physical.,* vol. 280, pp. 525-534, 2018. DOI: 10.1016/j.sna.2018.08.028.

[86] H. Lee *et al*, "Mogul-Patterned Elastomeric Substrate for Stretchable Electronics," *Adv Mater,* vol. 28, *(16),* pp. 3069-3077, 2016. DOI: 10.1002/adma.201505218.

[87] J. Park *et al*, "Tactile-Direction-Sensitive and Stretchable Electronic Skins Based on Human-Skin-Inspired Interlocked Microstructures," *ACS Nano,* vol. 8, *(12),* pp. 12020-12029, 2014. DOI: 10.1021/nn505953t.

[88] M. Kucewicz *et al*, "Modelling, and characterization of 3D printed cellular structures," *Mater Des,* vol. 142, pp. 177-189, 2018. DOI: 10.1016/j.matdes.2018.01.028.

[89] O. Al-Ketan and R. K. Abu Al-Rub, "Multifunctional mechanical metamaterials based on triply periodic minimal surface lattices," *Advanced Engineering Materials,* vol. 21, *(10),* pp. 1900524, 2019. DOI: 10.1002/adem.201900524.

[90] A. M. Abou-Ali *et al*, "Mechanical response of 3D printed bending-dominated ligament-based triply periodic cellular polymeric solids," *Journal of Materials Engineering and Performance,* vol. 28, *(4),* pp. 2316-2326, 2019. DOI: 10.1007/s11665-019-03982-8.

[91] I. Maskery *et al*, "Insights into the mechanical properties of several triply periodic minimal surface lattice structures made by polymer additive manufacturing," *Polymer,* vol. 152, pp. 62-71, 2018. DOI: 10.1016/j.polymer.2017.11.049.

[92] M. Keshavarzan *et al*, "Investigation on the failure mechanism of triply periodic minimal surface cellular structures fabricated by Vat photopolymerization Additive Manufacturing under compressive loadings," *Mech. Mater.,* vol. 140, pp. 103150, 2020. DOI: 10.1016/j.mechmat.2019.103150.

[93] S. AlMahri *et al*, "Evaluation of the dynamic response of triply periodic minimal surfaces subjected to high strain-rate compression," *Additive Manufacturing,* vol. 46, pp. 102220, 2021. DOI: 10.1016/j.addma.2021.102220.

[94] W. Yang *et al*, "Acoustic absorptions of multifunctional polymeric cellular structures based on triply periodic minimal surfaces fabricated by stereolithography," *Virtual and Physical Prototyping,* vol. 15, *(2),* pp. 242-249, 2020. DOI: 10.1080/17452759.2020.1740747.

[95] D. W. Abueidda, I. Jasiuk and N. A. Sobh, "Acoustic band gaps and elastic stiffness of PMMA cellular solids based on triply periodic minimal surfaces," *Mater Des,* vol. 145, pp. 20-27, 2018. DOI: rg/10.1016/j.matdes.2018.02.032.

[96] L. Zhang *et al*, "Energy absorption characteristics of metallic triply periodic minimal surface sheet structures under compressive loading," *Additive Manufacturing,* vol. 23, pp. 505-515, 2018. DOI: 10.1016/j.addma.2018.08.007.

[97] D. Sharma and S. S. Hiremath, "Additively manufactured mechanical metamaterials based on triply periodic minimal surfaces: Performance, challenges, and application," *Mechanics of Advanced Materials and Structures,* vol. 9, *(1),* pp. 1-31, 2021. DOI: 10.1080/15376494.2021.1948151.

[98] D. Li *et al*, "Comparison of Mechanical Properties and Energy Absorption of Sheet-Based and Strut-Based Gyroid Cellular Structures with Graded Densities," *Materials; Materials (Basel),* vol. 12, *(13),* pp. 2183, 2019. DOI: 10.3390/ma12132183.

[99] M. B. Coskun *et al*, "Detecting subtle vibrations using graphene-based cellular elastomers," *ACS Applied Materials & Interfaces,* vol. 9, *(13),* pp. 11345-11349, 2017. DOI: 10.1021/acsami.7b01207.

[100] L. Qiu *et al*, "Biomimetic superelastic graphene-based cellular monoliths," *Nature Communications,* vol. 3, *(1),* pp. 1-7, 2012. DOI: 10.1038/ncomms2251.

[101] J. H. Song *et al*, "Surface-Embedded Stretchable Electrodes by Direct Printing and their Uses to Fabricate Ultrathin Vibration Sensors and Circuits for 3D Structures," *Adv Mater,* vol. 29, *(43),* pp. 1702625-n/a, 2017. DOI: 10.1002/adma.201702625.

[102] Khurana *et al*, "Multifunctional graphitic tracks on flexible polymer sheet as strain, acoustic vibration and human motion sensor," *Measurement: Journal of the International Measurement Confederation,* vol. 146, pp. 9-14, 2019. DOI: 10.1016/j.measurement.2019.05.041.

[103] C. S. Boland *et al*, "Sensitive, High-Strain, High-Rate Bodily Motion Sensors Based on Graphene–Rubber Composites," *ACS Nano; ACS Nano,* vol. 8, *(9),* pp. 8819-8830, 2014. DOI: 10.1021/nn503454h.

[104] D. E. Hanson *et al*, "Stress softening experiments in silica-filled polydimethylsiloxane provide insight into a mechanism for the Mullins effect," *Polymer,* vol. 46, *(24),* pp. 10989-10995, 2005. DOI: 10.1016/j.polymer.2005.09.039.

[105] J. Diani, B. Fayolle and P. Gilormini, "A review on the Mullins effect," *European Polymer Journal,* vol. 45, *(3),* pp. 601-612, 2009. DOI: 10.1016/j.eurpolymj.2008.11.017.

[106] B. Fazekas and T. J. Goda, "Constitutive modelling of rubbers: Mullins effect, residual strain, time-temperature dependence," *Int. J. Mech. Sci.,* vol. 210, pp. 106735, 2021. DOI: 10.1016/j.ijmecsci.2021.106735.

[107] P. Austrell and A. K. Olsson, "Considering amplitude dependence during cyclic loading of elastomers using an equivalent viscoelastic approach," *Polym. Test.,* vol. 31, *(7),* pp. 909-915, 2012. DOI: 10.1016/j.polymertesting.2012.05.005.

[108] W. Luo *et al*, "Frequency-and strain-amplitude-dependent dynamical mechanical properties and hysteresis loss of CB-filled vulcanized natural rubber," *Int. J. Mech. Sci.,* vol. 52, *(2),* pp. 168-174, 2010. DOI: 10.1016/j.ijmecsci.2009.09.001.

[109] A. R. Payne, "The dynamic properties of carbon black-loaded natural rubber vulcanizates. Part I," *J Appl Polym Sci,* vol. 6, *(19),* pp. 57-63, 1962. DOI: 10.1002/app.1962.070061906.

[110] F. Xin, X. Bai and L. Qian, "Modeling and experimental verification of frequency-, amplitude-, and magneto-dependent viscoelasticity of magnetorheological elastomers," *Sms,* vol. 25, *(10),* pp. 105002, 2016. DOI: 10.1088/0964-1726/25/10/105002.

[111] P. Cataldi, A. Athanassiou and I. S. Bayer, "Graphene Nanoplatelets-Based Advanced Materials and Recent Progress in Sustainable Applications," *Applied Sciences,* vol. 8, *(9),* 2018. DOI: 10.3390/app8091438.

[112] S. Rosso *et al*, "An Optimization Workflow in Design for Additive Manufacturing," *Applied Sciences,* vol. 11, *(6),* 2021. DOI: 10.3390/app11062572.

[113] M. Kumke, H. Watschke and T. Vietor, "A new methodological framework for design for additive manufacturing," *Virtual and Physical Prototyping,* vol. 11, *(1),* pp. 3-19, 2016. DOI: 10.1080/17452759.2016.1139377.

[114] I. Gibson, *Additive Manufacturing Technologies.* (3rd ed.) Cham, Switzerland: Springer, 2021.

[115] M. Alzahrani, S. Choi and D. W. Rosen, "Design of truss-like cellular structures using relative density mapping method," *Mater Des,* vol. 85, pp. 349-360, 2015. DOI: 10.1016/j.matdes.2015.06.180.

[116] S. Yu, J. Sun and J. Bai, "Investigation of functionally graded TPMS structures fabricated by additive manufacturing," *Mater Des,* vol. 182, pp. 108021, 2019. DOI: 10.1016/j.matdes.2019.108021.

[117] N. Strömberg, "Optimal grading of TPMS-based lattice structures with transversely isotropic elastic bulk properties," *Engineering Optimization,* vol. 53, *(11),* pp. 1871-1883, 2021. DOI: 10.1080/0305215X.2020.1837790.

[118] S. Catchpole-Smith *et al*, "Thermal conductivity of TPMS lattice structures manufactured via laser powder bed fusion," *Additive Manufacturing,* vol. 30, pp. 100846, 2019. DOI: 10.1016/j.addma.2019.100846.

[119] S. Vijayavenkataraman, L. Y. Kuan and W. F. Lu, "3D-printed ceramic triply periodic minimal surface structures for design of functionally graded bone implants," *Mater Des,* vol. 191, pp. 108602, 2020. DOI: 10.1016/j.matdes.2020.108602.

[120] L. Meng *et al*, "From Topology Optimization Design to Additive Manufacturing: Today's Success and Tomorrow's Roadmap," *Archives of Computational Methods in Engineering,* vol. 27, *(3),* pp. 805-830, 2020. DOI: 10.1007/s11831-019-09331-1.

[121] J. Liu *et al*, "Current and future trends in topology optimization for additive manufacturing," *Structural and Multidisciplinary Optimization,* vol. 57, *(6),* pp. 2457-2483, 2018. DOI: 10.1007/s00158-018-1994-3.

[122] T. Dbouk, "A review about the engineering design of optimal heat transfer systems using topology optimization," *Appl. Therm. Eng.,* vol. 112, pp. 841-854, 2017. DOI: 10.1016/j.applthermaleng.2016.10.134.

[123] C. H. P. Nguyen and Y. Choi, "Multiscale design of functionally graded cellular structures for additive manufacturing using level-set descriptions," *Structural and Multidisciplinary Optimization,* vol. 64, *(4),* pp. 1983, 2021. DOI: 10.1007/s00158-021-02959-3.

[124] M. McConaha, V. Venugopal and S. Anand, "Design Tool for Topology Optimization of Self Supporting Variable Density Lattice Structures for Additive Manufacturing," *Journal of Manufacturing Science and Engineering,* vol. 143, *(7),* 2021. DOI: 10.1115/1.4049507.

[125] V. Ho-Huu *et al*, "An improved differential evolution based on roulette wheel selection for shape and size optimization of truss structures with frequency constraints," *Neural Computing and Applications,* vol. 29, *(1),* pp. 167-185, 2018. DOI: 10.1007/s00521-016-2426-1.

[126] A. Kaveh and S. Mahjoubi, "Hypotrochoid spiral optimization approach for sizing and layout optimization of truss structures with multiple frequency constraints," *Engineering with Computers,* vol. 35, *(4),* pp. 1443-1462, 2019. DOI: 10.1007/s00366-018-0675-6.

[127] R. M. Gorguluarslan *et al*, "An improved lattice structure design optimization framework considering additive manufacturing constraints," *Rapid Prototyping Journal,* vol. 23, *(2),* pp. 305-319, 2017. DOI: 10.1108/RPJ-10-2015-0139.

[128] A. Kaveh and T. Bakhshpoori, *Metaheuristics.* 2019.

[129] K. Hussain *et al*, "Metaheuristic research: a comprehensive survey," *The Artificial Intelligence Review,* vol. 52, *(4),* pp. 2191-2233, 2019. DOI: 10.1007/s10462-017-9605-z.

[130] C. Goh and K. C. Tan, *Evolutionary Multi-Objective Optimization in Uncertain Environments Issues and Algorithms.* (1st ed.) 2009. DOI: 10.1007/978-3-540-95976-2.

[131] X. Yang, "Firefly Algorithms for Multimodal Optimization," vol. 5792, pp. 169-178, 2010. DOI: 10.1007/978-3-642-04944-6_14.

[132] A. H. Gandomi, X. Yang and A. H. Alavi, "Mixed variable structural optimization using Firefly Algorithm," *Comput. Struct.,* vol. 89, *(23),* pp. 2325-2336, 2011. DOI: 10.1016/j.compstruc.2011.08.002.

[133] J. S. Arora, "Methods for discrete variable structural optimization," in *Structures Congress 2000,* 2000, pp. 1-8.

[134] B. Sharif, G. G. Wang and T. Y. ElMekkawy, "Mode Pursuing Sampling Method for Discrete Variable Optimization on Expensive Black-Box Functions," *Journal of Mechanical Design,* vol. 130, *(2),* 2008. DOI: 10.1115/1.2803251.

[135] G. G. Wang and S. Shan, "Review of Metamodeling Techniques in Support of Engineering Design Optimization," *Journal of Mechanical Design,* vol. 129, *(4),* pp. 370-380, 2006. DOI: 10.1115/1.2429697.

[136] A. Baykasoğlu and F. B. Ozsoydan, "An improved firefly algorithm for solving dynamic multidimensional knapsack problems," *Expert Syst. Appl.,* vol. 41, *(8),* pp. 3712-3725, 2014. DOI: 10.1016/j.eswa.2013.11.040.

[137] A. Baykasoğlu and F. B. Ozsoydan, "Adaptive firefly algorithm with chaos for mechanical design optimization problems," *Applied Soft Computing,* vol. 36, pp. 152-164, 2015. DOI: 10.1016/j.asoc.2015.06.056.

[138] T. Dokeroglu *et al*, "A survey on new generation metaheuristic algorithms," *Comput. Ind. Eng.,* vol. 137, pp. 106040, 2019. DOI: 10.1016/j.cie.2019.106040.

[139] Y. Mo, Y. Ma and Q. Zheng, "Optimal choice of parameters for firefly algorithm," in *International Conference on Digital Manufacturing and Automation,* 2013, pp. 887-892.

[140] D. Bratton and J. Kennedy, "Defining a standard for particle swarm optimization," in *2007 IEEE Swarm Intelligence Symposium,* 2007, pp. 120-127.

[141] R. Storn, "On the usage of differential evolution for function optimization," in *Proceedings of North American Fuzzy Information Processing,* 1996, pp. 519-523.

[142] B. A. Hassan, "CSCF: a chaotic sine cosine firefly algorithm for practical application problems," *Neural Computing and Applications,* vol. 33, *(12),* pp. 7011-7030, 2021. DOI: 10.1007/s00521-020-05474-6.

[143] S. Kalra and S. Arora, "Firefly algorithm hybridized with flower pollination algorithm for multimodal functions," in *Proceedings of the International Congress on Information and Communication,* 2016, . DOI: 10.1007/978-981-10-0767-5_23.

[144] S. Sumpunsri, C. Thammarat and D. Puangdownreong, "Multiobjective Lévy-Flight Firefly Algorithm for Multiobjective Optimization," pp. 145-153, 2021. DOI: 10.1007/978-3-030-68154-8_15.

[145] X. Yang, "Multiobjective firefly algorithm for continuous optimization," *Engineering with Computers,* vol. 29, *(2),* pp. 175-184, 2013. DOI: 10.1007/s00366-012-0254-1.

[146] *Zortrax 3D Printers User Guide: M Series*
Available: https://support.zortrax.com/user-guides/.

[147] M. Tian *et al*, "Temperature-dependent electrical properties of graphene nanoplatelets film dropped on flexible substrates," *J. Mater. Res.,* vol. 29, *(11),* pp. 1288-1294, 2014. DOI: 10.1557/jmr.2014.109.

[148] M. S. Dresselhaus *et al*, "Raman spectroscopy of carbon nanotubes," *Physics Reports,* vol. 409, *(2),* pp. 47-99, 2005. DOI: 10.1063/5.0030809.

[149] M. S. Dresselhaus, A. Jorio and R. Saito, "Characterizing graphene, graphite, and carbon nanotubes by Raman spectroscopy," *Annu.Rev.Condens.Matter Phys.,* vol. 1, *(1),* pp. 89-108, 2010. DOI: 10.1146/annurev-conmatphys-070909-103919.

[150] V. Skakalova and A. B. Kaiser, *Graphene: Properties, Preparation, Characterisation and Devices.* Cambridge: Elsevier Science & Technology, 2014*number 57*.

[151] C. Thomsen and S. Reich, "Double resonant Raman scattering in graphite," *Phys. Rev. Lett.,* vol. 85, *(24),* pp. 5214, 2000. DOI: 10.1103/PhysRevLett.85.5214.

[152] L. M. Malard *et al*, "Raman spectroscopy in graphene," *Physics Reports,* vol. 473, *(5-6),* pp. 51-87, 2009. DOI: 10.1016/j.physrep.2009.02.003.

[153] J. H. Warner *et al*, "Chapter 5 - characterisation techniques," in *Graphene*, J. H. Warner *et al*, Ed. UK: Elsevier Inc, 2013, pp. 229-332.

[154] M. Hulman, "Raman spectroscopy of graphene," in *Graphene - Properties, Preparation, Characterisation and Devices*, V. Skákalová and A. B. Kaiser, Eds. UK: Elsevier, 2014, pp. 156-183.

[155] E. Davoodi *et al*, "Sacrificial 3D printing of shrinkable silicone elastomers for enhanced feature resolution in flexible tissue scaffolds," *Acta Biomaterialia,* vol. 117, pp. 261-272, 2020. DOI: 10.1016/j.actbio.2020.10.001.

[156] S. Yu *et al*, "A variable step size firefly algorithm for numerical optimization," *Applied Mathematics and Computation,* vol. 263, pp. 214-220, 2015. DOI: 10.1016/j.amc.2015.04.065.

Appendix A
Sensor Photos

Additional photos of the sensor are presented here, as shown in Appendix Figure A-1. Appendix Figure A-1a and b show the benchmark sensor before and after mounting to electrodes, respectively. Appendix Figure A-1c shows SEM images of the sensor surface morphology, with a detail view on the right. SEM settings are repeated as specified in Section 3.1.

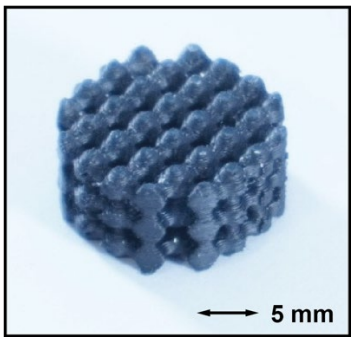

(a)

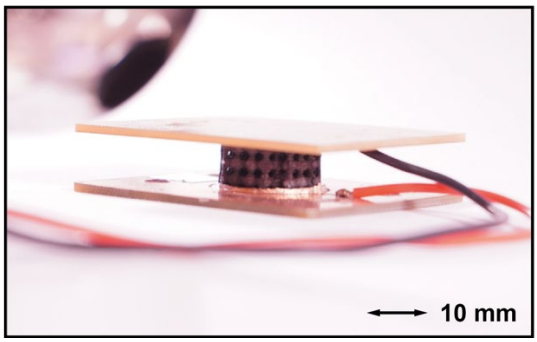

(b)

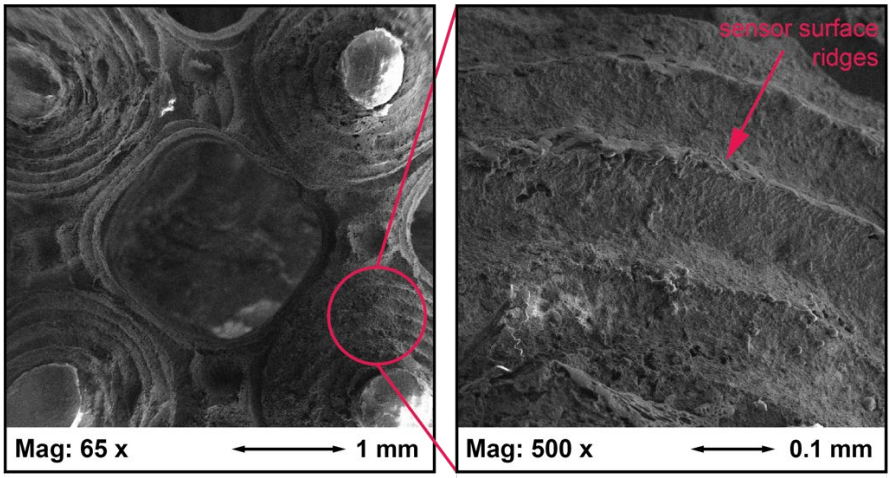

(c)

Appendix Figure A-1. (a) Image of benchmark sensor mounted on copper electrodes. (b) Image of benchmark sensor. (c) SEM images of benchmark sensor surface, with detail view of surface ridges shown on the right.

Appendix B
Shaker Natural Frequencies

Natural frequencies of the electrodynamic flexure shaker in the 0-200 Hz bandwidth were determined using impact hammer testing. Lateral vibrations (perpendicular to the shaker armature travel direction) were measured using an accelerometer while exciting with an impact hammer. As shown in Appendix Figure B-1, there are noticeable resonant peaks at 95 Hz and 165 Hz for the measured accelerance.

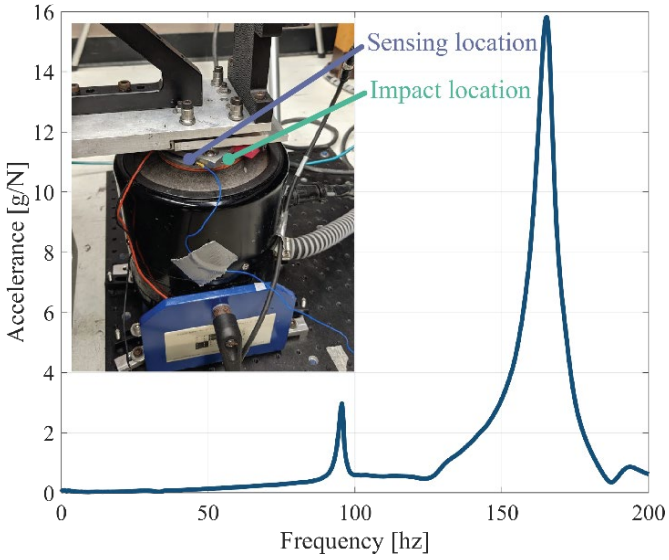

Appendix Figure B-1. Accelerance plot showing the shaker's first two natural frequencies found from impact hammer testing. The sensing and impact locations are on the shaker armature head as shown in the photo.

Appendix C
Optimal Sensor Resistance Measurement

Wheatstone bridges are often used for piezoresistive sensor measurements because of their ability to accurately measure small resistance changes [1]. Here a Wheatstone quarter bridge configuration is used (see Appendix Figure C-1), where the sensor resistance R_s is the only resistor that changes in the circuit (resistors $R_a, R_b,$ and R_c are fixed values). The same power supply and DAS are used as mentioned in Section 3.2.1.1, where the voltage V_{out} is measured directly by the DAS. By rearranging Equation (C.1) for V_{out} to Equation (C.2), the sensor resistance can be solved for a given voltage measurement. For the optimal sensor, the Wheatstone bridge configuration was only necessary for measuring the small resistance changes at ε_{pk} = 1-2%.

$$V_{out} = V_{in}\left(\frac{R_c}{R_s + R_c} - \frac{R_b}{R_a + R_b}\right) \tag{C.1}$$

$$R_s = R_c \frac{V_{in}}{V_{out} + \left(\frac{V_{in}R_b}{R_a + R_b}\right)} - 1 \tag{C.2}$$

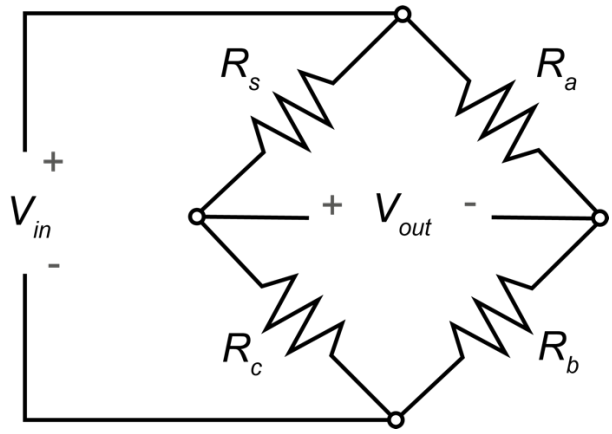

Appendix Figure C-1. Wheatstone quarter bridge configuration.